Interface energy transport of two-dimensional (2D) MoS_2

by

Pengyu Yuan

A dissertation submitted to the graduate faculty

in partial fulfillment of the requirements for the degree of

DOCTOR OF PHILOSOPHY

Major: Mechanical Engineering

Program of Study Committee:
Xinwei Wang, Major Professor
Chenxu Yu
Gap-Yong Kim
Hui Hu
Reza Montazami

The student author, whose presentation of the scholarship herein was approved by the program of study committee, is solely responsible for the content of this dissertation. The Graduate College will ensure this dissertation is globally accessible and will not permit alterations after a degree is conferred.

Iowa State University

Ames, Iowa

2018

DEDICATION

This dissertation is dedicated to my dear father Ding Yuan, and mother, Fengqin Hu, who have loved and supported me throughout my life;

To my beloved and beautiful wife, Yuning Chen, who has always been supporting me, inspiring me, and bring continuous happiness to me.

TABLE OF CONTENTS

Page

LIST OF FIGURES

Page

LIST OF TABLES

Page

NOMENCLATURE

2D	Two Dimensional
SL	Single Layer
FL	Few Layer
G	Interface Thermal Conductance
R	Interface Thermal Resistance
D	Hot Carrier Diffusivity
k	In-plane Thermal Conductivity

ACKNOWLEDGMENTS

I would like first offer my great appreciation to my advisor and my committee chair, Dr. Xinwei Wang for providing the opportunity to join the Micro/Nanoscale Thermal Science Laboratory and engaging in my Ph. D. projects. His expertise in thermal science and experimental skills improved my research ability and prepared me for future challenges. Without Dr. Wang's guidance, I would not have been able to obtain these great achievements. Next, I would like to sincerely thank my committee members, Dr. Chenxu Yu, Dr. Gap-Yong Kim, Dr. Hui Hu, Dr. Reza Montazami, for their suggestion throughout the course of my Ph. D. project and research and for their helpful comments on my preliminary exam.

Next, I would like to thank all my colleagues in the Micro/Nanoscale Thermal Science Laboratory for supporting my research, especially Dr. Shen Xu, Dr. Chong Li, Ridong Wang, Tianyu Wang, Meng Han, Bowen Zhu, Dr. Hong Tan of Nanjing University of Science and Technology. Greatly appreciate to the help from my friends, the department faculty and staff for making my time at Iowa State University a wonderful experience. Also thanks to my family for their support and encouragement.

Finally, the financial support of these researches by National Science Foundation (CBET1235852, CMMI1264399), Department of Energy (DENE0000671, DEEE0007686), and Iowa Energy Center (MG-16-025, OG-17-005). "Taishan Scholar" program of Shandong, China are gratefully acknowledged. In addition, I thank Dr. Chong Li for the MD simulation study about the thickness effect on interface energy coupling between MoS_2 and c-Si substrate.

ABSTRACT

The bottleneck of most modern technologies and energy solutions has been attributed to the thermal problems at the nanoscale. Especially, the thermal transport across interfaces and in-plane direction can significantly influence the overall performance of 2D nanosystems. So accurate thermal-physical characterization of the 2D materials is very important for both fundamental research and industrial applications.

Focusing on 2D mechanically exfoliated MoS_2, at first, we conduct a detailed temperature and laser power dependent micro-Raman spectroscopy study of FL MoS_2 (4.2 to 45 nm thick) on c-Si substrate. We measured the interfacial thermal resistance (R) at room temperature decreases with increased layers of MoS_2. Furthermore, we find that the number of layers of MoS_2 deeply affects the film corrugation, morphology, and interfacial thermal resistance. Then, for the first time, we consider the hot carrier excitation, diffusion and recombination in Raman 2D MoS_2-substrate interface energy coupling study. The hot carrier diffusion could become significant when the diffusion length is long or laser heating spot size is small. By applying different laser heating sizes in Raman experiment, we could determine both R and the hot carrier diffusivity for four sub-10 nm thick MoS_2 (3.6 to 9.0 nm thick). Especially, the hot carrier diffusion study is conducted without applying an electric field or electrical contacts so the results reflect the intrinsic properties of virgin 2D materials. After that, we realize that in widely applied Raman characterization of 2D material interface thermal resistance, laser absorption in the 2D atomic layer and its absolute temperature rise are needed. These factors could cause the largest experimental uncertainty. To this end, we develop a novel energy transport state-resolved Raman (ET-Raman) to address these critical issues. In ET-Raman, under steady laser heating, by constructing two steady heat conduction states with

different laser spot sizes, we differentiate the effect of R and hot carrier diffusivity (D). By constructing an extreme state of zero/negligible heat conduction using a picosecond laser, we differentiate the effect of R and material's specific heat. Combining the steady state Raman and pico-second Raman, we precisely determine R and D without the need of laser absorption and temperature rise of the 2D atomic layer. Seven MoS_2 samples (6.6 nm to 17.4 nm) on c-Si and six MoS_2 samples (1.8 nm to 18 nm) on glass substrate prepared by mechanical exfoliation are characterized using ET-Raman. At last, in order to reduce the dependence on other's work, we developed another new technique that could simultaneously determine k, D, and R of eight MoS_2 samples ranging from 2.4 nm to 37.8 nm thickness. The in-plane thermal conductivity could be determined without referring other's work. Besides, this systematic non-contact thickness-dependent thermal conductivity study reveals the intrinsic properties of FL MoS_2 and provides a practical guide for further advancing MoS_2 based device technologies.

CHAPTER 1. INTRODUCTION AND LITERATURE REVIEW

1.1 Two-Dimensional MoS_2

Two-dimensional (2D) atomic materials have attracted considerable attention for use in next-generation nano-electronic devices because, compared to one-dimensional materials, they are relatively easy to be used to fabricate complex structures. Currently, the most widely studied 2D material is graphene due to its rich physics and its high mobility.[1-3] However, natural graphene does not have a bandgap that makes it not suitable for many applications (*e.g.,* transistors). [4] As a result, more and more works have begun examining possible application of other 2D materials with the knowledge gained from graphene.

2D transition metal dichalcogenides (TMDs), in particular 2D MoS_2, have attracted ongoing research interest from both academic and applied communities because of their suitability for future electronic, piezoelectric and optoelectronic device applications.[5-8] Bulk MoS_2 crystals are stacks of layers held together in the vertical direction by weak van der Waals force, making the fabrication of few-layers and even single-layer sample possible by micro-mechanical cleavage technique.[9] Large-area sample can also prepared by chemical vapor deposition (CVD) method or liquid phase exfoliation.[10,11] Besides, MoS_2 is interesting for next generation devices due to their tunable bandgap structure. For instance, monolayer MoS_2 has a direct bandgap of 1.8 eV so it can serve as the the nano-transistor channel with an on/off ratio up to 10^8 , logic circuits and amploifiers with high gain.[12,13] Interestingly, the bulk MoS_2 has an indirect bandgap of 1.29 eV. [14,15] This thickness-dependent bandgap makes it applicable to potential photo-detection and optoelectronic applications and could be of interest for achieving a higher power conversion efficiency in traditional silicon solar cells.[16,17]

1.2 Thermal Transport across the Atomic-Layer Interface

For the design and operation of these devices, knowledge of the materials' thermal properties and the interfacial thermal conductance between adjacent layers [18] is a great factor in determining the device performance and durability. Especially, the interface between a two-dimensional atomic layer material and substrate plays a critical role in the overall thermal conductance in the nanosystem and therefore determines the devices' reliability, heat dissipation during operation, and lifetime.[19,20] The thermal transport across interfaces is quantified by the interfacial thermal conductance or Kapitza conductance (denoted as G),[21] which is a critical property needed in device thermal design and also an important property to reflect the local atomic bonding level.[22,23] However, the thermal transport across atomic-layer interfaces is very complicated and challenging to measure since the interfacial thermal conductance is intimately related to the characteristics of the interface properties, such as its structure, bonding, geometry, *etc.*[24-26]

To date, several optical and electrical methods have been employed to measure the interfacial thermal conductance, such as the laser flash method,[27] differential 3ω method,[28] ultrafast technique with femtosecond lasers (pump-probe),[29,30] Raman-based thermal probing technique with electrical heating [31] and laser heating.[32] Particularly, Tang *et al.* developed a separate laser heating Raman-probe method that has achieved significant improvement in measurement accuracy by controlling the heating with a desired laser wavelength and continuously adjusting the laser energy without interfering the sample.[32] Besides, several theoretical methods were also applied to study the interfacial thermal transport. For example, non-equilibrium molecular dynamics (NEMD) simulation[25,33-35] was a widely used atomistic-scale modeling method for calculating the interfacial thermal conductance. A pump-probe

method using molecular dynamics simulation was employed to study the surface roughness effect on thermal transport across the graphene/Si interface.[36] Additionally, the acoustic mismatch model (AMM) [37,38] and diffuse mismatch model (DMM) [39] were also widely used to study the thermal transport across weakly coupled systems at low temperatures.[40]

Extensive research has been done for thermal transport at graphene/substrate interfaces. The results of the interfacial thermal conductance vary greatly due to different graphene preparation methods, the different interface structures, and different substrates. Ruoff *et al.* in 2009 obtained an interfacial thermal conductance of (28+16/–9.2) $MW \cdot m^{-2}K^{-1}$ for a supported graphene monolayer grown by chemical vapor deposition on copper.[41] Mak *et al.* prepared single and multilayered graphene on fused SiO_2 by mechanical exfoliation and obtained the interfacial thermal conductance ranging from 20 to 110 $MW \cdot m^{-2}K^{-1}$.[42] Chen *et al.* designed graphene flakes with different thickness sandwiched between SiO_2 layers and reported the thermal contact resistance from 5.6×10^{-9} to 1.2×10^{-9} $K \cdot m^2/W$ with temperatures from 42 to 310 K.[43] In Yue *et al.*'s work, they obtained the thermal contact resistance between epitaxial graphene and 4H-SiC as high as 5.3×10^{-5} $K \cdot m^2/W$.

For the interface thermal properties of MoS_2 and its substrate. Taube *et al.* prepared a MoS_2 monolayer supported on SiO_2/Si substrates by the mechanical exfoliation method. They obtained an increasing interfacial thermal conductance with increasing temperature from 1.94 $MW \cdot m^{-2}K^{-1}$ at 300 K to 1.25 $MW \cdot m^{-2}K^{-1}$ at 450 K.[44] In contrast with graphene, little research has been conducted on the thermal transport across the interface between MoS_2 and its substrate.

1.3 Hot Carrier Transport Effect on Thermal Energy Distribution

In semiconductor materials, electrons or holes with higher energies compared to the Fermi Energy are called hot carriers. They can be generated electrically by high electrical field or by injection through a barrier. Carrier mobility (μ) describes the motion of electrons under electric fields. Hot carriers can also be produced optically by photons with excessive energy. In this electric field free environment, the carrier diffusivity (D) is more common for the description of charge movement. The diffusion is caused and directed by the concentration gradient instead of the electric field. Hot carrier's behavior plays a significant role in modern semiconductor science. Hot carrier phenomena (*e.g.,* hot carrier effects) are important in the operation of many semiconductor devices such as laser diodes, solar cells, short-channel field-effect transistors (FETs), and high-speed devices like ultrafast photodetectors and hot-electron transistors.[17,45-47] Like free electrons in metals, transport of hot carriers is affected by various interactions between carriers and other elementary excitations (e.g. electron-phonon coupling, electron-electron collisions, the capture of carriers by impurities, exciton interactions, *etc*.) in semiconductor materials.[48] So the study of hot carrier transport properties provides important information about scattering processes in semiconductors. Additionally, extensive work has been done on hot carrier in graphene with measured D as high as 11,000 cm^2/s,[17,49-51] while the report on MoS_2 is scarce.[12]

Until now, several methods have been developed and applied to study the hot carrier transport properties (mobility or diffusivity) either under high electric field or photon-injection. Majority works focus on electrically generated hot carriers. However, the experimentally measured carrier mobility by different methods varies by almost an order of magnitude. This large discrepancy could result from many factors: the charge impurity scattering, electron-

phonon interaction, and screening by the surrounding dielectric environment.[52] Besides, even the suppression of Coulomb scattering and modification of phonon dispersion from the devices preparation process can introduce strong effect. For example, the mobility of mechanically exfoliated multilayered (15-90 nm) MoS_2 FETs with SiO_2 as a high-κ dielectric is reported in the range of 30-60 cm^2/Vs in a four-probe configuration.[53] The exfoliated multilayered (8-40 nm) MoS_2 FETs on SiO_2 have a carrier mobility from 10 to 50 cm^2/Vs by two-probe measurements for back-gated structure.[54] In contrast, the top-gated MoS_2 FETs with HfO_2 demonstrated a mobility up to about 200 cm^2/Vs, which is even higher than that of bandgap-engineered graphene.[12] During those measurements, they have to apply a voltage to the electric contact to control the electron population in the material. However, the question is still open to the role of the electrical contacts causing screening disorder in multilayered MoS_2 FETs.[53,55] The use of a high-κ gate dielectric in a top-gated device is shown to boost the carrier mobility which is caused by screening of impurities by the dielectric and/or modifications of the MoS_2 phonons in the top-gated sample.[12] Besides, the nanosheets could be potentially modified and even destroyed during the device preparation process (*e.g.*, pattern electrical contacts using electron-beam lithography) especially for ultrathin samples.[56-58] So optical-based measurements of hot carriers transport properties could give us more in-depth understanding of virgin 2D materials. For MoS_2, very little optical-based studies have been reported on electron transport. Kumar *et al*. used transient absorption microscopy to determine the diffusivity of the thermalized electron (hot electron) of bulk MoS_2 crystal to be around 4.2 cm^2/s.[59] For multilayered MoS_2, Wang *et al*. employed a spatially and temporally resolved pump-probe technique and obtained the carrier diffusivity as 20±10 cm^2/s for few-layered (1.5-2.2 nm) MoS_2 on Si.[60]

For the laser heating assist thermal probing techniques, such as Raman spectroscopy, the hot carrier transport could strongly affect the measurement results. Because the generated hot carrier would diffuse out of the active laser heating are, rather than the energy transfer to phonons, as the main mechanism of the electron cooling.[55] This diffusion could significantly extend the heating area size, especially when the laser focal spot size is comparable to the hot carrier diffusion length.

1.4 In-plane Thermal Conductivity of 2D materials

For 2D MoS_2 based devices, a high thermal conductivity will facilitate the heat dissipation during the device operation, while a low thermal conductivity can enhance the thermoelectric conversion efficiency in thermoelectric devices.[61] Besides, different from the conventional thin films, such as silicon thin films, the weak van der Waals interaction in 2D MoS_2 makes the strength of boundary scattering much weaker.[62] This will lead to a quite different thickness dependent trend. So the fast and accurate measurement of thermal conductivity in 2D MoS_2, especially the thickness dependent thermal conductivity will help to understand the energy transport from both the fundamental and applied points of view.[62-65]

Over the past decades, significant progress has been made in the thermal conductivity measurement of 2D MoS_2 either by experiment or theoretical simulation. Some well-known experiment techniques include the 3ω method,[66] the pump-probe thermoreflectance technique,[67] and confocal micro-Raman technique.[68,69] For theoretical methods, molecular dynamics (MD) simulation using Stillinger-Weber potential [63] and first-principles-driven approaches [61,70] are widely used. Especially, experimental works for few-layer MoS_2, the results are ranging from 15 W/m·K to 100 W/m·K.[65,71-74] Just for single layer, 34.5 W/m·K (ref. 64) and 84 W/m·K (ref. 75) have been reported. Since both sample quality and experiment

conditions are different, the direct comparison among those results will be less convincing. Besides, the results contain large experimental errors from several mechanisms. In the 3ω method and pump-probe technique, the sample post-processing (e.g., metallic layer deposition and metal lines on the sample surface) makes the results impossible to reflect the intrinsic thermal conductivity of 2D materials. So the non-invasive Raman based thermal probing technique is more favorable.

However, there are still some challenges and possible origins of the measurement errors which limit its effective and numerous application.[76] First, in the confocal micro-Raman technique, the laser power is absorbed and then conducted by the 2D MoS_2. The accuracy of the measured thermal conductivity is directly connected to the laser absorption which is related to the interaction between a material and incident light and varies a lot from sample to sample.[64,65] So the reported scattered or geometry dependent thermal conductivity value could partially come from laser absorption evaluation.[62] Second, as with all the other thermal measurements, the experiment errors come from the values for the interfacial thermal resistance between the 2D MoS_2 and its substrate (R). Even though R is very small for most of the time, the accurate determination and consideration of the interface thermal resistance are very crucial for the 2D MoS_2 thermal conductivity study. Either referring the R value from other independent experiments or simply neglecting the effects of R could introduce great and yet unevaluated errors. Third, for semiconductor 2D materials just like MoS_2, the optically generated hot carriers can strongly contribute to the thermal diffusion and heat dissipation during the micro-Raman measurement.[77] The effect from the hot carrier diffusion on thermal transport has not been fully taken into account before. This usually leads to an underestimated heating area because the hot carrier diffusion could significantly extend the heating size. As a

result, an overestimated laser heating flux could lead to inaccurate thermal properties evaluation. At last, the temperature calibration coefficient of the targeted 2D materials has to be obtained to evaluate the absolute temperature. This gives very large errors and increased the uncertainty of the measured thermal conductivity in the micro-Raman experiment.[65,78] Considering these sources of uncertainty, the uncertainty of the measured thermal conductivity could be as large as 40% by confocal micro-Raman technique.[79,80]

1.5 Scope of Present Work

Firstly, we present a detailed temperature and laser power dependent micro-Raman spectroscopy study of different layers MoS_2 nanosheets. We measure the interfacial thermal conductance (G_k) between few to tens of layered MoS_2 and its c-Si substrate. At room temperature, we observe G_k increases with increasing layers of MoS_2. Furthermore, we find that the number of layers (thickness) of MoS_2 deeply affects the film corrugation, morphology, and interfacial thermal conductance. The MD simulation is also conducted to better interpret our results. Detail for this thickness dependent interfacial thermal conductance study is in Chapter 2.

Secondly, in chapter 3, the hot carrier effect on thermal energy distribution is identified by the local temperature from the Raman spectroscopy by varying the laser heating size. This effect is taken into account for studying the interface energy transport for the first time. For four sub-10 nm thick MoS_2 nanosheets on c-Si substrate, by a new developed Raman-based technique, we simultaneously determine the hot carrier diffusivity and interface thermal resistance. Unlike studies by electric techniques where the mobility of carriers was measured under an external electric field, we characterize the hot carrier diffusion caused by density gradient without making any electric contact to sample or exposing it to an electric field.

Therefore, this technique eliminates the detrimental effect of direct contact and measures the intrinsic carrier transport properties of materials.

For optical-based measurement of materials' thermal properties, the optical properties of the samples are the must-know parameters. They are related to the interaction between a material and incident light and vary a lot from sample to sample. Especially, for real 2D interface structure, a tiny change of the local spacing can significantly change the laser optical absorption, leading to large measurement errors. To this end, based on above two works, we develop a novel and more advanced technique: energy transport state-resolved Raman (ET-Raman) to study the 2D materials' thermal response under different laser heating states. By this technique, we could also determine *R* and *D* but completely eliminate the large errors introduced by laser absorption evaluation and Raman property temperature coefficient calibration. *D* and *R* could be determined by just comparing the Raman wavenumber shift measured from different energy transport states (in time and space domains). Therefore, this technique is believed to eliminate the errors brought in by local optical absorption evaluation, temperature coefficient calibration, and the effects from electrical contact. Therefore it provides a far more accurate understanding of interface energy coupling and hot carrier diffusion. This technique is successfully applied here to determine *D* and *R* of seven FL MoS_2 samples on c-Si substrate and six FL MoS_2 samples on glass substrate. The ET-Raman for different substrates has different data processing processes, and they will described in chapter 4 and chapter 5.

At last, for the in-plane thermal energy transport, the hot carrier (*D*) and in-plane phonon (*k*) have different contribution and follow different physical rules. Besides, for the ET-Raman developed to determine *D* and *R*, we have to input the *k* value referring others work

that may not be exactly suitable for our case. To this end, based on ET-Raman technique, we developed a Five-State ET-Raman technique to differentiate these two effect and simultaneously determine the k, D, and R for eight FL MoS_2 samples ranging from 2.4 to 37.8 nm thick on glass substrate. Besides, the large errors introduced by laser absorption evaluation and Raman property temperature coefficient calibration can be completely eliminated. Therefore it provides a far more accurate understanding of the intrinsic thermal property of 2D materials. In addition, this systematic non-contact thickness-dependent thermal conductivity study reveals the intrinsic properties of FL MoS_2 and provides a practical guide for further advancing MoS_2 based device technologies.

CHAPTER 2. INTERFACE THERMAL ENERGY TRANSPORT: EFFECT OF MOS2 THICKNESS

In this chapter, we report a systematic investigation of interfacial thermal conductance (G_k) between few to tens layered mechanical exfoliated molybdenum disulfide (MoS_2) and crystalline silicon (c-Si). Details for sample preparation and characterization are presented in Section 2.1. As given in Section 2.2, based on Raman spectroscopy, we find G_k at room temperature increases with increased layer numbers of MoS_2 from 0.974 MW/m^2·K to 68.6 MW/m^2·K. The higher G_k of thicker samples reveals their better interface contact with the substrate, leading to accordingly improved interfacial energy coupling. Molecular dynamics (MD) simulations are conducted to interpret and compare with the experimental observations in Section 2.3. MD simulations predict a thermal conductance in the range of 53-77 MW/m^2·K, which agrees well with the upper bound G_k measured in our work. The thickness dependence of measured G_k reflects the improved interface spacing for thicker MoS_2 samples. This phenomenon is further confirmed by the Raman intensity enhancement study by the interface spacing and local optical interference calculations.

2.1 Sample Preparation and Characterization

2.1.1 Preparation of MoS_2 Nanosheets by Mechanical Exfoliation Method

The layered MoS_2 samples through all my work are prepared by micromechanical cleavage of a bulk MoS_2 (429MS-AB, molybdenum disulfide, small crystals from USA, SPI Suppliers). Several methods have been reported to prepare atomically thin MoS_2 nanosheets, such as chemical vapor deposition and liquid exfoliation, etc. Among these, mechanical exfoliation is widely used and the most efficient way to produce clean, highly crystalline and

atomically thin nanosheets of layered materials for investigating of their intrinsic thickness-dependent properties.[81]

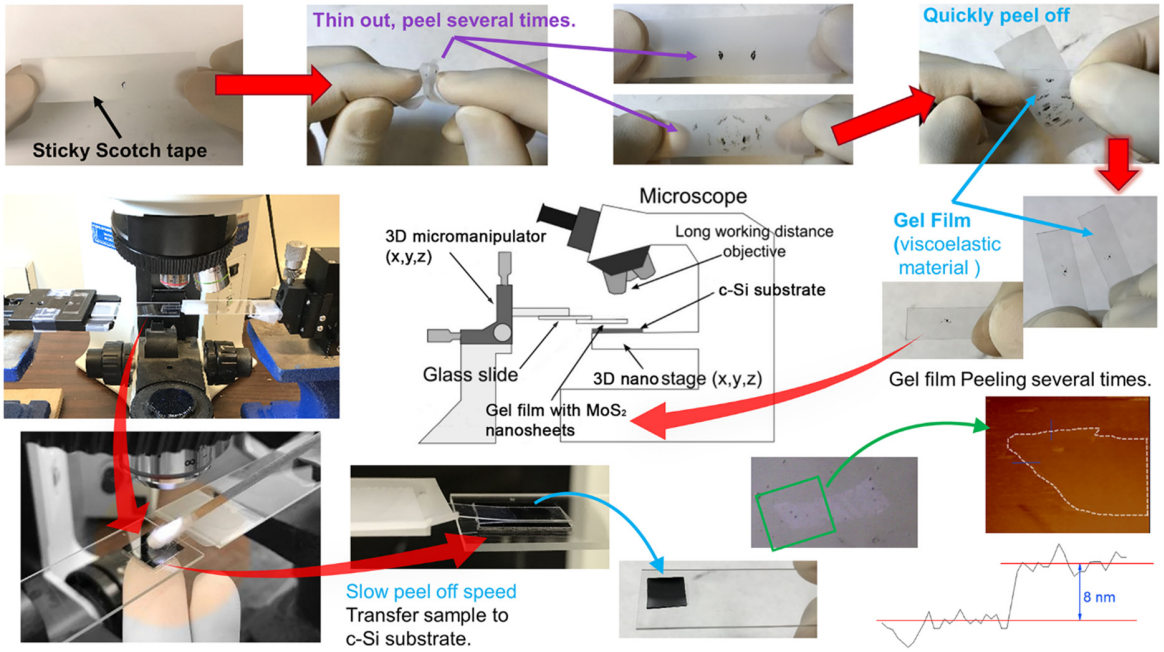

Figure 2.1 Micromechanical cleavage two-dimensional MoS_2 preparation process.

As in the typical mechanical exfoliation process, as shown in Fig. 2.1, we first put a small piece of bulk MoS_2 on the sticky side of a piece of ordinary adhesive Scotch tape and then peel off appropriate thin MoS_2 crystals. After repeating the peeling process several times, we identify some relatively thin crystals on the Scotch tape with microscope. Then we lay one gel film (Gel-Film, PF-20/1.5-X4, Gel-Pak) on the crystals and gently rubbed the back of the gel film by using tools such as a plastic plate to further cleave the crystals. The third step is to quickly peel back the gel film from the Scotch tape to transfer the crystals. Then we apply crystals inked gel film to a freshly cleaned c-Si substrate and carefully rub the back of gel film again. At last, by slowly peeling off the gel film from the substrate by a dedicated setup using 3D micromanipulator, several MoS_2 nanosheets with different thickness are left there.[82] The

size of layered MoS_2 nanosheets ranges from 3 to 15 μm. Optical microscope (Olympus BX53), atomic force microscope (AFM) and Raman spectroscopy are used to locate the MoS_2 nanosheets.

2.1.2 Surface Morphology and Layer Thickness Study by AFM

Figure 2.2 shows AFM images of seven cleaved samples of multilayer MoS_2 nanosheets. AFM is also used to measure the thickness of these MoS_2 samples. We choose the contact mode of AFM instead of tapping or other modes to avoid possible artifacts in the nanosheet thickness measurements.[83] Because we currently cannot do the sample thickness control, there is only one sample for each thickness level. In Fig. 2.2, for each sample, the left figure gives the 2D contour. The MoS_2 sample is marked by the white dashed curves. The two blue lines indicate the edges where the height is measured [shown in the figures in the middle, e.g. Fig. 2.2 (a-1) and Fig. 2.2 (a-2)]. The blue dashed square indicates the location for detailed MoS_2 surface morphology study. This morphology study is shown in the top figure on the right, e.g., Fig. 2.2 (a-3). The bottom figure on the right [e.g., Fig. 2.2 (a-4)] shows the height variation along the blue line in the top figure on the right [e.g., Fig. 2.2 (a-3)].

Take the AFM image of the 45 nm-thick sample as an example [Fig. 2.2 (a)], we explain the surface morphology characterization results. We can find that the surface height varies as much as 9.5 nm which indicates the existence of corrugations and/or ripples on the MoS_2 layers [Fig. 2.2 (a-4)]. This variation is also partly induced by the non-uniform layer number of the sample. For other six samples, the surfaces are found much smoother with a height measurement noise of around 0.3 nm. The average height variation ranges from 0.94 nm to 0.43 nm and the surface becomes smoother for thinner MoS_2 samples. The noise in the AFM measurement (~0.5 nm) is obvious for the 4.2 nm thick sample and the white spots in Figs. 2.2

(d, f) are residual from gel films. In the experiment, the laser spot is on the MoS_2 sample completely. From all the figures, it is conclusive that the surface of MoS_2 sample is atomically smooth, except for the first sample (45 nm). In Fig. 2.2 (f), we can find that on the large sample there are also some small flakes. The large MoS_2 sample has a thickness of 5 nm [Fig. 2.2 (f-1) and 1(f-2)]. Besides, the surface of the substrate we use is same to Tang *et al.*'s work.[32] As shown in Fig. 2.2 (b) of his work, when considering the AFM measurement noise, the surface of the c-Si is very flat and we believe that there is no protruding points on it. In our interface characterization, the laser spot is focused on the area without extra flakes, like the area indicated by the dashed square.

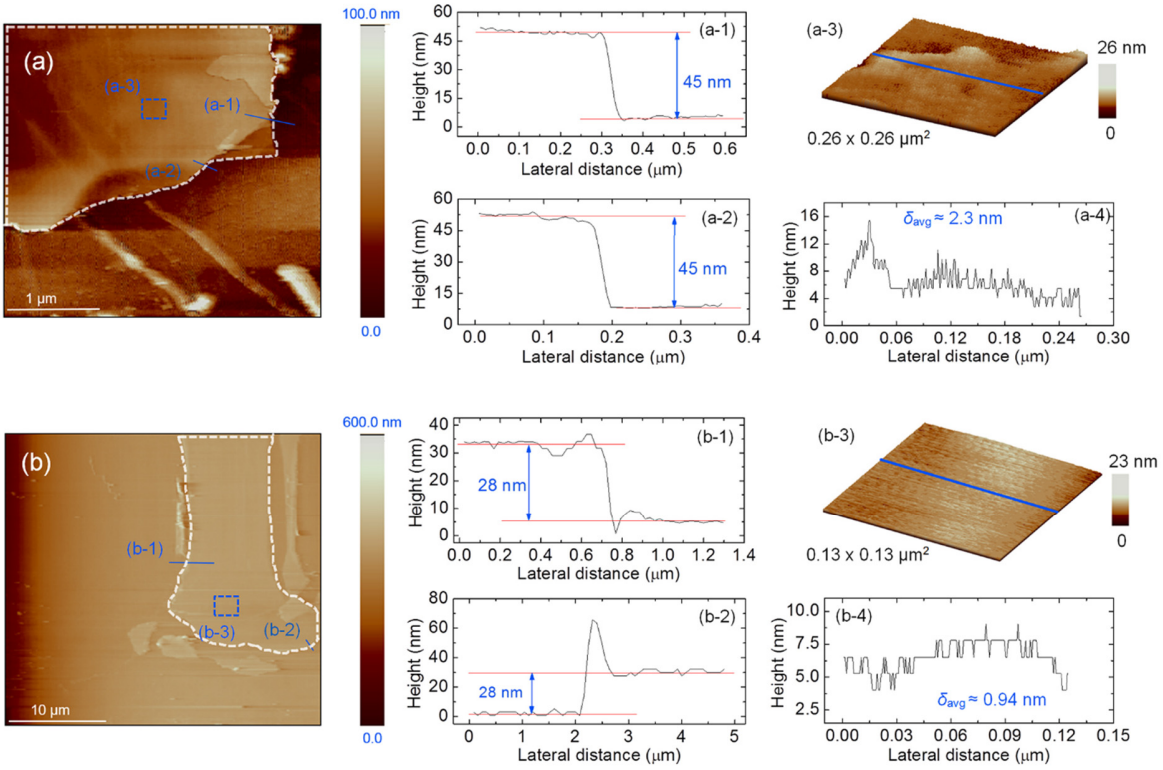

Figure 2.2 Sample thickness measurement and surface characterization.

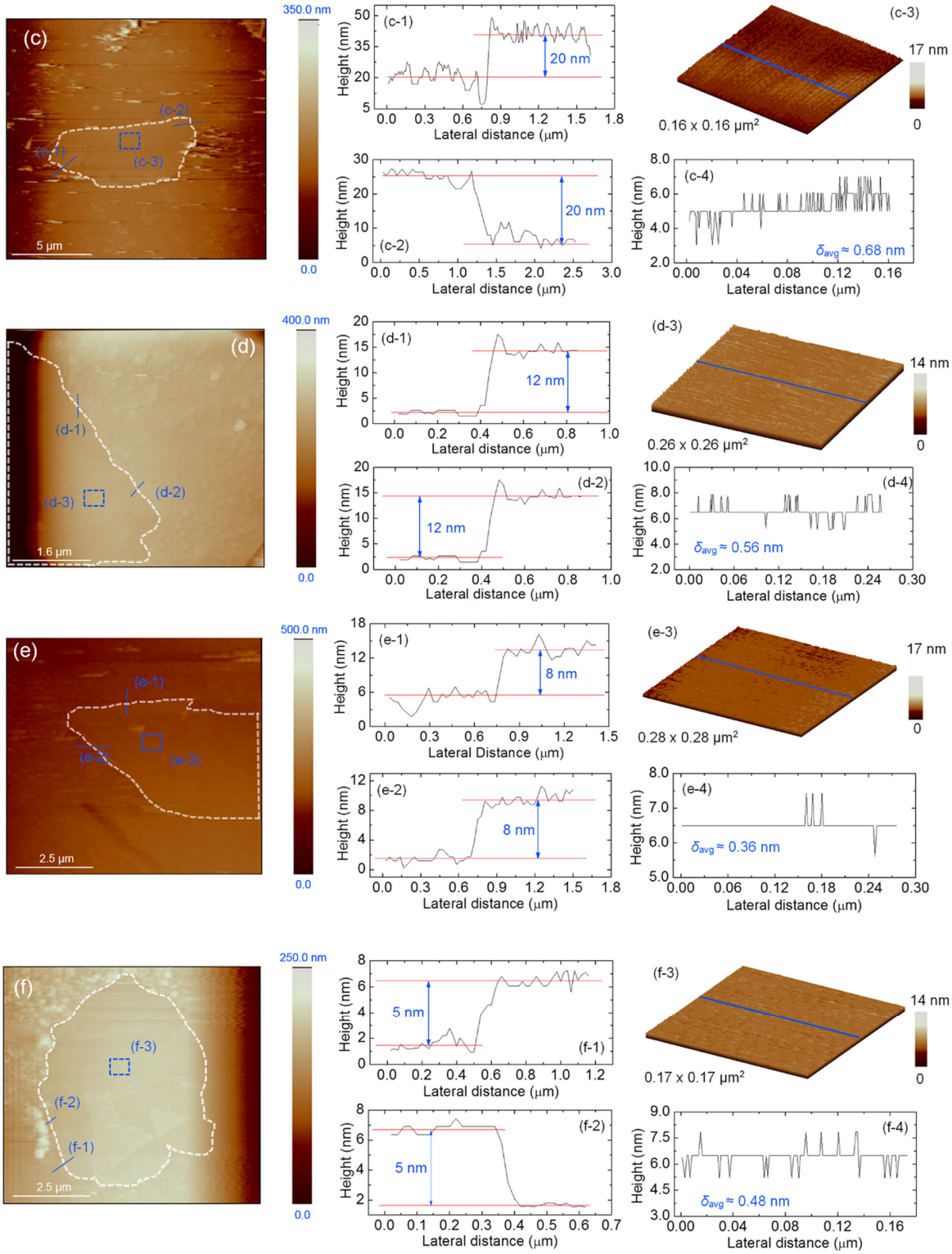

Figure 2.2 (continued)

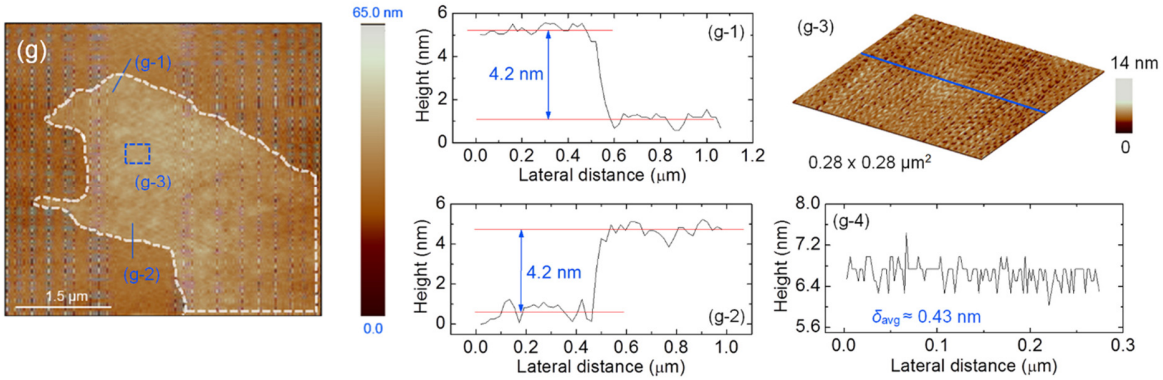

Figure 2.2 (continued)

2.2 Experimental Design and Physical Model for Interface Characterization

2.2.1 Experiment Setup

Raman scattering studies are conducted by using a BWTEK Voyage confocal Raman microscope system using a longitudinal single mode continuous-wave (CW) laser with an excitation wavelength of 532 nm as shown in Fig. 2.2 (a). The laser is introduced to the Raman system and its energy is adjusted by a neutral-density (ND) filter. Search and identifying of the MoS_2 nanosheet sample on c-Si under microscope is realized using a 3D nano-stage (MAX313D, Thorlabs, Inc.) with a resolution of 5 nm. The laser beam is focused on the center of the sample and the laser power is varied between 2.61 mW and 12.1 mW to introduce different heating levels in the MoS_2 samples. The absorbed energy is conducted away across the MoS_2/c-Si interface to the substrate. We use the Raman spectrometer to measure the temperature of MoS_2 and c-Si simultaneously. Based on the temperature difference between MoS_2 and c-Si, and the absorbed laser power, we can directly determine the interfacial thermal conductance. Shown in Figs. 2.3 (b) (c) are the laser energy distribution (contour and 3D) under a 20× objective lens. From Fig. 2.3 (c) is clear that the energy distribution can be well described by a linear line from the center of the spot to its edge. Under 20×, the spot size is around 5 μm.

Under 50×, the spot size is around 1.9 μm. Quantitative definition of the spot size depends on how it is evaluated. Below when we discuss the physical model, the spot size will be discussed more. Physical models for detailed data processing will be described below, too. In our experiment, depending on the sample size and thickness, either 20× or 50× objectives is used. Details are summarized in Table 2.1.

Table 2.1 Temperature coefficient of different layered MoS_2 nanosheets and c-Si under the corresponding objective lens, and interfacial thermal conductance.

Layer number of MoS_2, objective lens	G_k by Raman parameters of A_{1g} mode (MW/m^2K)	Temperature coefficient χ_T (cm^{-1}/K)		
		A_{1g} mode	E^1_{2g} mode	c-Si
7 L, 50× lens	0.974±0.158	-(0.0143±0.0005)	-(0.0146±0.0004)	-(0.0191±0.0017)
8 L, 20× lens	1.05±0.172	-(0.0110±0.0005)	-(0.0111±0.0004)	-(0.0195±0.0018)
13 L, 20× lens	6.00±1.46	-(0.0153±0.0014)	-(0.0158±0.0008)	-(0.0190±0.0010)
20 L, 20× lens	7.58±1.06	-(0.0237±0.0013)	-(0.0299±0.0019)	-(0.0248±0.0011)
33 L, 20× lens	17.5±3.02	-(0.0174±0.0013)	-(0.0221±0.0275)	-(0.0271±0.0004)
47 L, 20× lens	21.0±3.68	-(0.0221±0.0013)	-(0.0275±0.0015)	-(0.0353±0.0016)
75 L, 50× lens	68.6±9.14	-(0.0174±0.0010)	-(0.0194±0.0012)	-(0.0355±0.0006)

2.2.2 Effective Thermal Conductance between MoS_2 and c-Si

Considering the non-uniform distribution of the laser energy in space [Fig. 2.3 (b) and (c)], the temperature distribution in the MoS_2 nanosheet measured in the experiment could be obtained from following heat diffusion equation in the cylindrical coordinate:

$$k_s t \frac{1}{r}\frac{d}{dr}\left(r\frac{dT}{dr}\right) - G_e(T_1 - T_2) + I_a = 0 \tag{2.1}$$

Where G_e is the effective interfacial thermal conductance per unit area. T_1 is the temperature rise of MoS_2 nanosheet upon laser heating, T_2 the temperature rise of c-Si. Note

the effective interfacial thermal conductance (G_e) is defined based on the effective/average temperature measured in the experiment: T_1 and T_2. Since the measured temperatures do not represent the temperature of MoS_2 and c-Si at locations immediately adjacent to their interface, the effect of temperature distribution in the thickness direction for MoS_2 and c-Si will be considered to find the true interfacial thermal conductance. I_a (W/m^2) represents the absorbed laser power per unit area in MoS_2. This is calculated according to the TMM.[84] The refractive index of air is 1. The refractive index and extinction coefficient of MoS_2 are taken as 5.2 and 1.1 when the wavelength (λ) of the laser beam is 532 nm.[85] The refractive index and extinction coefficient of c-Si are 4.15 and 0.05 when λ is 532 nm.[32] $k_s = 52$ W/m·K is the in-plane thermal conductivity of MoS_2 nanosheet.[65] r is the radial position measured from the center of the laser beam, r_0 the radius of the laser beam spot, and t the MoS_2 nanosheet thickness. In our experiment, the measured temperature rise is Raman/laser intensity weighted average over the laser spot size and can be expressed as

$$\overline{T} = \int_0^{r_0} I_a T dA / \int_0^{r_0} I_a dA. \tag{2.2}$$

To reflect this weighted average temperature in above equation, we multiply I_a on both sides of Eq. 2.1, do the integral over the laser spot area, and then divide them by $\int_0^{r_0} I_a dA$, finally we have

$$\frac{k_s t}{Q} I_{a(\max)} \overline{T_1} - G_e(\overline{T_1} - \overline{T_2}) + \int_0^{r_0} I_a^2 dA / \int_0^{r_0} I_a dA = 0. \tag{2.3}$$

Here $I_{a(\max)}$ is the absorbed laser intensity in the center of the laser spot. In the above integral, we take one assumption that at the edge of the laser spot, the temperature rise is much smaller than the average temperature rise. This is true since the sample is very thin, the heat

conduction/transfer along the thickness direction in MoS_2 is much larger than that in the in-plane direction. In the above equation, the term $\int_0^{r_0} I_a^2 dA / \int_0^{r_0} I_a dA$ in fact gives an equivalent heat flux (q''_{eff}) we can obtain from our laser beam distribution and use it to evaluate G_e. Fig. 2.3(b) and (c) show the contour and 3D profile of the laser beam for non-uniform laser distribution in space. Based on the calculated effective laser energy density, we could further evaluate the laser beam size as $A_{beam} = (\int I_a dA)^2 / \int I_a^2 dA$. Using this definition, the spot size is calculated as 35.7 μm^2 for 20× and 5.90 μm^2 for 50×. In our experiment, q''_{eff} for different laser energy levels are evaluated and used to suppress experimental noise and determine G_e.

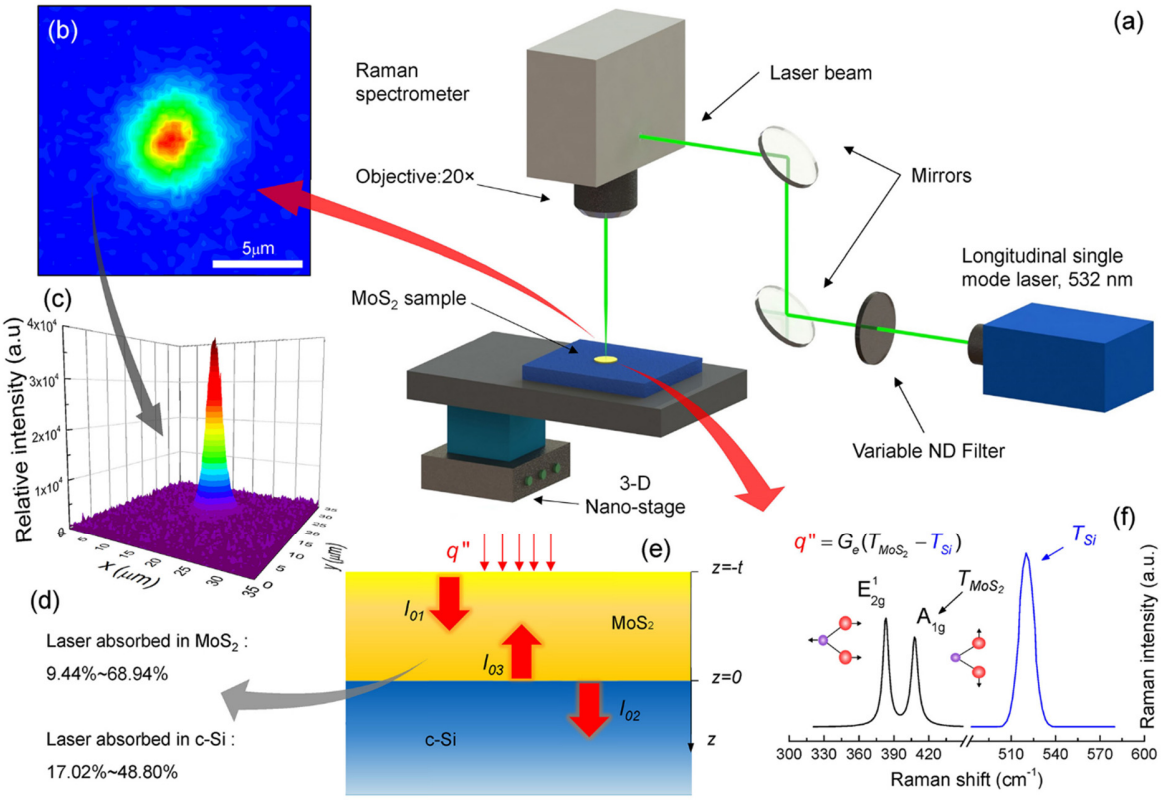

Figure 2.3 Schematic of the Raman experiment setup for characterizing the MoS_2/c-Si interface energy coupling.

As shown in Fig. 2.3 (b) and (c), the laser intensity can be well represented with a linear distribution from the spot center to its edge. Therefore, we can calculate the total absorbed laser power Q in Eq. 2.3 as

$$Q = \int_0^{r_0} 2\pi I_a r dr = \int_0^{r_0} I_{a(\max)}(1-\frac{r}{r_0})2\pi r dr = \frac{I_{a(\max)}}{3}\pi r_0^2. \tag{2.4}$$

Finally, the effective interfacial thermal conductance can be described as

$$G_e = \frac{3k_s t/(\pi r_0^2)\cdot \overline{T_1} + q''_{eff}}{\overline{T_1} - \overline{T_2}}. \tag{2.5}$$

In the experiment, by using only one incident laser energy, we can measure $\overline{T_1}$, $\overline{T_2}$ and q''_{eff}, and then determine G_e. To suppress the experimental noise, we use different incident laser energy levels, and plot how $\overline{T_1}$ and $\overline{T_2}$ linearly vary against q''_{eff}. Instead of using their absolute value, the slope of the relation: $\partial\overline{T_1}/\partial q''_{eff}$ and $\partial\overline{T_2}/\partial q''_{eff}$ are used to determine the effective thermal conductance as

$$G_e = \frac{3k_s t/(\pi r_0^2)\cdot \partial\overline{T_1}/\partial q''_{eff} + 1}{\partial\overline{T_1}/\partial q''_{eff} - \partial\overline{T_2}/\partial q''_{eff}}. \tag{2.6}$$

The quantity $\partial\overline{T}/\partial q''_{eff}$ could be experimentally obtained using following relation:

$$\frac{\partial\overline{T}}{\partial q''_{eff}} = \frac{\partial\omega}{\partial q''_{eff}} \Big/ \frac{\partial\omega}{\partial T} = \frac{q''_{eff}}{P}\chi_p\chi_T^{-1}, \tag{2.7}$$

where χ_T and χ_p is first-order temperature coefficient and power coefficient for the Raman shift of MoS_2 and c-Si. P is the laser power reaching the sample surface. The temperature coefficients of the Raman shift are obtained from the separate temperature calibration experiments. In our experiment, eight different incident laser powers are introduced to achieve accurate and linear power coefficients for MoS_2 and c-Si.

2.2.3 Evaluation of the Real Interfacial Thermal Conductance

In our experiment, as mentioned before, the measured temperatures of MoS_2 and c-Si are not the ones immediately adjacent to their interface. Rather they have the effect of the temperature distribution in the thickness direction for both MoS_2 and c-Si, and are discussed as below.

Considering the finite thickness of MoS_2, there is a temperature gradient existing in MoS_2 caused by the exponential laser energy absorption and heat conduction in the MoS_2 nanosheet. The penetration depth of the Raman laser in MoS_2 is $\tau_1 = \lambda / (4\pi\kappa_{\mathrm{MoS_2}})$. At $\lambda = 532$ nm, the extinction coefficient $\kappa_{MoS_2} = 1.1$ for MoS_2, we have $\tau_1 = 38.5$ nm. Following the coordinate definition in Fig. 2.3 (e), we could describe the energy absorbed in MoS_2 nanosheets within $(-t, z)$ as $I_{\mathrm{MoS_2}}(z) = I_{01}[1 - e^{-(z+t)/\tau_1}]$. In our work, since the sample is very thin, the heat conduction in the thickness direction is dominant over that in the in-plane direction. Also as indicated in Fig. 2.3 (e), the reflected laser beam at the interface is negligible in MoS_2 in terms of absorption from the multiple reflections calculation. As a result, the temperature distribution within MoS_2 could be expressed as $T_1(z) = T_1\big|_{z=0} + \int_{-t}^{0} I_{01}/k_{s'}[1 - e^{-(z+t)/\tau_1}]dz$, where I_{01} is the laser intensity just entering MoS_2 from the top surface. $k_{s'}$ is the cross-plane thermal conductivity of MoS_2 nanosheets which has been obtained as 2 W/m·K.[72] Actually, the Raman-based temperature measurement is an intensity-weighted average temperature in the thickness direction. So $T'_{exp} = \int_{-t}^{0} T_l(z) e^{-(z+t)/(\tau_1/2)} dz \Big/ \int_{-t}^{0} e^{-(z+t)/(\tau_1/2)} dz = T_1\big|_{z=0} + f_1(t) I_{01}$. $f_1(t)$ is a function of thickness t and given as:

$$f_1(t) = \frac{\tau_1(-2e^{-3t/\tau_1} + 3e^{-2t/\tau_1} + 6e^{-t/\tau_1} - 7) + 6t}{6k_{s'}(1 - e^{-2t/\tau_1})}. \tag{2.8}$$

The equivalent heat conduction resistance (R_1) caused by the finite thickness is

$$R_1 = \frac{\int f_1(t) I_{01} I_a dA / \int I_a dA}{[3k_s t/(\pi r_0^2)] \cdot \overline{T_1} + q''_{eff}} = \frac{f_1(t) \cdot q''_{eff} / (1 - e^{-t/\tau_1})}{[3k_s t/(\pi r_0^2)] \cdot \overline{T_1} + q''_{eff}}. \quad (2.9)$$

For c-Si, similar to MoS_2, its measured temperature is not the temperature immediately next to its upper surface either, but an average temperature within the focal depth of the Raman probing laser. The temperature distribution reflects the effects of the heat flux from the MoS_2 sheet plus the laser energy absorption in c-Si. The temperature rise distribution induced by the heat flux from MoS_2 is linearly distributed against the thickness in the region close to the c-Si surface. The penetration depth of the Raman laser in c-Si is $\tau_2 = \lambda/(4\pi\kappa_{Si})$. With $\kappa_{Si} = 0.05$ for silicon, we have $\tau_2 = 820\,\text{nm}$. As the Raman excitation laser is focused on the c-Si surface and considering the Raman intensity weighted average for temperature measurement, we can calculate the measured temperature of c-Si as $T_{\exp} = \int_0^\infty T_2(z) \cdot e^{-z/(\tau_2/2)} dz \Big/ \int_0^\infty e^{-z/(\tau_2/2)} dz$ $= T_2\big|_{z=\tau_2/2}$,[32] where z is the distance from c-Si surface as shown in Fig. 2.3(e). This means the extra temperature of c-Si measured in the experiment is equal to the value at $z = \tau_2/2 = 410$ nm. The equivalent heat conduction resistance of c-Si across this distance is $R_2 = \tau_2 / \{2k_{Si}[3k_s t/(\pi r_0^2) \cdot \partial\overline{T_1}/\partial q''_{eff} + 1]\}$, which we should subtract from the measured effective thermal resistance (G_e^{-1}).

Finally, the laser energy transmitted from MoS_2 to c-Si also causes a temperature gradient in c-Si because of the laser absorption. As shown in Fig. 2.3 (e), the energy absorbed in c-Si within (0, z) could be described as $I(z) = I_{02}(1 - e^{-z/\tau_2})$ and the temperature distribution could be expressed as $T_2(z) = T_2\big|_{z=0} - \int_0^z I_{02}/k_{Si}(1 - e^{-z/\tau_2})dz$. Here I_{02} is the laser intensity just

entering c-Si from the interface, and is expressed as $I_{02}(1-e^{-t/\tau_2})$ after neglecting the weak reflection at the local interface. Similar to MoS_2, the Raman-based temperature measurement in c-Si is also an intensity-weighted temperature for the laser spot. So this effect is expressed as $T'_{\exp}=\int_0^\infty T_2(z)\cdot e^{-z/(\tau_2/2)}dz\Big/\int_0^\infty e^{-z/(\tau_2/2)}dz=T_2\big|_{z=0}-I_{01}(1-e^{-t/\tau_1})\tau_2/6k_{Si}$. The equivalent heat conduction resistance caused by this effect is

$$R_3=\frac{\int[I_{01}(1-e^{-t/\tau_1})\tau_2/(6k_{Si})\cdot I_a]dA/\int I_a dA}{3k_s t/(\pi r_0^2)\cdot\overline{T_1}+q''_{eff}}=\frac{q''_{eff}\tau_2}{6k_{Si}[3k_s t/(\pi r_0^2)\cdot\overline{T_1}+q''_{eff}]}. \quad (2.10)$$

To the end, the real interfacial thermal conductance G_k should be:

$$G_k=\frac{3k_s t/(\pi r_0^2)\cdot\overline{T_1}+q''_{eff}}{T_1\big|_{z=0}-T_2\big|_{z=0}}=\frac{1}{G_e^{-1}-R_1-R_2-R_3}. \quad (2.11)$$

2.3 Results and Discussion

2.3.1 Raman Characterization of MoS_2 Nanosheets

For all the seven MoS_2 samples, first, we conduct Raman characterization under the same conditions to study the sample's difference in terms of Raman properties. A 532 nm laser under a 50× objective lens is used in the Raman spectroscopy study. The samples are excited with 3.28 mW laser power and the integration time is 10 s. Fig. 2.4 (a) shows the strong signals from both E^1_{2g} and A_{1g} vibration modes in ambient environment. The E^1_{2g} mode is associated with in-plane opposite vibration of two sulfur atoms with respect to the molybdenum atom, whereas the A_{1g} mode is associated with the out-of-plane vibration of only sulfur atoms in opposite directions.[44] We observe the E^1_{2g} (~383 cm^{-1} for thin MoS_2) and A_{1g} (~407 cm^{-1} for thin MoS_2) modes from curve fitting by using the Lorentzian function. Instead of using Gaussian function, we find using Lorentzian function could better determine the Raman

parameters of MoS_2. Fig. 2.4(b) depicts the Gaussian-fit Raman spectra of c-Si with different thickness MoS_2 sample on its surface. The c-Si Raman peak position at around 521 cm^{-1} determined from the Gaussian fit is used as an intrinsic Raman shift for temperature determination of the c-Si substrate. As shown in Fig. 2.4 (c), we could observe the thickness dependence of the Raman intensity of Raman active E^1_{2g} and A_{1g} modes in MoS_2 nanosheets. When the sample is thicker, the Raman signal of MoS_2 is stronger and that of c-Si is weaker (inset). For the Raman intensity of MoS_2, it does not increase with the sample thickness linearly since the laser absorption in MoS_2 follows an exponential function. The trend indicates that when the thickness of MoS_2 goes further, intensity saturation will be reached. For the Raman intensity of c-Si, when the MoS_2 layer is thicker, less laser will reach the substrate to excite Raman signals. In addition, less percentage of the Raman signal will have the chance to reach out and be detected because some Raman signal is also absorbed by MoS_2 nanosheets.

Figure 2.4 (d) displays the thickness dependence of Raman shift of two Raman modes in MoS_2 nanosheets. The Raman shift of E^1_{2g} mode softens while that of the A_{1g} mode has a blue shift with the increased layer number. This is mainly because the interlayer Van der Waals force in MoS_2 layers becomes stronger with increased layer number, causing the decrease of the force constant for A_{1g} mode and structure changes. As for the contrary behavior in E^1_{2g} mode of MoS_2, it suggests that the increased interlayer Van der Waals force may play a minor role. The stacking induced structure change or the possible presence of additional interlayer interactions such as the long-range Coulomb interlayer interactions in layered MoS_2 nanosheets may dominate the change of atomic vibration. We also plot the Raman shift difference [$\Delta\omega$, in cm^{-1} unit] as a function of the layer number in Fig. 2.4 (d). In the past, the Raman shift difference has been found to be a convenient diagnostic of the layer thickness of

MoS_2 nanosheets. Our result is consistent with results and predictions of *Lee et al.*'s work : $\Delta\omega$ =25 cm^{-1} is for about 7 layers and $\Delta\omega$ increases with increasing sample thickness.[86]

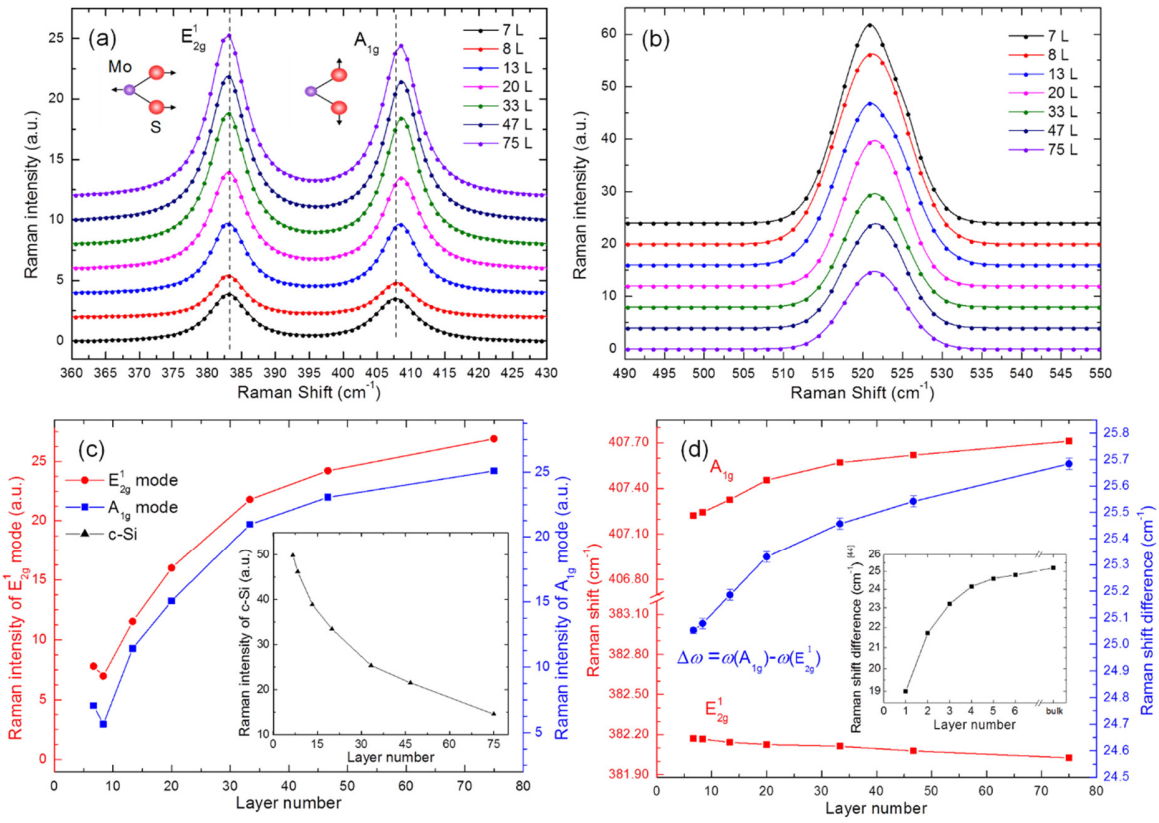

Figure 2.4 Raman characterizations of seven MoS_2 nanosheet samples.

In the Raman experiments, for each sample, eight room-temperature Raman spectra are collected at the laser power ranging from 2.61 to 12.1 mW. This heating power variation is designed to study the Raman spectrum change under the heating and to significantly suppress the noise. Fig. 2.5 (a) shows the five representative Raman spectra and their corresponding Lorentizian fits collected from the MoS_2 sample of 4.2 nm thickness. As the laser power increases, the Raman wave number of both E^1_{2g} and A_{1g} modes shift to left (red-shift). These changes indicate the local temperature of the sample surface goes higher under a higher laser

power. The Raman shift for the two vibration modes as a function of incident laser power are plotted in Fig. 2.5 (c). In our specified laser power range, it is observed that the Raman shift linearly depends on the laser power by $\Delta\omega = \omega(P_2) - \omega(P_1) = \chi_P(P_2 - P_1) = \chi_P \Delta T$. χ_P is the first-order laser power coefficient for MoS_2 vibration mode and P is the laser power. The fitted χ_P for E^1_{2g} and A_{1g} modes are quite close, –(0.182±0.010) cm^{-1}/mW and –(0.192±0.012) cm^{-1}/mW, respectively.

We also calibrate the temperature coefficients of MoS_2 and c-Si Raman spectra to determine the local temperature during the interfacial thermal conductance experiment. This calibration is conducted for each sample considering the possible sample-to-sample difference. In the calibration experiments, the MoS_2/c-Si sample is placed on a heated stage and the sample's temperature is controlled by a voltage transformer that powers the heater, and monitored by a thermocouple. Raman spectra of both MoS_2 and c-Si are collected after the sample's temperature reaches a stable reading. Fig. 2.5 (b) shows four representative Raman spectra and their corresponding Lorentzian fits with the temperature ranging from 310 to 415 K. The Raman shift of both E^1_{2g} and A_{1g} modes decreases against increased temperature.

Figure 2.5 (d) shows the temperature coefficients of the Lorentzian-fit Raman peaks from 292 to 415 K for both E^1_{2g} and A_{1g} modes. At higher temperatures, all layers expand with the same rate leading to a nearly linear decrease of the Raman shift for both E^1_{2g} and A_{1g} modes. So that we could describe the Raman peak position as a function of temperature $\Delta\omega = \omega(T_2) - \omega(T_1) = \chi_T(T_2 - T_1) = \chi_T \Delta T$. χ_T is the first-order temperature coefficient for MoS_2 vibration modes and T is temperature. Here, we do not consider the higher order temperature coefficients because these terms are significant only at high temperature about 570

K and above.[65] In our experiment, the MoS_2/c-Si samples are firmly placed on the 3D nanostage and the same point of each sample is measured during temperature calibration and interfacial thermal conductance experiment. This treatment eliminates possible location-to-location structure variation and temperature coefficient variation.

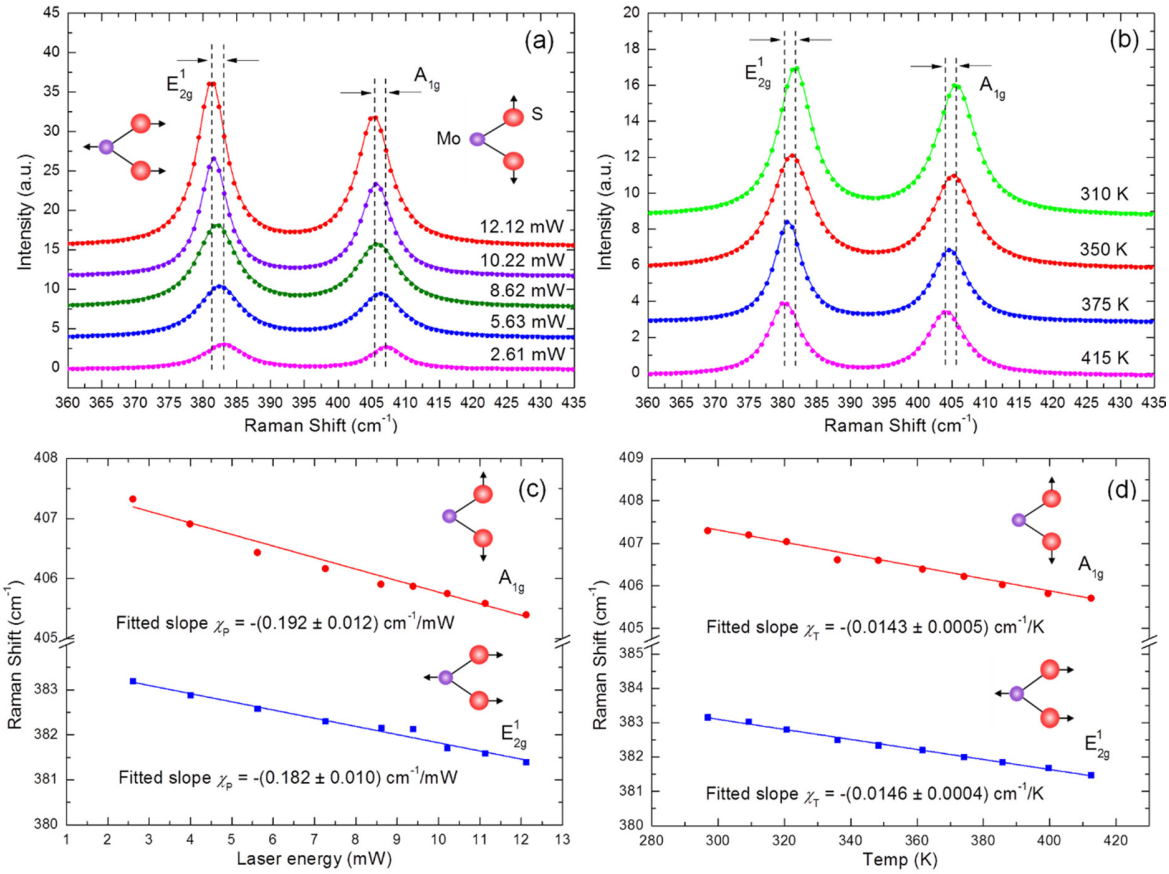

Figure 2.5 The Lorentzian-fit Raman spectra and linear fitting for Raman shift against laser power and temperature of 4.2 nm thick MoS_2 nanosheets.

The observed linear evolution of the Raman peak position with temperature is actually a manifestation of the anharmonic terms in the lattice potential energy which is determined by the phonon occupation number, the anharmonic potential energy, and the thermal expansion of the crystal. That is, the temperature effects could be approximately attributed to two factors:

energy shift of the lattice due to the anharmonic phonon-phonon interactions and the shift contribution caused by the thermal expansion of the crystal. As the lattice expands or contracts because of temperature change, the equilibrium positions of atoms are displaced and consequently the interatomic forces change. This modifies the phonon vibrational frequencies shown in the form of the Raman spectra.[87,88] In our work, the temperature coefficients difference of vibration mode E^1_{2g} and A_{1g} shown in Fig. 2.5 (a) as red and blue curves are just an indication of the different anharmonic coupling of the phonon modes. Because we prepare all the MoS_2 nanosheets samples by mechanical exfoliation, it is highly possible that wrinkles and/or ripples are introduced to the nanosheets which could result stress/strain in the nanosheets. Additionally, the MoS_2 nanosheets on c-Si substrate could be more affected by the changes in the nanosheets morphology such as wrinkles and ripples when temperature increases. This is mainly caused by the thermal expansion coefficient difference between MoS_2 and c-Si. All these combine together to result in different temperature coefficients among MoS_2 samples as shown in Fig. 2.5 (a) and Table 2.1.

Based on the first-order temperature coefficient χ_T and the power coefficient χ_P for MoS_2, we could extract the interfacial thermal resistance/conductance between MoS_2 and c-Si as shown in Figs. 2.6 (b), (c), and (d). From Figs. 2.6 (b, c), we can find that the three temperature correction equivalent thermal resistances together have bigger effects on interfacial thermal resistance (G_k^{-1}) when the sample is thicker. R_2 is roughly a constant. R_3 approaches zero while R_1 becomes larger for thicker samples. In addition, the equivalent heat conduction resistance (R_1) caused by the finite thickness of MoS_2 affects G_k^{-1} most. By subtracting all those three equivalent thermal resistances, we get that G_k^{-1} decreases by about

two orders of magnitude with increasing layer numbers of MoS_2 based on the Raman parameters of both E^1_{2g} and A_{1g} vibration modes.

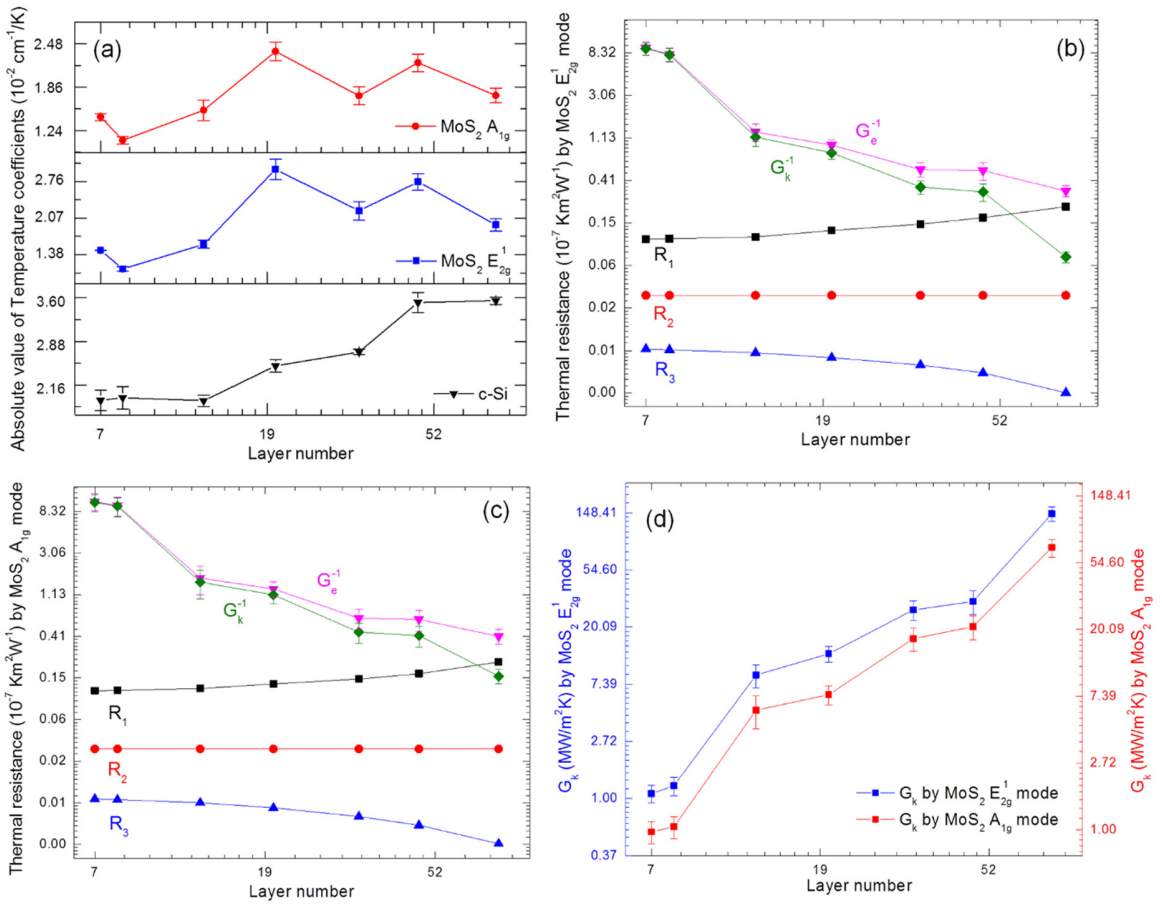

Figure 2.6 The temperature coefficients and interfacial thermal conductance results as a function of MoS_2 layer number.

From Fig. 2.6 (d), G_k obtained from E^1_{2g} and A_{1g} vibration modes are very close and follow the similar trend. Since the E^1_{2g} mode would be more affected by the interaction between the nanosheets and the substrate than the A_{1g} mode,[89] we choose the A_{1g} mode results results to evaluate the interfacial thermal conductance and elaborate the discussion. The uncertainty of our results mainly comes from the linear fit of the temperature coefficients as

shown in Table 2.1. The real interfacial thermal conductance at room temperature increases with increased layer number of MoS_2 from around 0.974 MW/m^2·K to 68.6 MW/m^2·K. The thermal conductance increases by 70 times. They are almost on the same order of magnitude as the interfacial thermal conductance of monolayer graphene supported on SiO_2 [(28+16/–9.2) MW/m^2·K].[41] The interfacial thermal conductance of MoS_2 monolayer supported on SiO_2/Si substrates was found to vary from 1.94 MW/m^2·K at 300 K to 1.25 MW/m^2·K at 450 K.[44] This result is quite close to the interfacial thermal conductance we report here for the thin MoS_2 nanosheet (7 and 8 layers). The values are also similar to those reported for different metal-insulator interfaces that lies between 30 MW/m^2·K and 110 MW/m^2·K. The results deviation presumably reflects the relatively poor nature of interface prepared by the mechanical exfoliation process. The fact that thicker samples having a higher G_k in our work indicates their better surface contact with the substrate, leading to accordingly improved interfacial energy coupling. As we discussed early, the wrinkles and/or ripples maybe introduced to the nanosheets during the mechanical exfoliation process. In addition, the thinner MoS_2 nanosheets samples may be more likely to be folded, corrugated. For example, as shown in Fig. 2.2 (f), there is folded area just at the bottom the sample. All these mechanical-folding type defects could definitely decrease the interface thermal conductance. Tang *et al.*'s MD simulation results show that the interatomic forces between the sample and substrate will decrease thousands times when the spacing or separation between these materials increases just quarter nanometers.[32] This will lead to corresponding smaller interface thermal conductance. However, the intrinsic value of the MoS_2/c-Si interfacial thermal conductance could be higher as shown in our molecular dynamics simulation discussed later in this work.

2.3.2 Effect from Sample Thickness: Interpretation from Interface Structure

To further interpret our above interfacial thermal conductance results, we perform the following Raman intensity enhancement study to reveal the interface structure. If there is a tiny spacing between MoS_2 and c-Si at the interface, the local thermal conductance will reduce significantly. At the same time, the tiny spacing will give rise of Raman intensity. So in this section we study the Raman intensity of the MoS_2 sample against its thickness, in anticipation to uncover the local interface spacing information. The multiple reflection of the incident laser beam and Raman signal within a supported film and the spacing between it and the substrate has been studied in previous work.[90,91] The net absorption factor (F_{ab}) is given by

$$F_{ab} = t_1 \frac{(1 + r_2 r_3 e^{-2i\beta_2}) e^{-i\beta_x} + (r_2 + r_3 e^{-2i\beta_2}) e^{-i(2\beta_1 - \beta_x)}}{1 + r_2 r_3 e^{-2i\beta_2} + (r_2 + r_3 e^{-2i\beta_2}) r_1 e^{-2i\beta_1}}, \tag{2.12}$$

where $t_1 = 2n_0/(n_0 + \tilde{n}_1)$, $r_1 = (n_0 - \tilde{n}_1)/(n_0 + \tilde{n}_1)$, $r_2 = (\tilde{n}_1 - \tilde{n}_2)/(\tilde{n}_1 + \tilde{n}_2)$, and $r_3 = (\tilde{n}_2 - \tilde{n}_3)/(\tilde{n}_2 + \tilde{n}_3)$ are Fresnel transmittance and reflection coefficients for the interface involving air (0), MoS_2 nanosheets (1), air (2), and Si (3). n_0, $\tilde{n}_1$, $\tilde{n}_2$ and $\tilde{n}_3$ are the refractive indices for air, MoS_2 nanosheets, air, and c-Si, respectively. $\beta_x = 2\pi x \tilde{n}_1/\lambda$, $\beta_1 = 2\pi d_1 \tilde{n}_1/\lambda$ and $\beta_2 = 2\pi d_2 \tilde{n}_2/\lambda$, where x is the depth of the point where interaction occurs, λ is the wavelength of incident laser, d_1 and d_2 are the thickness of MoS_2 nanosheets and c-Si, respectively. First, we assume there is no air between MoS_2 nanosheets and the c-Si substrate. The Raman intensity variation with the MoS_2 thickness will be compared with the experimental results to evaluate whether there is an interface spacing.

The net scattering factor (F_{sc}) is given by

$$F_{sc} = t_1' \frac{(1 + r_2 r_3 e^{-2i\beta_2}) e^{-i\beta_x} + (r_2 + r_3 e^{-2i\beta_2}) e^{-i(2\beta_1 - \beta_x)}}{1 + r_2 r_3 e^{-2i\beta_2} + (r_2 + r_3 e^{-2i\beta_2}) r_1 e^{-2i\beta_1}}, \tag{2.13}$$

where $t_1^{'} = 2\tilde{n}_1/(n_0 + \tilde{n}_1)$ and λ is the wavelength of the A_{1g} mode of MoS_2. Then the theoretical Raman intensity (F) is given as

$$F = \int_0^{d_1} \left| F_{ab} F_{sc} \right|^2 dx, \tag{2.14}$$

In the calculation, the refractive index of MoS_2 nanosheets is $5.2–1.1i$. The refractive indices of c-Si are $4.15+0.05i$ and $3.99+0.33i$ for incident laser and Raman scattering, respectively.

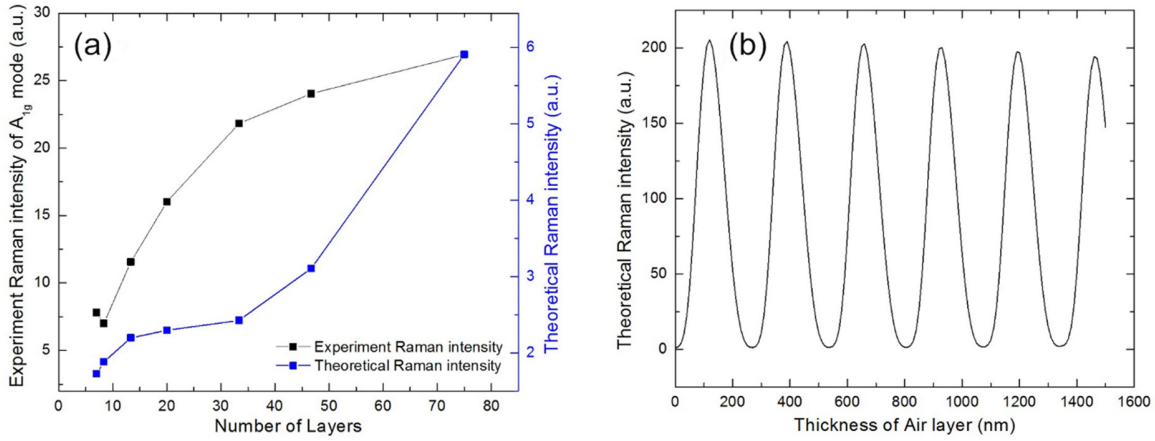

Figure 2.7 Theoretical Raman intensity study results.

Figure. 2.7 (a) shows the comparison of the experiment Raman peak intensity trend of MoS_2 A_{1g} mode and the theoretic Raman intensity F for our seven MoS_2 nanosheets samples. In the figure, we assume that there is no spacing for 75-layer MoS_2 sample for the theoretical Raman intensity calculation. The deviation of the calculation results and our experiment results uncovers the spacing existence for other six MoS_2 samples, especially for the thicker ones, 33 and 48-layer MoS_2. Compared with the theoretical calculation, Fig. 2.7 (a) shows that when the MoS_2 becomes thinner, the experimental Raman intensity is much higher than the case without interface spacing. This strongly proves the existence of spacing between MoS_2 and c-

Si. The spacing between the sample and it substrate will dramatically weaken the interatomic forces between these two materials which will lower the thermal energy coupling between the MoS_2 and c-Si system. Eventually, the spacing will result in reducing the interfacial thermal conductance. To demonstrate how the interface spacing can change the Raman intensity, we take the 75-layer (45 nm) MoS_2 as an example to calculate how much the Raman intensity will change when the spacing thickness changes. This result is shown in Fig. 2.7 (b). This possible loose contact could also result in the different temperature coefficients for different layered MoS_2 samples as shown in Fig. 2.6 (a). Additionally, with the laser heating of the sample, imperfect contact between thick MoS_2 nanosheets and c-Si interface could more likely transform into relatively well smooth contact, leading to more effectively heat transfer.

2.4 Physics Interpretation Based on Molecular Dynamics Simulations

To help better interpret the experimental results, molecular dynamics (MD) simulations are conducted to study the MoS_2/c-Si interfacial thermal conductance. The inset of Fig. 2.8 (a) shows the physical domain construction for a MoS_2 nanosheet sample placed above a silicon bulk. There are nine layers of MoS_2 and it measures $17.7 \times 3.8 \times 5.2$ nm^3. The silicon bulk measures $22.3 \times 5.8 \times 5.3$ nm^3. Varshney *et al.*[92] have studied the force field of MoS_2 systematically. Following their work, we create an orthorhombic unit cell based on the original non-orthorhombic structure of MoS_2. This transformation does not change any modeling dynamics for its constituent atomic entities.[92]

The set 8 of the force field parameter in the work of Varshney *et al.* [92] is used in this simulation. The bond interaction of Mo and S is described by the Morse interaction. The angle component of the force field is described by harmonic style. The non-bonded component of the force field is described by the Lennard-Jones (12-6) potential. The partial electrostatic

charge of Mo is 0.76 and of S is –0.38 in the unit of one electron charge. Standard Ewald summation is employed to take care of the long-range Coulombic interaction. Table 2.2 shows the details of the force filed parameters for MoS_2. All simulations here were performed using LAMMPS molecular dynamics package from Sandia National Laboratories.[93]

Since the interaction between the MoS_2 and c-Si is weak, the van der Waals force and Lennard-Jones (12-6) potential are employed to describe the interaction. Similar method has been used for interface interaction of other materials.[36,94-96] According to the universal force field,[97] the parameters of the Lennard-Jones potential are: $\sigma_{S-Si} = 3.71\,\text{Å}$, $\sigma_{Mo-Si} = 3.27\,\text{Å}$, $\varepsilon_{S-Si} = 0.0143$ eV, $\varepsilon_{Mo-Si} = 0.0065\,\text{eV}$. The initial distance of MoS_2 and c-Si is set to be 3.54 Å. Periodic boundary condition is applied to the *x* and *y* (in-plane) directions and free boundary condition for the *z* (out-of-plane) direction. The conjugate gradient method is used for the initial minimization. The distance between MoS_2 and c-Si is 2.5 Å at equilibrium. Afterwards, MoS_2 is irradiated by a short thermal pulse of $q = 3.6 \times 10^{-3}$ W for 50 fs.

Table 2.2 The force field parameters of MoS_2 in the MD simulation.

Parameters	**Potential**	**Coefficients**
Bond (Mo-S)	Morse interaction	$D_0 = 19.945$, $\alpha = 0.858$, $r_0 = 2.39$
Angle(Mo-S-Mo)	Harmonic style	$K = 2.5163$, $\theta_0 = 82$
Angle(S-Mo-S)	Harmonic style	$K = 2.5163$, $\theta_0 = 82$
Non-bonded (Mo-Mo)	Lennard-Jones (12-6)	$\varepsilon = 0.8382$, $\sigma = 2.551$
Non-bonded (S-S)	Lennard-Jones (12-6)	$\varepsilon = 0.0606$, $\sigma = 3.3695$
Non-bonded (Mo-S)	Lennard-Jones (12-6)	$\varepsilon = 0.0339$, $\sigma = 2.9318$

Equation for Morse interaction: $E = D_0\left[e^{-2\alpha(r-r_0)} - 2e^{-\alpha(r-r_0)}\right]$,

Equation for Harmonic interaction: $E = K(\theta - \theta_0)^2$,

Equation for Lennard-Jones (12-6): $E = 4\varepsilon\left[(\sigma/r)^{12} - (\sigma/r)^6\right]$.

Because of the thermal pulse, the temperature of MoS_2 has an abrupt increase in the beginning. Then heat would be transported from MoS_2 nanosheets to c-Si. The temperature of MoS_2 decreases while the temperature of c-Si increases.

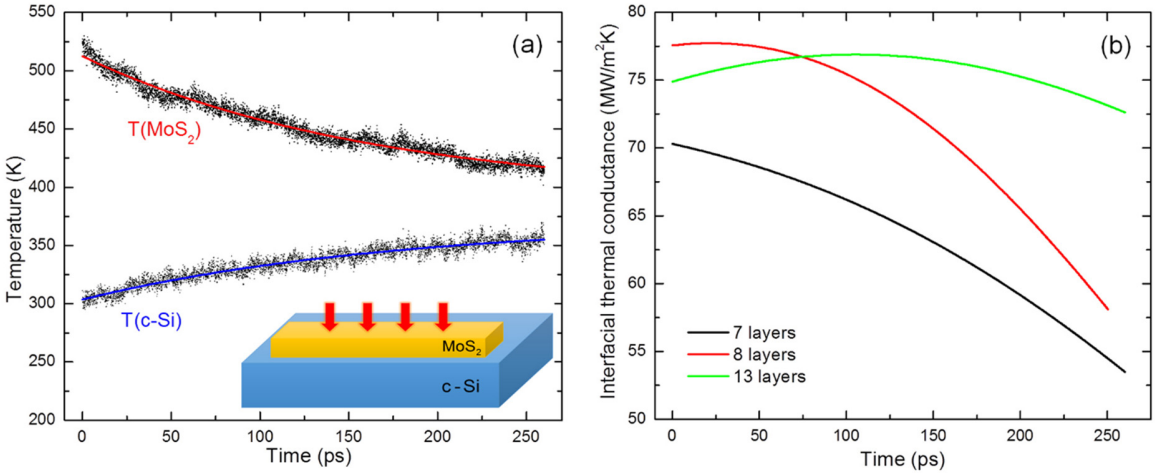

Figure 2.8 Molecular Dynamics simulation results.

Fig. 2.8 (a) shows the temperature evolution of MoS_2 and c-Si for a 7-layered MoS_2 sheet. To precisely determine the interface thermal conductance, the top 4 layers of c-Si bulk are chosen for the temperature calculation, and the bottom 2 layers of MoS_2 are used for its temperature calculation. The interfacial thermal conductance is calculated as

$$G = -\frac{n \times C_p \times \partial T/\partial t}{\left[T\big|_{MoS_2} - T\big|_{Si}\right] \times A}, \tag{2.15}$$

where $\partial T/\partial t$ is the temperature changing rate of MoS_2. $T\big|_{MoS_2}$ is the bottom temperature of MoS_2, and $T\big|_{Si}$ is the surface temperature of c-Si. A is the contact area of MoS_2 and c-Si. n is the number of mole and C_p is heat capacity of the MoS_2 nanosheet. In our calculation, the average temperature of MoS_2 is first fitted with an exponential function first, then $\partial T/\partial t$ is

calculated based on the fitted exponential function. For $T\big|_{MoS_2}$ and $T\big|_{Si}$, instead of using the raw data in Eq. 2.15, we first fit them using an exponential function, as shown in Fig. 2.8 (a), and then use the fitted data for interface thermal conductance calculation. All these treatments are intended to reduce the statistical noise in the MD raw data.

Figure 2.8 (b) shows the interfacial thermal conductance determined from Eq. 2.15. The calculated *G* changes during thermal relaxation due to change of the energy coupling of the interface. The interface thermal conductance is roughly proportional to the interface materials phonon specific heat and the phonon transmission.[98] During thermal relaxation, although the c-Si surface temperature increases a little bit, MoS_2 bottom temperature reduces more. Therefore, the interface material phonon specific heat goes down, leading to decreased *G*. More detailed explanation about the temperature effect on interface thermal conductance can be found in our recent work.[98] The thermal conductance is different for these three different cases. Generally speaking, we can conclude that when the material is thicker, the interface thermal conductance is higher. This trend agrees well with our experimental observation. In our MD simulation, we have tried thinner MoS_2 nanosheets, but found they are vulnerable to tiny stress in the material, and intend to warp. Therefore, the increased mechanical stiffness of thicker samples will help form a better contact with the c-Si substrate, leading to increased interface thermal conductance. Based on the results shown in Fig. 2.8 (b), we could get the interfacial thermal conductance around 56.6, 62.0, and 74.1 $MW/m^2 \cdot K$ for 7L, 8L, and 13L respectively. These are higher than the experiment result (Table 2.1) of respectively layered MoS_2. This reveals the imperfect contact of MoS_2 and c-Si in our experiments samples. The upper bound of our experimentally measured *G* is 68.6±9.14 $MW/m^2 \cdot K$, very close to the MD simulation result.

CHAPTER 3. HOT CARRIER EFFECT ON INTERFACE THERMAL TRANSPORT OF MOS2 NANOSHEETS

In this chapter, we develop a novel approach for non-contact simultaneous determination of hot carrier diffusivity (D) and interface thermal resistance (R) of sub-10 nm mechanically exfoliated MoS_2 nanosheets on c-Si. The effect of hot carrier diffusion in heat conduction by photon excitation, diffusion, and recombination is identified by varying the heating spot size from 0.294 μm to 1.14 μm (radius) and probing the local temperature rise using Raman spectroscopy. The hot carrier diffusion length (L_D) can be determined without knowledge of the hot carrier's life time. Unlike previous methods by making electrical contacts and applying an electric field for D measurement, our technique has the advantage of being truly non-contact and non-invasive, and is able to characterize the electron diffusion behavior of virgin 2D materials. Also it points out that hot carrier diffusion needs to be taken into serious consideration in Raman-based thermal properties characterization of 2D materials, especially under very tightly focused laser heating whose spot size is comparable to the hot carrier diffusion length. This chapter begins with the characterization of samples in Section 3.1. In Section 3.2, physical principle and experiment details are introduced. The measurement results of both R and D are reported in Section 3.3, followed by structure and physics analysis discussion.

3.1 Sample Preparation and Characterization

Same to Chapter 2, we prepare the four sub-10 nm thick multilayered MoS_2 samples by micromechanical cleavage from their parent bulk MoS_2 crystals. In this work, the lateral size of layered MoS_2 nanosheets ranges from 4 to 12 μm. We use optical microscope, atomic

force microscope (AFM) (Model MMAFM-2, Digital Instruments, CA, USA) and Raman spectroscopy to identify and locate the MoS_2 nanosheets.

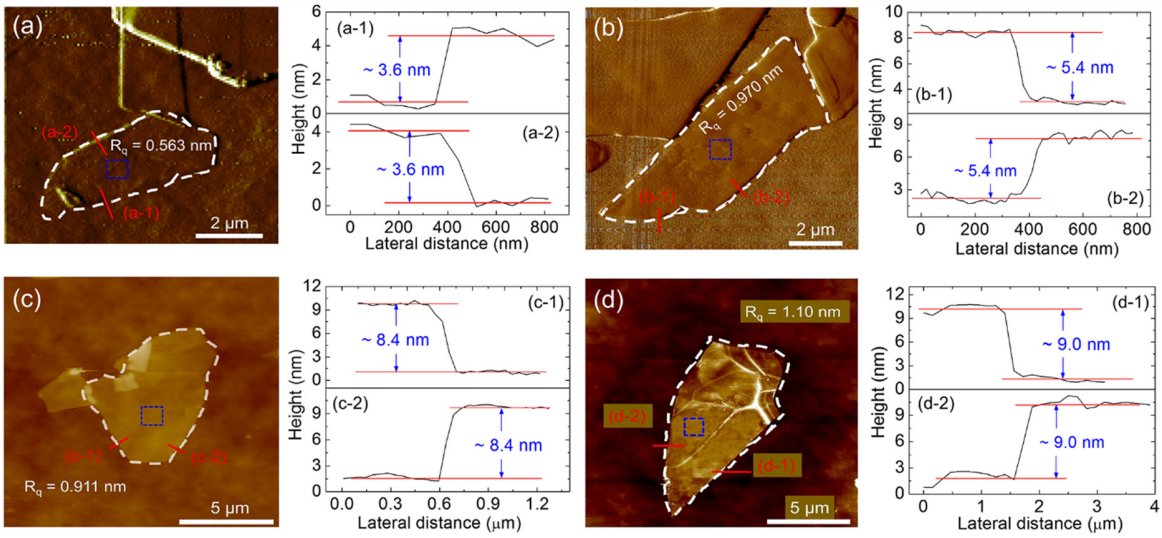

Figure 3.1 AFM measurement results of four MoS_2 samples.

Figure 3.1 shows AFM scan images of the four studied MoS_2 samples on the c-Si substrate. The samples have a thickness of 3.6 nm, 5.4 nm, 8.4 nm, and 9.0 nm, respectively. In Fig. 3.1, for each sample, the sample area is marked by the dashed white curves. Two red lines indicate the edges for height measurements and the measurement results are shown in the right two figures for each sample. The blue box in each sample AFM image shows the area where the laser is focused during Raman experiment. The sample surface roughness is evaluated as well. The 3.6 nm thick sample has a root-mean-square (RMS) roughness (R_q) of 0.563 nm. As the thickness increases, RMS roughness increases: R_q value for the 5.4 nm, 8.4 nm, and 9.0 nm thick sample is 0.970 nm, 0.911 nm, and 1.10 nm, respectively. This is probably due to possible wrinkles or ripples in the samples. Also, the substrate (c-Si) has a R_q of 0.09 nm, confirming its atomically smooth surface.

3.2 Physical Principle and Experimental Details

3.2.1 Physical Principle

The schematic in Fig. 3.2 (a) shows the physical principles of our non-contact technique. Here we use a CW 532 nm (E=2.33 eV) laser to excite the MoS_2/c-Si structure. Because the excitation energy E is greater than the bandgap of MoS_2 (E_g=1.29~1.80 eV) and c-Si (E_g=1.15 eV), the electrons (e) are excited by the absorbed photons to the conduction band, leaving holes (h) in the valence band. Part of the photon energy $\Delta E = (E - E_g)$ of hot carriers is quickly dissipated to other electrons and the lattice by a fast non-radiative process. This occurs very quickly (about 10^{-12} s) so that we can neglect carrier diffusion effects during this process. The rest part of photon energy (E_g) is carried by electrons. They will store this photon energy and diffuse out of the excitation spot before recombining with holes, leading to a significantly wider thermal source spatial redistribution as a result of diffusion. Due to the Coulomb attraction, the excited electrons and holes move together as *e-h* pairs in this diffusion process. The time of this diffusion process are typically nanoseconds and diffusion cannot be neglected.[99] Since both the multilayered MoS_2 and c-Si have an indirect bandgap, the radiative recombination of carriers is greatly restricted by crystal momentum conservation. Therefore, the excited hot electrons would release the laser energy via non-radiative recombination with holes by exciting phonons. The energy of these phonons in MoS_2 dissipates within the 2D nanosheets and through layers down to substrate to raise the temperature, eventually reaching thermal equilibrium with the electrons.

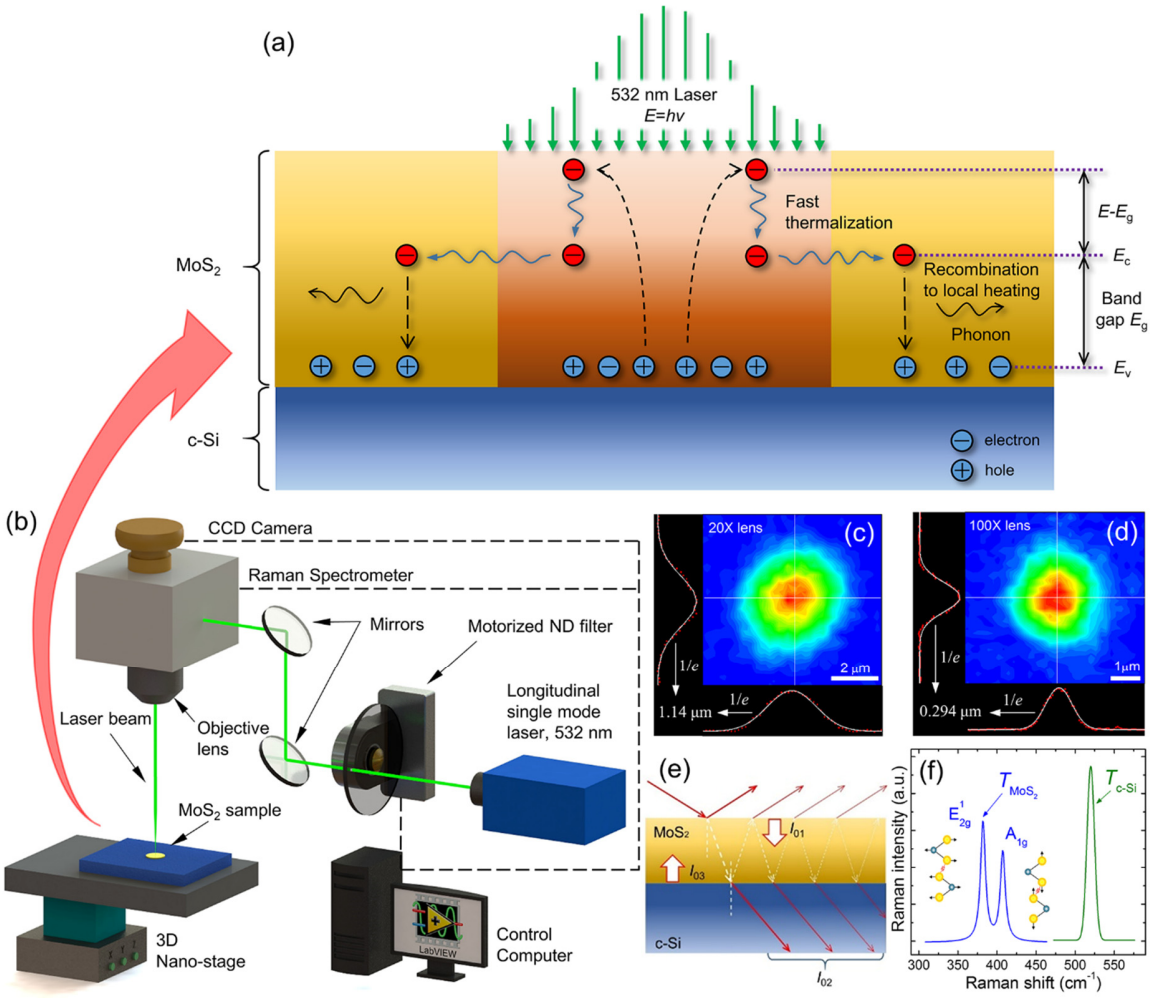

Figure 3.2 Schematic of MoS_2 under a CW 532 nm laser illumination (not to scale). The physical model of hot carrier generation, diffusion, and recombination. The Raman experiment setup.

The schematic in Fig. 3.2 (a) shows the physical principles of our non-contact technique. Here we use a CW 532 nm (E=2.33 eV) laser to excite the MoS_2/c-Si structure. Because the excitation energy E is greater than the bandgap of MoS_2 (E_g=1.29~1.80 eV) and c-Si (E_g=1.15 eV), the electrons (e) are excited by the absorbed photons to the conduction band, leaving holes (h) in the valence band. Part of the photon energy $\Delta E = (E - E_g)$ of hot

carriers is quickly dissipated to other electrons and the lattice by a fast non-radiative process. This occurs very quickly (about 10^{-12} s) so that we can neglect carrier diffusion effects during this process. The rest part of photon energy (E_g) is carried by electrons. They will store this photon energy and diffuse out of the excitation spot before recombining with holes, leading to a significantly wider thermal source spatial redistribution as a result of diffusion. Due to the Coulomb attraction, the excited electrons and holes move together as *e-h* pairs in this diffusion process. The time of this diffusion process are typically nanoseconds and diffusion cannot be neglected.[99] Since both the multilayered MoS_2 and c-Si have an indirect bandgap, the radiative recombination of carriers is greatly restricted by crystal momentum conservation. Therefore, the excited hot electrons would release the laser energy via non-radiative recombination with holes by exciting phonons. The energy of these phonons in MoS_2 dissipates within the film and through layers down to substrate to raise the temperature, eventually reaching thermal equilibrium with the electrons. The generation and diffusion of heat and hot carriers in the sample are governed by two partial differential equations in steady state ($\partial N / \partial t = 0$).[100,101] The first one is the carrier diffusion equation to determine the hot carrier concentration $\Delta N(\boldsymbol{r},t)$ (cm^{-3}):

$$D\nabla^2 \Delta N - \frac{\Delta N}{\tau} + \frac{\partial n_0}{\partial T}\frac{\Delta T}{\tau} + \Phi\alpha = 0, \tag{3.1}$$

where D_E (cm^2/s), τ (s) and Φ (photons/cm^3s) are the carrier diffusivity, the electron-hole recombination time of MoS_2 and the incident photon flux of the laser source. α is the optical absorption coefficient of the MoS_2 nanosheets. n_0 (cm^{-3}) is the equilibrium free-carrier density at temperature T. The first term on the left side is about the carrier diffusion, the second term: $\Delta N/\tau$ represents the electron-hole recombination. The thermal activation term $(\partial n_0 / \partial T)\Delta T / \tau$

is related to the carrier creation due to the temperature rise. It is negligible under the relatively low-temperature rise and in small free-carrier density case.[100,102] In our experiment, for the 3.6 nm thick sample, the temperature rise under 20× objective is only 1.0 K per mW (temperature rise for other samples under different lenses are summarized in Table 3). Besides, the free carrier density at equilibrium could be given as $n_0 = N_s \exp(-E_g / 2k_B T)$, where N_s is the number per unit volume of effectively available states. It is of order 10^{19} cm^{-3} at room temperature and increases with temperature. k_B is the Boltzmann's constant. E_g is the bandgap energy. k_B is the Boltzmann's constant. At room temperature, $k_B T$ = 0.026 eV. Since E_g=1.3 eV, so $k_B T \ll E_g$ gives a very small n_0 (room temperature) to neglect the thermal activation term. The last term $\Phi\alpha$ is the carrier photogeneration source term. In our work, the MoS_2 film is very thin (sub-10 nm) compared with its lateral dimension (4 ~ 12 μm), so the hot carrier gradient in the thickness direction is neglected. Therefore, Eq. 3.1 only considers the in-plane direction diffusion.

The second equation is the thermal diffusion equation that involves the free carrier density since non-radiative recombination is a heat source:

$$k\nabla^2 \Delta T + (h\nu - E_g)\Phi\alpha + \frac{E_g \Delta N}{\tau} = 0, \tag{3.2}$$

where $\Delta T(\boldsymbol{r},t)$ (K), k (W/mK) and E_g (eV) are the temperature rise, the thermal conductivity and the bandgap energy of the multilayered MoS_2. And $h\nu$ (eV) is the photon energy of the laser source. The second term of equation (17), $(h\nu - E_g)\Phi\alpha$, which is proportional to $h\nu$–E_g, represents the heat generation due to photo-generated carriers giving off the excess energy to the MoS_2 lattice. The term $E_g \Delta N / \tau$ contains the carrier concentration represents the heat generation through the non-radiative recombination of free carriers.

The hot electrons will diffuse in the sample until they recombine with holes through the non-radiative transition. Therefore, the real heating area will not be simply the laser irradiating area. Instead, it will be strongly affected by the hot carrier diffusion length ($L_D = \sqrt{\tau D}$) of the electrons. When the laser heating spot size (radius: 0.294 μm to 1.14 μm) is comparable to the carrier diffusion length and the laser heating spot size is relatively small, this effect becomes more prominent. If the laser heating spot size is sufficiently large, the hot carrier diffusion will have less or negligible effect on the heating area. For multilayered MoS_2, the hot carrier diffusion length is in the order of 0.1 μm.[12,103] So we could observe different heating phenomena in MoS_2 by changing the laser heating spot size. However, the c-Si used in this experiment is single-side polished silicon wafer [*p*-doped, (100)-oriented, 0-100 Ω·cm resistivity, ~335 μm thickness] from University Wafer Company (Boston, MA). The diffusion length of this *p*-type Si is around 700 μm [104] which is much larger than our laser heating spot size. Generally, the bulk and surface recombination mechanisms coexist. Nevertheless, we only consider the bulk recombination process here. The physics can be explained as below. First, consider the c-Si surface area of the MoS_2/c-Si interface, MoS_2 could be thought of as native *n*-doping due to its sulfur vacancies.[105] So the MoS_2/c-Si structure is just one *p*-*n* junction, and the depletion region of that has been found to considerably reduce the surface recombination rate.[106] Then, for the remained c-Si surface, its native oxide layer could be the predominant passivating layer which can also significantly reduce the surface recombination rate.[106] So we could neglect the effect of the carriers surface recombination for the diffusion process. In this case, the transmitted laser energy only heats the c-Si substrate by the fast thermalization process ($\Delta E = E - E_g\big|_{\text{c-Si}}$) because the hot carriers with the rest photon energy ($E_g\big|_{\text{c-Si}}$) will diffuse such a long distance that will induce a uniform heating of the overall Si

substrate. As a result, the measured temperature rise of MoS_2 (by Raman spectrum) is determined by the hot carrier diffusion and the MoS_2/c-Si interface thermal resistance. Eqs. 3.1 and 3.2 are solved to analyze the experimental results and determine the hot electron diffusivity and the interface thermal resistance/conductance. In our work, the temperature difference between MoS_2 and Si is determined and used. This treatment has taken into full consideration of the temperature rise effect of the c-Si substrate.

3.2.2 Experiment Details

Raman experiments are conducted by using the Confocal Raman system that consists of a Raman spectrometer (Voyage^{TM}, B&W Tek, Inc.) and a microscope (Olympus BX53). We use a CW laser of 532 nm as shown in Fig. 3.2 (b). The laser is introduced to the Raman system and its power is adjusted by a motorized neutral-density (ND) filter system (CONEX-NSR1 and NSND-5, Newport Corporation). The laser beam is focused on a specific area of the samples (detailed in Fig. 3.1) and the laser power is varied to introduce different heating levels in the MoS_2 samples. The optically generated heat is dissipated away across the MoS_2/c-Si interface to the substrate. During the experiments, both the Raman spectrometer and the motorized ND filter are controlled by LabVIEW-based software on a computer. The Raman spectrometer could collect and store the spectra for each energy level automatically after the ND filter is set. This significantly shortens the experiment time, reduces the external disturbance, and improves the precision and accuracy of the experiment. We use the Raman spectrometer to measure the temperature rise of MoS_2 and c-Si. Based on the temperature rise and the absorbed laser power, we can directly determine the hot carrier diffusivity and interfacial thermal resistance.

Shown in Fig. 3.2 (c) and (d) are the laser energy distribution contour under 20× and 100× objective of focused laser spot images from CCD camera. The beam size at the focal plane is measured where there is enough irradiance to have a decent signal to noise ratio without saturating the camera, and the beam lineout is fitted with a Gaussian function [the white curves in Fig. 3.2 (c) and (d)] for both *x* and *y* directions to take the average as final results. For the CCD camera, the pixel size under 20×, 50×, and 100× lens is 0.347, 0.123, 0.069 μm/pixel, respectively. Then the Gaussian beam spot size r_0 (at e^{-1} peak value) under 20×, 50×, and 100× lens is 1.14±0.01, 0.531±0.006, and 0.294±0.003 μm, respectively. When the laser beam irradiates the sample surface, multiple reflections happen within the MoS_2 film. According to the Transfer Matrix Method (TMM)[107] and the complex refractive index of two materials,[68] we could determine the transmitted power at the top surface (I_{01}), the transmitted power in c-Si top surface (I_{02}) and the reflected power at the bottom surface (I_{03}) of MoS_2. Here the complex refractive index of MoS_2 is assumed to be constant because it has been found to have little change with sample's thickness for our samples thickness range.[15]

3.3 Results and Discussion

3.3.1 Steady Thermal Response of MoS_2 under Different Laser Heating Sizes

In our experiments, for all the four samples, eight room-temperature Raman spectra are collected at the laser power (*P*) spanning from 2.49 to 11.9 mW (corresponding to the average power density $P/\pi r_0^2$ is from 0.942 to 4.50 MW/cm^2) under 100× objective and from 6.83 to 32.8 mW (0.167 to 8.03 MW/cm^2) under 20× objective. Note this laser power is the level just before the laser enters the MoS_2 sample. This heating power variation is designed to study the Raman spectrum change under optical heating, and this could significantly suppress the experiment noise of a single laser power experiment. To avoid damage to the sample and to

stay within the linear temperature-dependence range for Raman properties, we try to keep the excitation laser power as low as possible. Five representative room temperature Raman spectra under 100× objective lens and their corresponding Lorentzian fits collected from the 3.6 nm thick MoS_2 sample are shown in Fig. 3.3 (a), where both E^1_{2g} and A_{1g} modes shift to left (red-shift) linearly with increased laser power and the peak position shifts are visible as $\Delta\omega|(2.49\text{ mW} \sim 11.9\text{ mW})$. We use two objective lenses to generate different optical heating phenomena. Fig. 3.3 (c) and (d) show the Raman shift for the two vibration modes as a function of incident laser power under 20× and 100× objective lens, respectively. Similarly, as described in Section 2.3.1, we obtain the first-order laser power coefficient for two vibration modes of MoS_2 and c-Si. For this 3.6 nm thick sample, the fitted χ_P for E^1_{2g} and A_{1g} modes are quite close, –(0.151±0.004) cm^{-1}/mW and –(0.151±0.003) cm^{-1}/mW under 100× objective, and –(0.029±6.0×10^{-4}) cm^{-1}/mW and –(0.027±7.0×10^{-4}) cm^{-1}/mW under 20× objective, respectively. Note the laser power coefficients for two vibration modes under 100× objective are higher than those under 20× objective. This is because the temperature rise determined by Raman spectra under 100× increases more rapidly than that under 20× due to the larger power density under 100× objective. The fitted χ_P of c-Si for this 3.6 nm thick MoS_2 sample are –(0.008±3.0×10^{-3}) cm^{-1}/mW [Fig. 3.3 (e)] and –(0.151±4×10^{-3}) cm^{-1}/mW [Fig. 3.3 (f)] under 20× and 100× objectives, respectively.

The temperature calibration experiment is conducted for MoS_2 and c-Si to determine the local temperature rise during the above experiment. Fig. 3.3 (b) shows five representative Raman spectra and their corresponding Lorentzian fits with the temperature ranging from 297 to 398 K under 50× objective lens. The power of the incident laser power is maintained low enough to not increase much temperature rise at the irradiated spot (1.10 mW before entering

the sample). The Raman shift of both E^1_{2g} and A_{1g} modes decreases with increased temperature is visible as $\Delta\omega|(297\ \text{K} \sim 398\ \text{K})$. The temperature dependence of both E^1_{2g} and A_{1g} modes of MoS_2 and c-Si measured between 297 and 398 K is depicted in Fig. 3.3 (b). The Raman shift for both E^1_{2g} and A_{1g} modes decreases with increased global temperature for all cases and exhibits linear temperature dependence in the range used in our experiment.

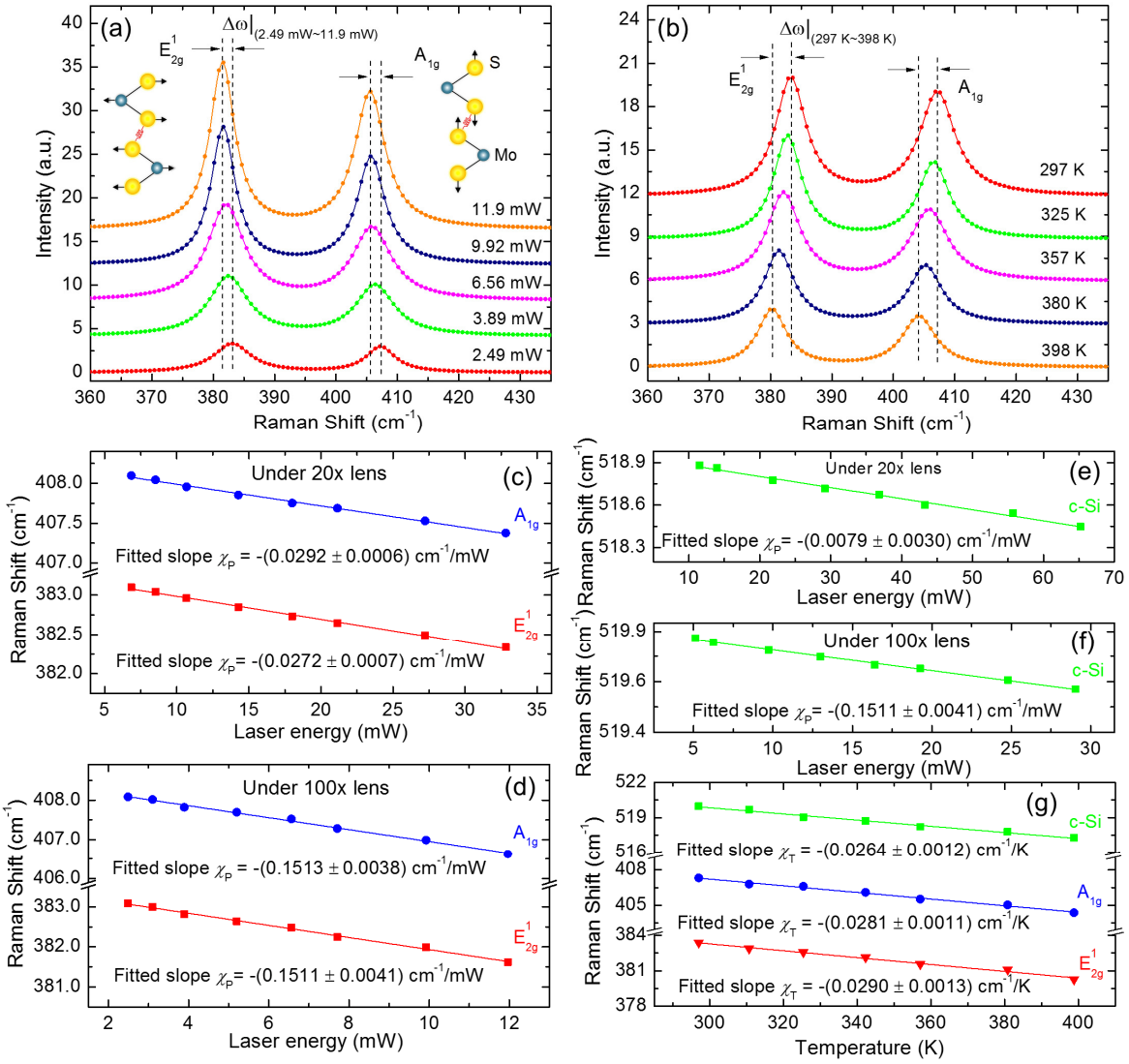

Figure 3.3 The Lorentzian-fit Raman spectra and linear fitting of Raman shift against laser energy and temperature of 3.6 nm thick MoS_2.

For the 3.6 nm thick MoS_2 sample, as shown in Fig. 3.3 (g), the extracted the first-order temperature coefficient χ_T values are –(0.029±1×10^{-3}) cm^{-1}/K and –(0.028±1×10^{-3}) cm^{-1}/K for E^1_{2g} and A_{1g} modes, and –(0.026±1×10^{-3}) cm^{-1}/K for the c-Si substrate. The temperature coefficients of all four samples are summarized in Table 3.1. The temperature-dependent changes in the Raman spectra are due to the anharmonic terms in the lattice potential energy, mediated by phonon-phonon interactions.[108]

We note that (for the 3.6 nm MoS_2 sample) the χ_T value from E^1_{2g} mode (–0.029 cm^{-1}/K) is slightly (3%) larger than that from A_{1g} mode (–0.028 cm^{-1}/K). The difference in χ_T value between those two modes gets larger for the other three samples (e.g. χ_T value from E^1_{2g} mode is ~14% larger than that from A_{1g} mode for 9.0 nm sample). It makes sense that the out-of-plane A_{1g} mode shows a weaker temperature response for all these four multilayer MoS_2 samples, where there are interlayer interactions restricting the vibrations away from the basal plane. And this restriction increases with increased layer number. The in-plane E^1_{2g} mode will be less affected by the interlayer interactions and weakly affected by the substrate,[87] so we use the Raman results from this vibration mode as the property to evaluate the interface thermal resistance and the hot carrier diffusivity.

In our experiment, the MoS_2/c-Si samples are firmly placed on a 3D nano-stage and the same point of each sample (as marked in Fig. 3.1 with dashed blue box) is measured during the entire experiments. This treatment could eliminate any possible location-to-location structure variation and temperature coefficient variation. For each MoS_2 sample, the average temperature rise per unit laser power ($\Delta\overline{T}_{20\times}$ and $\Delta\overline{T}_{100\times}$) could be experimentally obtained by

$\Delta\overline{T}_{MoS_2 \text{ or c-Si}} = \chi_p \chi_T^{-1}$ (K/mW). And this value for four MoS_2 samples is summarized in Table 3.1. The use of $\Delta\overline{T}$ instead of direct temperature rise ΔT (K) for the determination of D and R is to avoid artificial shifts of peak position resulting from calibration errors of two different objectives. Generally, a higher $\Delta\overline{T}_{MoS_2}$ is induced for a thicker sample because a thicker sample sample comes with a higher absorbance level. This will result a higher temperature rise in MoS_2 to transfer the heat across the interface down to the substrate. However, from the Table 3, the temperature rise of the 9 nm MoS_2 (6.42 K at 100×) is lower than that of 8.4 nm MoS_2 (9.96 K at 100×). This is caused by lower interface thermal resistance (R) of 9.0 nm MoS_2 sample: R for 9.0 nm and 8.4 nm MoS_2 sample is 4.46×10^{-8} and 7.66×10^{-8} K·m^2/W, respectively (from Table 3.1). So there will be more heat going into the substrate from MoS_2 film for 9.0 nm sample. For the 3.6 nm thick MoS_2 sample, the highest temperature rise of MoS_2 film and c-Si we have heated to is around 33 K and 10 K under 20× objective, respectively, and around 62 K and 5.6 K under 100× objective, respectively.

The heat transfer across the MoS_2/c-Si structure could be described by $\Delta q = A(T_{MoS_2} - T_{Si})/R$ (A is the heating area, Δq is the net heat flow). So the temperature difference between MoS_2 film and c-Si should be proportional to the inverse of the heating spot area. However, our results show it is significantly different from this prediction, indicating the hot carrier diffusion effect. Taking the 3.6 nm MoS_2 as an example, under 20× objective, the measured temperature difference per mW laser heating is 0.71 K. Under 100× objective, the laser heating spot size is 6.6% of that under 20×. As a result, we expect the temperature rise difference is around 10.7 K under 100× objective. But our measurement only gives a temperature rise difference of 4.74 K per mW under 100× objective. This strongly indicates

that the hot carriers diffuse out of the heating region, make the effective heating spot size bigger than the laser spot, and reduce the temperature difference.

Table 3.1 Summary of Raman experiment results of four MoS_2 samples.

Sample thickness:			**3.6 nm**	**5.4 nm**	**8.4 nm**	**9.0 nm**
$\chi_{P(20\times)}$ (cm^{-1}/mW)	MoS_2	E^1_{2g}	-(0.029±0.001)	-(0.024±0.001)	-(0.030±0.009)	-(0.030±0.001)
		A_{1g}	-(0.027±0.001)	-(0.025±0.001)	-(0.025±0.002)	-(0.032±0.001)
	c-Si		-(0.008±0.0003)	-(0.007±0.0002)	-(0.011±0.0004)	-(0.010±0.0003)
$\chi_{P(100\times)}$ (cm^{-1}/mW)	MoS_2	E^1_{2g}	-(0.151±0.004)	-(0.142±0.006)	-(0.163±0.007)	-(0.154±0.004)
		A_{1g}	-(0.151±0.004)	-(0.163±0.009)	-(0.163±0.009)	-(0.152±0.005)
	c-Si		-(0.012±0.0003)	-(0.016±0.0005)	-(0.026±0.001)	-(0.013±0.001)
$\chi_{T(50\times)}$ (cm^{-1}/K)	E^1_{2g}		-(0.029±0.001)	-(0.020±0.001)	-(0.016±0.001)	-(0.024±0.001)
	A_{1g}		-(0.028±0.001)	-(0.018±0.001)	-(0.014±0.001)	-(0.021±0.001)
$\Delta\overline{T}_{MoS_2}$ (K/mW)	20×		-(1.00±0.05)	-(1.16±0.08)	-(1.85±0.10)	-(1.26±0.06)
	100×		-(5.21±0.26)	-(6.86±0.49)	-(9.96±0.62)	-(6.42±0.27)
$\Delta\overline{T}=$ $\Delta\overline{T}_{MoS_2}-\Delta\overline{T}_{c\text{-}Si}$ (K/mW)	20×		-(0.71±0.05)	-(0.89±0.06)	-(1.41±0.07)	-(0.89±0.04)
	100×		-(4.74±0.24)	-(6.27±0.45)	-(8.94±0.55)	-(5.92±0.25)

3.3.2 Determination of Hot Carrier Diffusivity

Then we conduct a 3D numerical modeling based on the finite volume method to calculate the temperature rise to determine the hot carrier diffusivity (*D*) and the interface thermal resistance (*R*). As shown in Figure 3.4, the model calculation size of the substrate has a radius and thickness of 50 μm. The MoS_2 sample is with the actual size and thickness as those in the experiment. The smallest mesh size along the thickness direction is 0.1 nm and increases from the MoS_2 surface to the substrate with an increasing ratio of 1.02. The smallest mesh size is 1 nm in the radial direction and also increases with a ratio of 1.02. In our modeling, in the in-plane and cross-plane directions, we take $k_{\parallel}=52$ W/mK (ref. 65) and $k_{\perp}=2$ W/mK,

(ref. [72]) $k_{c\text{-}Si}$=148 W/mK. (ref. [109]) P=1 mW is the excitation laser energy before entering the sample.

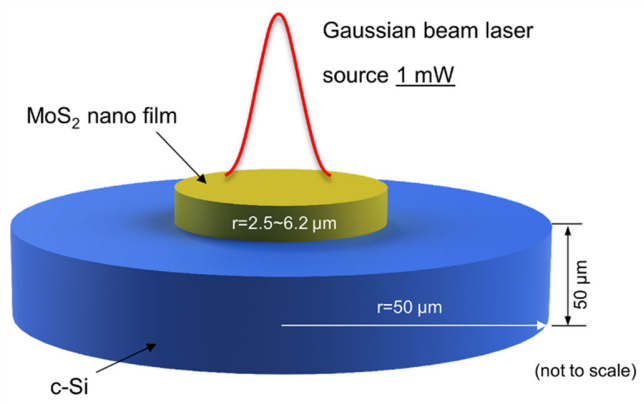

Figure 3.4 3D numerical modeling setup.

The thickness dependent bandgap of MoS_2 thin film has been investigated,[15] and we fit the E_g values for different thickness samples by an exponential function as $E_g(\text{eV}) = 0.5836 \times \exp(-\text{thickness}/3.525) + 1.29$ as shown in inset of Fig. 3.6 (c). Then we extract E_g values for our samples as 1.48 eV for 3.6 nm, 1.41 eV for 5.4 nm, 1.34 eV for both 8.4 nm, and 1.33 eV for 9.0 nm thick sample. This treatment could help us determine R and D values with better confidence instead of using a constant E_g value. τ is set as 1 ns at room temperature.[99] For MoS_2, it has been documented that the photo-excited electrons have a life time of hundreds of picoseconds in few-layer samples and nanoseconds or longer in the thick crystal.[99,110] Besides, for phonon contribution to the thermal transport, the material thermal conductivity could be reduced if the heating size is smaller than the long mean free path phonons.[111,112] In this work, for MoS_2, the phonon mean free path is less than 20 nm[62,113] which is much smaller than the laser spot size (radius: 0.294 to 1.15 μm). So the ballistic effect on thermal conductivity is not influential. In this 3D modeling, we only consider the diffusive

phonon transport. We first solve the carrier diffusion equation (Eq. 3.1) and then the heat conduction one with the hot carrier concentration $\Delta N(\boldsymbol{r},t)$ used in the source term.

Here we take the 3.6 nm thick MoS_2 sample for example to discuss the modeling results. In our modeling, we scan the combined space of diffusivity D and interface thermal resistance R to calculate the temperature difference between MoS_2 and c-Si under 20× and 100× objective laser heating. The (D, R) pair giving the temperature difference both agreeing with the 20× and 100× experimental results is taken as the real properties of the sample. Note in our Raman experiment, as expressed in Eq. 2.2, the measured temperature rise of both MoS_2 and c-Si are Raman-intensity weighted average temperature of the sample. At a location of the sample, the local Raman intensity is proportional to the local laser intensity and the scattered Raman signal multi-reflected in the sample. All these have been considered in our modeling to evaluate the temperature rise of both MoS_2 and c-Si substrate.

In Fig. 3.5 (a) and (b), we present the calculated averaged temperature difference under two different objective lenses: $\Delta\overline{T}_{20\times}$ and $\Delta\overline{T}_{100\times}$ in the (D, R) space for the 3.6 nm thick MoS_2 nanosheet. In both cases, the lower electron diffusivity or higher interface thermal resistance implies a higher temperature rise. When D is lower, the heating area will be limited to the laser heating region, resulting in a higher local temperature rise and difference. When R is higher, less heat will dissipate from MoS_2 to c-Si substrate under the same temperature drop. This will require a higher local temperature rise to dissipate the heat to the substrate. Additionally, in Fig. 3.5 (a) (under 20× objective), it is evident that the temperature difference is less sensitive to the D change, especially for the lower values of R. However, when the laser spot size reduces (under 100× lens), the sensitivity of $\Delta\overline{T}_{100\times}$ on D changes increases. The physics can be explained as below. The hot carrier diffusion length is $L_D = \sqrt{\tau D} = 0.344\ \mu\text{m}$ (based on our

measured *D* for this sample, and detailed later). This is around 1.5 times the laser spot size under 100× lens (r_0=0.294 μm). So the hot carriers could diffuse out of the laser spot size more easily and their effect becomes more prominent.

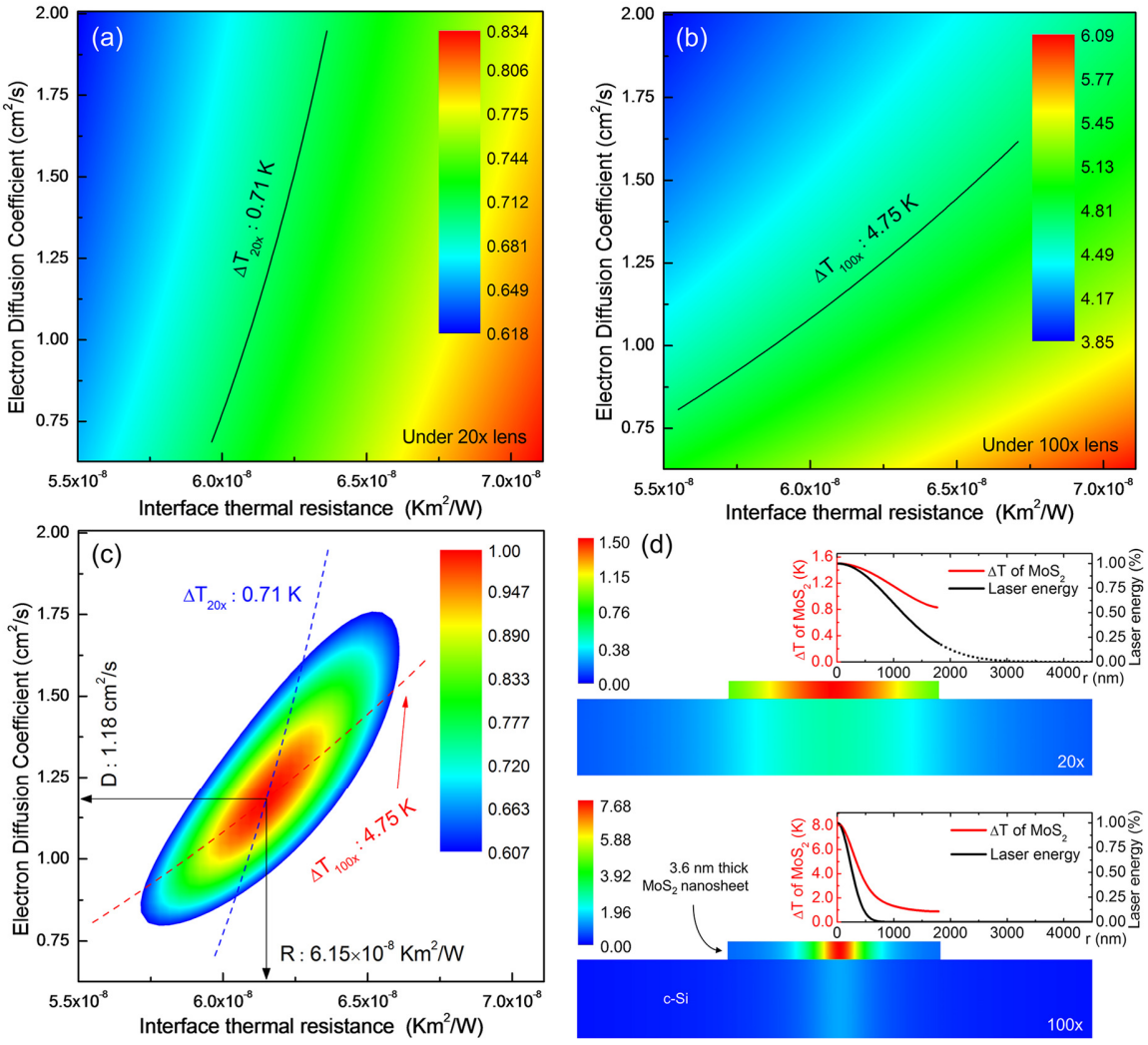

Figure 3.5 3D numerical modeling results for 3.6 nm thick sample to illustrate the results.

In Fig. 3.5 (a) and (b), for each heating spot size, the experimentally obtained temperature difference (the isolines) could be satisfied by many different (*D, R*) pairs. So we could not determine final results based on a single case. To determine *D* and *R*, we combine

the results from both cases as shown in Fig. 3.5 (c). For the sample of 3.6 nm thick MoS_2, by the cross point of the red ($\Delta\overline{T}_{100\times}$) and blue ($\Delta\overline{T}_{20\times}$) dashed curves, we could determine that D is 1.18 cm^2/s and R is 6.15×10^{-8} Km^2/W. To better present the uncertainty of D and R, we calculate the normalized probability distribution function (Ψ) as $\Psi = \exp\left[-(x-\overline{x})^2/(2\sigma^2)\right]$, where x, $\overline{x}$, and σ are the variable, its average, and the standard deviation. In the (D, R) space, we have $\Psi_{(D,R)} = \Psi_{\Delta\overline{T}_{100\times}} \cdot \Psi_{\Delta\overline{T}_{20\times}}$. We use the value of $\Psi_{(D,R)} = 0.6065$ corresponding to the σ confidence in the (D, R) space to show the final results uncertainty. Finally, the deduced R is $6.15^{+0.25}_{-0.25}\times10^{-8}$ $K\cdot m^2/W$ and D is $1.18^{+0.30}_{-0.23}$ cm^2/s. The uncertainty of these two values is determined by $\Psi_{(D,R)}$ distribution as shown in Fig. 3.5 (c). For example, to determine the uncertainty of D, let $\Psi_{(D,9.26\times10^{-8})} = 0.6065$ in the $\Psi_{(D,R)}$ distribution and fix the R value, we could get D_{min}=0.950 cm^2/s and D_{max}=1.48 cm^2/s. Final results and the uncertainty for the other three samples are summarized in Table 3.2 and also plotted in Fig. 13.

Table 3.2 The summary of the calculated hot electron diffusivity (D) and the interface thermal resistance (R) from the 3D numerical modeling and data fitting, and the corresponding electron mobility (μ) and electron diffusion length (L_D).

Sample Thickness	R (10^{-8} $K\cdot m^2/W$)	D (cm^2/s)	μ ($cm^2/V\cdot s$)	L_D (μm)
3.6 nm	$6.15^{+0.25}_{-0.25}$	$1.18^{+0.30}_{-0.23}$	$47.4^{+11.9}_{-9.38}$	$0.344^{+0.041}_{-0.036}$
5.4 nm	$6.27^{+0.38}_{-0.38}$	$1.07^{+0.37}_{-0.26}$	$42.7^{+14.7}_{-10.5}$	$0.327^{+0.052}_{-0.043}$
8.4 nm	$7.66^{+0.37}_{-0.36}$	$1.20^{+0.34}_{-0.27}$	$47.9^{+13.5}_{-10.8}$	$0.346^{+0.046}_{-0.042}$
9.0 nm	$4.42^{+0.17}_{-0.17}$	$1.62^{+0.30}_{-0.23}$	$64.8^{+12.2}_{-9.36}$	$0.402^{+0.036}_{-0.030}$

Figure 3.5(d) shows the calculated temperature rise distribution in the 3.6 nm MoS_2 sample on c-Si substrate under laser heating with 20× and 100× objective lenses by the determined D and R. For both cases, the temperature rise is uniform in the thickness direction

in MoS_2 because the sample is very thin. Also the heat conduction/transfer along the thickness direction in MoS_2 is much larger than that in the in-plane direction. Besides, the temperature rise of c-Si is very small because of its high thermal conductivity. For the 3.6 nm thick MoS_2 sample, from the Raman experiment ($\Delta\overline{T} = \chi_p \chi_T^{-1}$), the temperature rise is much smaller than that of MoS_2 as we discussed in the temperature calibration experiment section. So it can easily conduct the heat away from the heating region. Compared to the laser energy distribution, the temperature distribution is out of the laser spot a lot, especially for the case under the 100× objective. As discussed above, the diffusion length L_D is only 1/3 of the laser spot size under the 20× and around 1.5 times of that under the 100× objective. This makes the hot carrier diffusion have a significant contribution to our observations under the 100× objective.

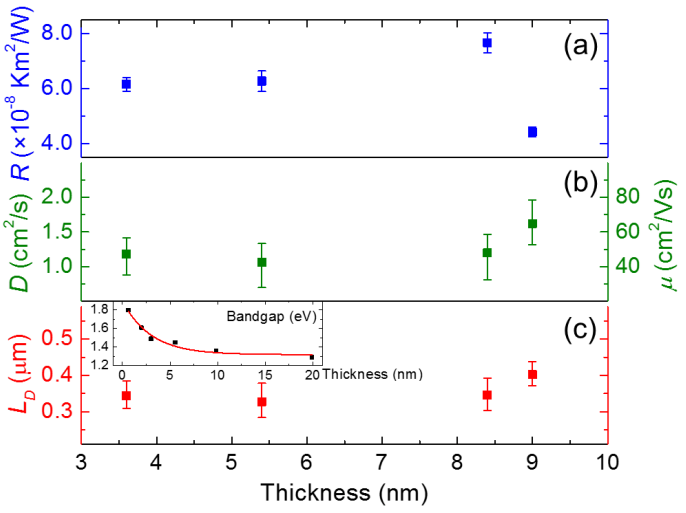

Figure 3.6 Interface thermal resistance, hot electron diffusivity, corresponding electron mobility, and the electron diffusion length of four MoS_2 samples as a function of thickness.

As discussed above, during the diffusion process, electrons (*e*) and holes (*h*) move as pairs due to the Coulomb attraction between them. Therefore, the measured *D* is the ambipolar diffusivity, $D = 2D_eD_h/(D_e + D_h)$, where $D_{e(h)}$ is the unipolar diffusivity of electrons

(holes).[114] In our optical study, equal numbers of electrons and holes are generated. Besides, the effective masses of electrons and holes of MoS_2 are comparable and even similar.[115] Therefore, the diffusivity for both D_e and D_h are expected to be the same. As a result, the measured value *D* can be approximately treated as unipolar carrier diffusivity of both electrons and holes. In this thermalized system, the diffusivity is related to the mobility (μ) by the Einstein relation, $D / k_B T = \mu / q,$ where k_B, *T*, and *q* are the Boltzmann constant, temperature, and the amount of charge of each carrier. For the 3.6 nm thick MoS_2 nanosheets sample, the measured *D* corresponds to a mobility of $\mu =$ 47.4 cm^2/Vs. Here, we assume that the carriers have a thermal distribution of 300 K during the diffusion process because the energy relaxation time is only several picoseconds.[99] Our measured μ is very close to the literature value of 30-60 cm^2/Vs for multilayer MoS_2 on SiO_2,[53] ~70 cm^2/Vs for multilayer MoS_2 on Al_2O_3.[116]

The interface thermal resistance we obtain here is in the order of 6×10^{-8} Km^2/W as summarized in Table 3.2. They are lower than what we found in previous work, such as the 7.8 nm MoS_2 on c-Si with *R* is 1.66×10^{-7} Km^2/W.[68] We attribute this mainly to the fact that the samples we prepare here have better interface contact due to our experience development in sample preparation. Tang *et al*. found that the loose (imperfect) contact at the interface could dramatically reduce the interface thermal energy coupling.[32]

3.3.3 Discussion

As reported before, one approach that could simultaneously extract the thermal conductivity and interface thermal resistance of supported 2D layered material has been developed by exploiting the property of the laser beam.[117] However, that method cannot explain the results we observed in this work because they did not consider the hot carrier diffusion phenomena. To have non-contact detection, the pump-probe technique has also been

applied to study charge carriers in MoS_2 [103] and graphene nanosheets.[51] The biggest difference between the optical and electric measurement of carrier mobility is that we do not need to cover the sample (MoS_2 nanosheets) with a dielectric layer such as HfO_2.[12] The dielectric layer is believed to affect the mobility because of the suppression of Coulomb scattering by the dielectric.[118,119] Nevertheless, our optically measured mobility is still comparable to those with a dielectric top layer. As described above, during the diffusion process, the electron-hole pair moves as a unit so that the pair is electrically neutral. In this case, the pair will not be influenced by the Coulomb scattering.[103]

In our data processing by solving Eqs. 3.1 and 3.2, τ takes 1 ns. The finally determined D is dependent on the τ. To further elucidate this effect, we use a normalized carrier concentration $\xi=\Delta N/\tau$ to re-express those equations as (neglecting the thermal activation term):

$$D\tau\nabla^2\xi - \xi + \Phi\alpha = 0, \tag{3.3}$$

$$k\nabla^2\Delta T + (h\nu - E_g)\Phi\alpha + E_g\xi = 0. \tag{3.4}$$

From the above equation, it is clear the term $D\tau$ can be determined without the input of other hot carrier properties. The carrier diffusivity D is determined based on the carrier lifetime τ. However, the interface thermal resistance R has no dependence on the carrier lifetime knowledge. The lifetime diffusion length of the hot carriers is calculated from D and τ as $L_D = \sqrt{\tau D}$. As summarized in Table 3.2, for the four samples (3.6 nm, 5.4 nm, 8.4 nm, and 9.0 nm thickness), their L_D are determined as 0.344 μm, 0.327 μm, 0.346 μm, and 0.402 μm, respectively. It is conclusive that the technology developed in this work can firmly determine the lifetime diffusion length of the hot carriers. Their diffusivity is dependent on the lifetime data, which needs to be obtained from a separate experiment. A recently published work found that the photo-carriers in the C-exciton state are hot carriers with free-carrier properties which

could also transport energy.[120] Under our 532 nm (2.33 eV) laser excitation, the high energy C-exciton (transition optical bandgap of C-excitonic transition for few-layered MoS_2 is 2.70 eV [121]) could also be generated by the up-conversion process but with relatively lower possibility than using a 400 nm (3.10 eV) laser. This effect of C-excitons is actually already included in our experiment model because C-excitons will also contribute to the local temperature rise and energy transfer that is probed by Raman spectroscopy to identify effect of the hot carrier diffusion in our work.

As shown in Table 3.2 and Fig. 3.6, the *R* and *D* are with a relatively high uncertainty, especially for *D*. This is mainly caused by the uncertainty from the linearly fitting of χ_p and χ_T. Additionally, the little thickness-dependent hot carrier diffusivity we find here may be attributed to the stronger effect of Coulomb scattering or weaker in-plane electron-phonon interaction for thicker samples.[122] As for the sample, we do not reduce the thickness of MoS_2 nanosheets to single layer due to sample preparation difficulty. Under optical microscope, the single-layered MoS_2 has very weak visibility on c-Si substrate compared to that on SiO_2 substrate. This makes it extremely difficult to identify them for Raman study. Besides, for single-layered MoS_2, its larger bandgap (~1.8 eV) could potentially reduce electron mobility[123] and it is very sensitive to air exposure which is so far believed to make it have a lower mobility.[124] Both experiment and analytic modeling have shown that multilayered MoS_2 devices could have a higher mobility and density of states under the same dielectric environment. Also, they have a higher current limit and better manufacturability compared with single layer devices.[125]

CHAPTER 4. ET-RAMAN TECHNIQUE FOR PROBING INTERFACE THERMAL TRANSPORT AND HOT CARRIER DIFFUSION OF MOS2

In widely applied Raman characterization of 2D atomic layer material interface thermal resistance (R), laser absorption in the 2D atomic layer and its temperature rise are needed. These factors cause the largest experimental uncertainty due to unknown optical properties variation from sample to sample; interface spacing-induced optical interference, off-normal direction laser incidence, and very large thermal-Raman calibration uncertainties. In this chapter, we report a novel energy transport state resolved Raman (ET-Raman) to address these critical issues. In ET-Raman, under steady laser heating, by constructing two steady heat conduction states with different laser spot sizes, we differentiate the effect of R and hot carrier diffusivity (D). By constructing an extreme state of zero/negligible heat conduction using a picosecond laser, we differentiate the effect of R and material's specific heat. Combining the steady state Raman and pico-second Raman, we precisely determine R and D without need of laser absorption and temperature rise of the 2D atomic layer. Seven mechanically exfoliated MoS_2 samples (6.6 nm to 17.4 nm) on c-Si are characterized using ET-Raman. Their hot carrier diffusivity is measured in the order of 1.0 cm^2/s, and having an increasing trend against the MoS_2 thickness. R is determined as $1.22\sim1.87\times10^{-7}$ $K\cdot m^2/W$, decreasing with the MoS_2 thickness. This chapter begins with brief characterization of samples in Section 4.1. Then, in Section 4.2, we will focus on the physical model of ET-Raman. The measurement results of both R and D are reported in Section 4.3, followed by structure and physics analysis discussion.

4.1 Sample Preparation and Characterization

4.1.1 FL MoS_2 Nanosheets Preparation and AFM Measurement Results

We prepare seven few-layered MoS_2 samples by micromechanical cleavage technique. The lateral size of layered MoS_2 nanosheets has an equivalent radius ranging from 2.5 to 6.2 μm. This limited sample size is also considered in our numerical modeling for data processing.

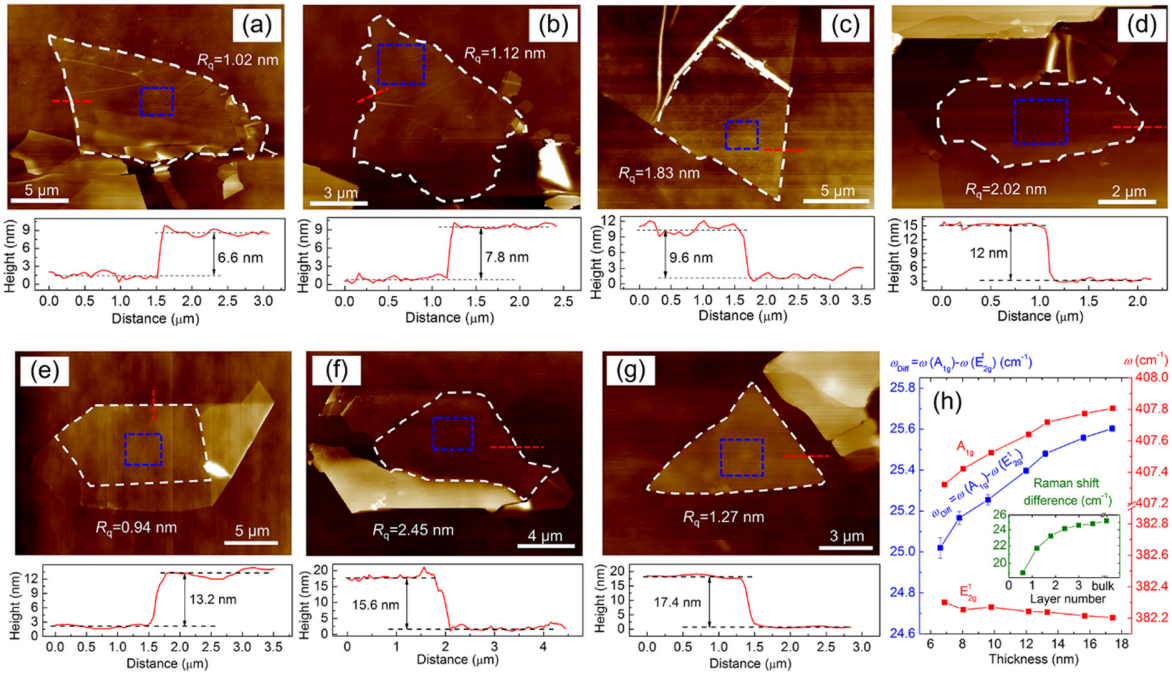

Figure 4.1 AFM measurement results of seven MoS_2 samples supported on c-Si.

Figure 4.1 (a)-(g) show AFM images of seven MoS_2 samples supported on c-Si substrate. In each image, the sample area is marked by the dashed white circle. The height profiles shown below the images correspond to the red dashed lines in the AFM images. The samples have a thickness of around 6.6 nm, 7.8 nm, 9.6 nm, 12.0 nm, 13.2 nm, 15.6 nm and 17.4 nm, respectively. The blue dashed square in each sample AFM image shows the area where the laser is focused during different Raman experiments. We also evaluate the sample surface roughness. For example, the 6.6 nm thick sample has a root-mean-square (RMS)

roughness (R_q) of 1.02 nm. R_q increases a little bit with increased thickness except for 13.2 nm and 17.4 nm thick sample. These two samples may have fewer wrinkles or ripples. In addition, the substrate (c-Si) has a R_q of 0.09 nm which confirms its atomically smooth surface. Fig. 4.1(h) displays the thickness dependence of Raman shift and Raman shift difference $[\omega_{Diff} = \omega(A_{1g}) - \omega(E^1_{2g})]$ of two Raman modes of MoS_2 nanosheets which was widely used to study the thickness of FL MoS_2 as discussed in Section 2.3.1.[86] Our results agree well with results and predictions of Lee *et al*.'s work.[86]

4.1.2 MoS_2 Nanosheets Raman Shift Mapping Results

We also perform scanning Raman of 6.6 nm and 13.2 nm thick MoS_2 samples to have a better idea of the uniformity of surface structure. Here we take the 6.6 nm thick MoS_2 sample for example to discuss the scanning results. Fig. 4.2 (a) shows its AFM image. The blue dashed square marks the area in which the scanning Raman is performed. The square has a width of 20 μm. Full Raman spectra are recorded for each point with a step size of 500 nm. The spectra are analyzed by an MATLAB-based automatic fitting program, which determines the Raman shift, intensity, and linewidth for two vibration modes of MoS_2 and LO phonon mode of c-Si.

We further process the extracted data to create false color images as depicted in Fig. 4.2 (a-1) and (a-2). Here we set Raman shift information of the bare c-Si substrate as white to increase the contrast between sample and substrate. In these figures, we plot the Raman shift of E^1_{2g} and A_{1g} modes as a function of position. Fig. 4.2 (a-3) shows the Raman shift difference of these two modes. Fig. 4.2 (a-4) shows the Raman shift difference from a smaller area as marked with green dashed square in Fig. 4.2 (a). This area is also included in the area where we performed the Raman experiments for *D* and *R* determination. The scanning step

size for this area is 100 nm. The relatively uniform Raman shift difference mapping shows the sample thickness is uniform and there is no large interface spacing variance.

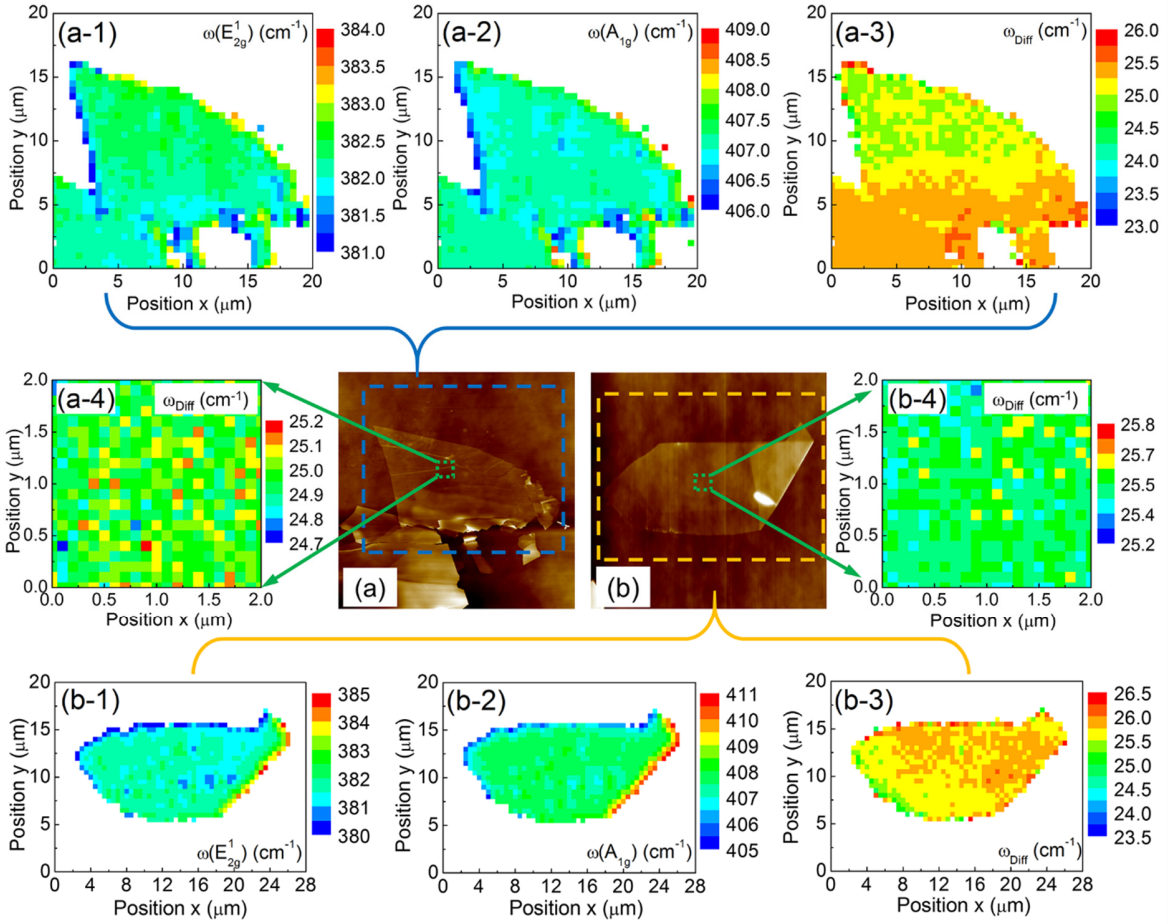

Figure 4.2 False color images of Raman shift map of 6.6 nm and 13.2 nm thick MoS_2 samples.

4.2 Physical Model and Experimental Details of ET-Raman Technique

4.2.1 Physical Principles of ET-Raman Technique

As described in Chapter 3, besides two laser-heating states by CW laser, we will use a picosecond laser in the ET-Raman technique. We construct three distinct energy transport states in both space and time domains, and probe the materials' thermal response. Fig. 4.3 (a) shows the physical principles of this technique. A 532 nm laser irradiates the MoS_2 sample for both laser heating and Raman probe. Because the excitation energy E is greater than the

bandgap of MoS_2, the absorbed photons will excite the electrons (e) to the conduction band with holes (h) left in the valence band. This results in the formation of hot electrons and holes (hot carriers). Then the hot carriers will lose part of the photon energy $\Delta E=(E-E_g)$ via a rapid non-radiative process on a time scale of 0.1 ps.[110] The hot electrons will store the rest part of photon energy (E_g) and diffuse out of the excitation spot before recombining with holes. This diffusion will result in a significantly wider thermal source spatial redistribution in the sample. It typically takes nanoseconds for this diffusion process so we have to consider the diffusion effect.[99] At last, the excited hot electrons would release the laser energy via non-radiative recombination with holes by exciting phonons. The energy of these phonons in MoS_2 nanosheets dissipates within the sample and through the interface down to the substrate to raise the local temperature. The phonons eventually reach thermal equilibrium with the electrons.

The first energy transport state in our technique is the steady state heating, and it has two sub-states with different laser heating sizes. As shown in Fig. 4.3 (c) and (d), we use a CW laser source to generate steady-state heating to study the temperature profile that depends on (R, D) effect. Moreover, by using different objectives (20× and 100×) to have the size variation, we could differentiate the effect of D and R. In Fig. 4.3 (c), the laser heating spot under a 20× (NA=0.4) objective has a diameter around 2.30 μm (1/e peak value). Since the MoS_2 nanosheets will absorb the laser energy, they will conduct the absorbed energy directly to substrate via R and to the in-plane direction then to the substrate via the interface (effects of both R and D). At the same time of laser heating, the same laser beam also excites Raman signal by which we could collect to get the temperature profile of the sample. By using different laser powers (P), we can obtain one parameter, called Raman shift power coefficient (RSC): $\chi_{CW1}=\partial\omega/\partial P$. As expected, χ_{CW1} is determined by R, D, laser absorption coefficient, and

temperature coefficient of Raman shift. Then, as shown in Fig. 4.3 (d), we reduce the laser heating dimension to a much smaller level by a 100× (NA=0.8) objective (0.588 μm), and we also obtain RSC from this experiment as χ_{CW2}. At this steady state, the D of the 2D material will have more influence on the measured temperature than that under 20× objective. Therefore, these two steady states construction could differentiate the effect of D and R in the measured RSC by Raman spectroscopy. Note although we mention temperature here as they are reflected in RSC, we do not need to determine the absolute temperature rise in the whole technique.

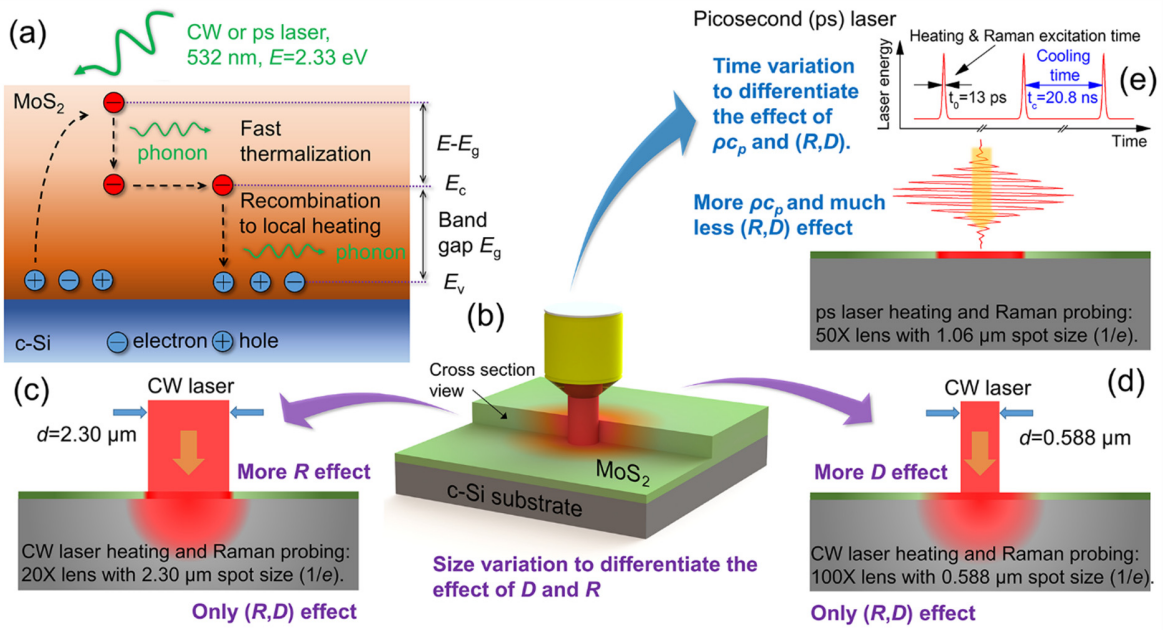

Figure 4.3 Physical model of hot carrier generation, diffusion, and recombination in MoS_2 under laser illumination (not to scale).

The second energy transport state is completely opposite to the steady-state: it has zero-transport. In this experiment, we apply a ps laser (repetition rate is 48.2 MHz, the pulse duration is 13 ps) under 50× (NA=0.5) objective with r_0 as 0.531 μm (1/e peak value) with the same

wavelength as the CW laser to focus on the sample to do localized heating and Raman experiment. Using the same wavelength for the two laser sources ensures that the samples have the same laser absorption level in two heating states. In the same way, we obtain the RSC for this ps laser heating case: $\chi_{ps}=\partial\omega/\partial P$. The collected Raman signal reflects the Raman signal-weighted temperature rise during ps laser heating. Within this very short heating time (13 ps), the thermal diffusion length (L_t) for MoS_2 and c-Si is only around 38 nm and 68 nm, respectively. ($L_t = 2\sqrt{\alpha_k t_c}$, α_k=2.75×10^{-5} m^2/s for MoS_2 and 8.92×10^{-5} m^2/s for Si, is the in-plane thermal diffusivity; t_0=13 ps, is the ps laser pulse width). They are much smaller than the laser spot size (r_0=0.53 μm). Therefore, we could neglect the heat conduction from the heating region. Besides, the thermal relaxation time of the MoS_2 nanosheets for our interface structure (R is in the order of 10^{-7} K·m^2/W) is estimated to be around 1.9 ns (=$\delta z \cdot \rho c_p R$. δz takes 10 nm, is the thickness of MoS_2 nanosheets; ρc_p=1.89 MJ/m^{3}K, is the volumetric heat capacity, R takes 10^{-7} K·m^2/W, is the interface thermal resistance.) which is much longer than the heating time (13 ps) and much shorter than the laser cooling time (20.8 ns). Therefore, during ps laser heating, the energy absorbed in MoS_2 is used to heat up the sample, but is not transferred out of the heating region to other MoS_2 region or the substrate. Also the sample will be fully cooled to the ambient temperature during the pulse interval. This ensures the RSC measured during ps laser heating has no DC accumulation effect from previous pulses. In summary, the RSC (χ_{ps}) is mainly coming from the volumetric heat capacity of the sample (ρc_p). D and R have an extremely limited contribution to the temperature rise so that we could use this heating state to distinguish the roles of ρc_p and (R, D).

While evaluating the above different states, we do not consider the heat loss to the environment during the Raman measurement in atmospheric condition. This is because, as has

been studied for the supported 2D material, the heat loss through radiation or natural convection is negligible compared to the interfacial heat flux.[41] In our steady-state experiment, also as described in Eq. 2.2, the measured RSC is proportional to the temperature rise of the two materials, which is a Raman/laser intensity weighted average over the laser spot size as

$$\overline{T}_{\mathrm{CW}} = \int_0^{V_0} I_a(\boldsymbol{r})T(\boldsymbol{r})dv \Big/ \int_0^{V_0} I_a(\boldsymbol{r})dv\,. \tag{4.1}$$

For the zero-transport state, the measured temperature rise includes both time and space averaged over the pulse width and heating domain as

$$\overline{T}_{\mathrm{ps}} = \int_0^{t_0}\int_0^{V_0} I_a(\boldsymbol{r},t)T(\boldsymbol{r},t)dv \Big/ \int_0^{t_0}\int_0^{V_0} I_a(\boldsymbol{r},t)dv\,. \tag{4.2}$$

All of these will be also considered in the following 3D numerical simulation for data processing.

After these three energy transport states experiments, we will define the dimensionless normalized RSC as: $\Theta_1 = \chi_{\mathrm{CW1}}/\chi_{\mathrm{ps}}$ and $\Theta_2 = \chi_{\mathrm{CW2}}/\chi_{\mathrm{ps}}$. Although χ_{CW1}, χ_{CW2}, and χ_{ps} are all influenced by the Raman temperature coefficient and the laser absorption in the sample, this normalized RSC completely rules out the effect of laser absorption and Raman temperature coefficients. Θ_1 and Θ_2 are only a function of the 2D and substrate materials' ρc_p, R, and D. Using a 3D heat conduction model to include all these properties, we could finally determine D and R of the 2D material. The whole measurement does not involve absorbed laser heating power determination and absolute temperature rise determination. This eliminates the large uncertainties brought in by these two key factors in the past measurements.

4.2.2 Governing Equations for Data Processing

As given in Chapter 3, for the steady-state heating, the generation and diffusion of heat and electrical carriers in the sample are governed by two partial differential equations in steady

state as Eqs. 3.1 and 3.2. The hot electrons will diffuse in the sample until they recombine with holes to release the energy through the non-radiative recombination transition. Therefore, we could observe different heating phenomena in MoS_2 by changing the laser heating spot size.

When we use the ps laser to generate the zero-transport heating state, the laser pulse is so short that only the fast thermalization process happens and we could neglect the heat conduction in the lattice here as discussed above. By only considering the laser absorption in MoS_2 sample and its substrate, we have

$$\rho c_{\mathrm{p}} \frac{\partial \Delta T_{\mathrm{ps}}}{\partial t} = \alpha I(\frac{hv - E_g}{hv}), \tag{4.3}$$

where I (W/cm^2) is the laser intensity, t is the time. $\Delta T_{\mathrm{ps}}(\mathrm{r},t)$ is the temperature rise from the zero-transport state. After considering both space and time domain Gaussian distributions, and the Beer-Lambert law, the laser intensity (heat flux) is given by:

$$I(r,z,t) = \frac{I_0}{\tau_L} \exp\left[-\frac{r^2}{r_0^2}\right] \exp\left[-\ln(2)\frac{t^2}{t_0^2}\right] \exp\left[-\frac{z}{\tau_L}\right], \tag{4.4}$$

where I_0 (W/cm^2) is the peak laser intensity, r_0 (0.53 μm) is the laser spot radius of ps laser, t_0 (6.5 ps) is the half pulse width. $\tau_{\mathrm{L}} = \lambda/4\pi k_{\mathrm{L}}$ is the laser absorption depth. From Chapter 2.2.3, we have $\tau_{\mathrm{L}}(MoS_2)$=38.5 nm, and τ_{L}(c-Si)=820 nm. Because the thickness of MoS_2 nanosheets (6.6 nm to 17.4 nm) is smaller than its laser absorption depth, both MoS_2 and c-Si will absorb the laser energy and be heated.

As a result, the measured temperature rise of MoS_2 is actually determined by the hot carrier diffusivity and the interface thermal resistance under steady-state heating and only by laser absorption rate and ρc_{p} under zero-transport state heating. By solving Eqs. 3.1, 3.2, 4.1,

and 4.2, we could rule out the laser absorption term and deduce the ratio of the temperature rise ($\overline{T}_{\mathrm{CW}}/\overline{T}_{\mathrm{ps}}$) of two materials from two heating states. The ratio is just the normalized RSC. Then we solve Eqs. 3.1 and 3.2 to analyze the experimental results and determine the *R* and *D* value. In our work, the temperature difference between MoS_2 and c-Si is determined and used. This treatment has taken into full consideration of the temperature rise effect of the c-Si substrate.

4.2.3 ET-Raman Experiment Details

Figure 4.4 shows the schematic of the Raman experiment setup. We perform the Raman experiments by using the same confocal Raman system as shown in Fig. 3.2 (b). The 532 nm CW laser or ps laser is introduced to the Raman system and the laser power is adjusted by a motorized ND filter system. The laser source could be switched by the flip mounted mirror before it enters the Raman system without changes in the experiment setup. Except for searching for and identifying the MoS_2 sample under the microscope, the 3D piezo-actuated nano-stage is also used in the following Raman shift scanning experiment and it provides us accurate step size. The laser beam is focused on a specific area of the samples (as shown in Fig.4.1).

During the experiments, we use LabVIEW-based software to fully control the Raman spectrometer, the motorized ND filter, and 3D nano-stage. The Raman spectrometer could automatically acquire and store the spectrum for each energy level after the ND filter is set or each position after the 3D nano-stage is set during the scanning Raman experiment. By analyzing the Raman spectrum, we could evaluate the RSC of MoS_2 and c-Si. Based on the RSC under different heating states, we can directly determine the hot carrier diffusivity and interfacial thermal resistance. Fig. 4.4 (b) is the structure of our MoS_2 supported on the c-Si

substrate. Fig. 4.4 (c) shows the atomic structure of the typical layered MoS_2. The Mo atom is in the middle for each layer and the layer distance is around 0.65 nm.

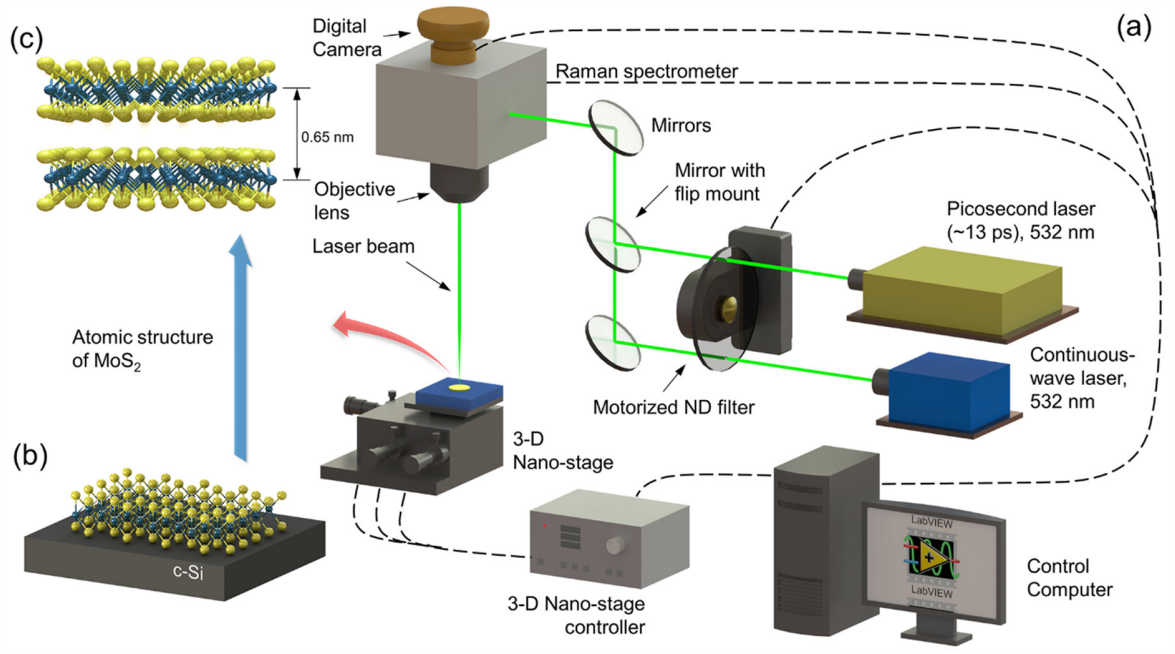

Figure 4.4 Schematic of the experimental setup for the ET-Raman experiment of MoS_2/c-Si sample.

4.3 Results and Discussion

4.3.1 Thermal Response of MoS_2 under ps and CW Laser Heating

In the Raman experiments, for all the seven samples, eight room-temperature Raman spectra are automatically collected at different laser power by the controlled computer to find the laser power coefficient. The CW laser energy is from 1.59 mW to 6.34 mW (0.586 to 2.33 MW/cm^2) under the 100× objective and from 6.03 to 29.2 mW (0.145 to 0.703 MW/cm^2) under the 20× objective. The ps laser energy is from 1.84 to 6.93 mW (pulse power density is from 0.08 to 0.31 GW/cm^2) under the 50× objective. Note that this laser power is the level just before the laser enters the MoS_2 sample surface. Moreover, the power is maintained as low as possible

especially for the ps laser to avoid photon absorption saturation [126,127] and stay within the linear temperature dependence range for Raman properties. For the 532 nm picoseconds pulse laser heating, the saturation intensity is around 1.13 GW/cm^2.[127] When the photon density exceeds that level, the conductance band will be filled and the material will be unable to absorb further photons according to the Pauli-exclusion principles.[128]

Here we also take the 6.6 nm thick sample for example to illustrate the results. Five representative room temperature Raman spectra and their corresponding Lorentzian fits of MoS_2 and Gaussian fits of c-Si under 100× objective by CW laser are shown in Fig. 4.5 (a) and under 50× objective by ps laser are shown in Fig. 4.5 (b). Also in Fig. 4.5 (a), the inset shows the false color map for the spatial energy distribution of the laser energy beam under 100× objective. The mapping data is from the image captured by a CCD camera. The corresponding laser spot size (at e^{-1}) on the sample is determined as 0.294 μm. In Fig. 4.5 (a), both two modes of MoS_2 and LO phonon mode c-Si shift to left (red shift) linearly with increased laser power, and the peak position shifts are visible as $\Delta\omega|(1.59\text{ mW} \sim 6.34\text{ mW})$ by CW laser and $\Delta\omega|(1.84\text{ mW} \sim 4.68\text{ mW})$ by ps laser for MoS_2. The temperature rise of c-Si is not very visible due to its larger thermal conductivity, so the Raman shift changes little. The Raman shift changes indicate that the local temperature of the sample becomes higher under a higher laser power.

Two objective lenses with CW laser are used to generate different optical heating phenomena. In this work, we choose the Raman results from this E^1_{2g} vibration mode to deduce deduce RSC because the in-plane E^1_{2g} mode will be less affected by the interlayer interactions and weakly affected by the substrate.[87] Besides, the E^1_{2g} mode exhibits slightly polar dependence on the laser polarization configuration. So the effects of switching laser sources

on Raman results will be eliminated. By CW laser, as shown in Fig. 4.5(c) and (d), the linear fitting results RSC of MoS_2 E^1_{2g} mode under 20× objective is –(0.026±0.001) cm^{-1}/mW, and under 100× objective is –(0.150±0.007) cm^{-1}/mW.

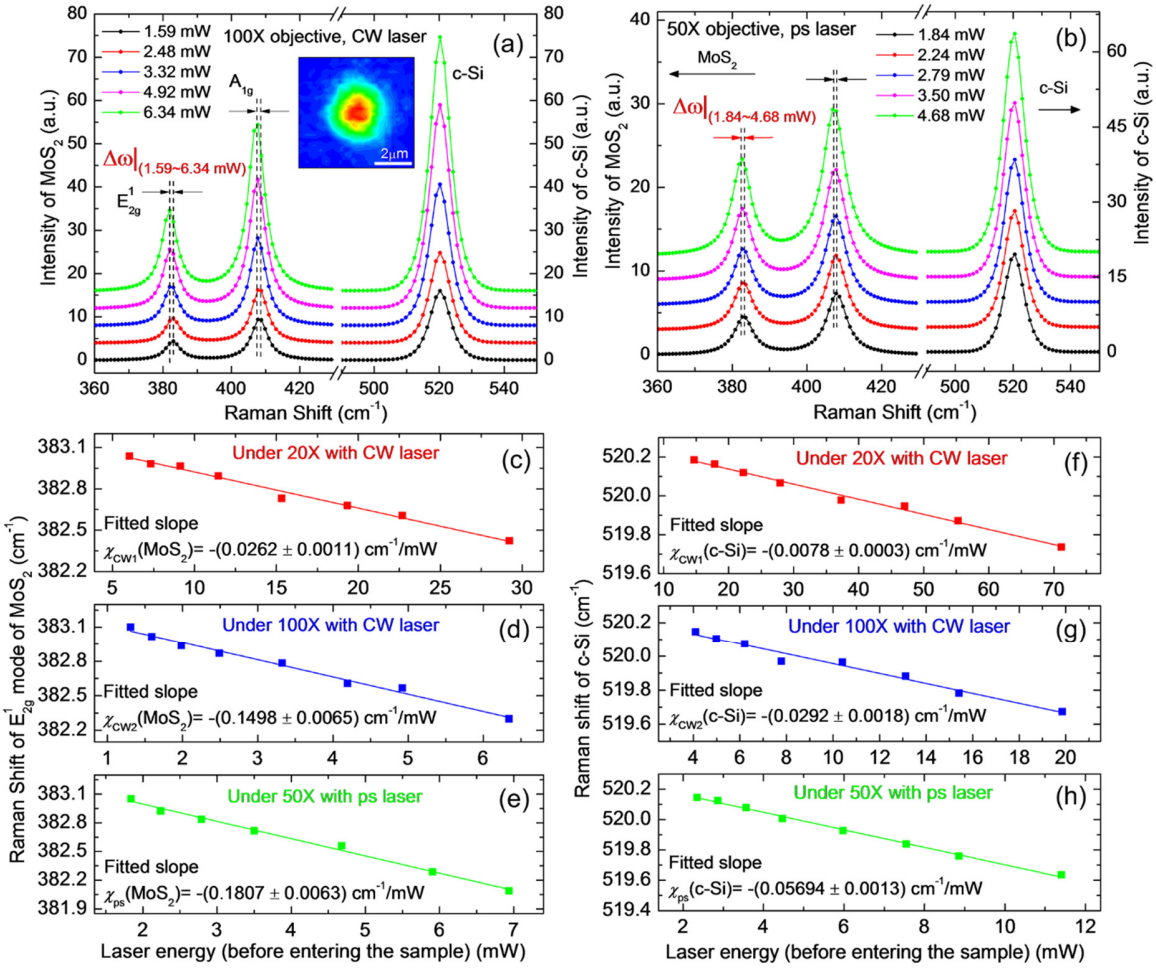

Figure 4.5 The Raman spectra and RSC results of 6.6 nm thick MoS_2 and c-Si.

The RSC value of c-Si, as shown in Fig. 4.5(f) and (g), under 20× objective is –(0.008±0.001) cm^{-1}/mW, and under 100× objective is –(0.029±0.002) cm^{-1}/mW. The linear dependence on the laser power for two different heating sizes indicates that there are no

significant changes in the thermal properties of materials in our considered laser power range.

By ps laser under 50× objective, as shown in Fig. 4.5(e) and (f), the RSC values of MoS_2 E^1_{2g} mode and c-Si are –(0.181±0.006) cm^{-1}/mW and –(0.057±0.001) cm^{-1}/mW, respectively. Also, RSC values for other six samples are summarized in Table 4.1. The RSC values roughly increase with increased MoS_2 thickness for both CW and ps laser heating. The main reason is that the thicker sample will absorb more energy when the thickness is smaller than its laser absorption depth, so a higher temperature rise will be expected. Under same laser power level (1 mW before it enters the sample), the Raman wavenumber change will increase.

4.3.2 Determination of *D* and *R*

Then a 3D numerical modeling based on the finite volume method is conducted to calculate the temperature rise to determine the hot carrier diffusivity (D) and the interface thermal resistance (R). The model is given in Section 3.3.2 and shown in Fig. 3.4. As considered in our previous work in Chapter 3, the MoS_2 nanosheets have the thickness dependent bandgap.[15] The change in the band structure with layer number is due to quantum confinement and the resulting change in hybridization between *pz* orbitals and S atoms and *d* orbitals on Mo atom.[5] This consideration, instead of using a constant E_g value, could help us determine R and D values with greater confidence. τ is set as 1 ns at room temperature.[99] After the model setup, we first solve the carrier diffusion equation (Eq. 3.1) and then the heat conduction one with the hot carrier concentration $\Delta N(\boldsymbol{r},t)$ used in the source term.

As shown in Fig. 3.2(e), based on the optical properties of these two materials TMM (Section 3.2.2), we could determine the transmitted power at the top surface (I_{01}), the reflected power at the bottom surface (I_{02}) of MoS_2 and the transmitted power in c-Si top surface (I_{03}).

As mentioned in the introduction section, our method could eliminate the errors from the local laser absorption evaluation and temperature coefficient calibration. Further data processing is given below with detailed explanations.

Table 4.1 Summary of Raman experiment results E^1_{2g} mode of MoS_2 and c-Si.

Sample thickness (nm)		χ_{CW1} (cm^{-1}/mW)	χ_{CW2} (cm^{-1}/mW)	χ_{ps} (cm^{-1}/mW)	Θ_1	Θ_2
6.6 nm	MoS_2	-(0.026±0.001)	-(0.150±0.007)	-(0.181±0.006)	0.145±0.008	0.829±0.046
	c-Si	-(0.008±0.0003)	-(0.029±0.002)	-(0.057±0.002)	0.136±0.007	0.513±0.035
7.8 nm	MoS_2	-(0.034±0.002)	-(0.171±0.009)	-(0.203±0.009)	0.169±0.010	0.841±0.059
	c-Si	-(0.008±0.0004)	-(0.027±0.002)	-(0.051±0.002)	0.151±0.010	0.531±0.038
9.6 nm	MoS_2	-(0.030±0.001)	-(0.158±0.006)	-(0.193±0.006)	0.157±0.007	0.818±0.043
	c-Si	-(0.009±0.0001)	-(0.027±0.001)	-(0.050±0.001)	0.166±0.004	0.523±0.026
12.0 nm	MoS_2	-(0.040±0.002)	-(0.187±0.007)	-(0.197±0.008)	0.204±0.011	0.947±0.051
	c-Si	-(0.009±0.0003)	-(0.029±0.0006)	-(0.056±0.003)	0.157±0.010	0.517±0.029
13.2 nm	MoS_2	-(0.033±0.001)	-(0.175±0.008)	-(0.187±0.006)	0.175±0.009	0.935±0.054
	c-Si	-(0.008±0.0004)	-(0.025±0.001)	-(0.059±0.003)	0.141±0.010	0.430±0.029
15.6 nm	MoS_2	-(0.040±0.001)	-(0.189±0.008)	-(0.201±0.006)	0.197±0.008	0.940±0.046
	c-Si	-(0.008±0.0005)	-(0.026±0.001)	-(0.050±0.003)	0.164±0.014	0.514±0.032
17.4 nm	MoS_2	-(0.045±0.002)	-(0.217±0.009)	-(0.210±0.005)	0.212±0.011	1.03±0.050
	c-Si	-(0.006±0.0002)	-(0.021±0.001)	-(0.054±0.001)	0.114±0.004	0.386±0.017

The temperature coefficient χ_T for MoS_2 and c-Si is unknown in our work. For steady-state Raman, the temperature rise (K/mW) of MoS_2 is from two parts: ΔT_1 by the direct laser energy absorption and ΔT_2 by the thermal energy absorption in c-Si. So we express the temperature rise by RSC as

$$\chi_{CW,\,MoS_2} = (\Delta T_1 + \Delta T_2) \times \chi_{T,\,MoS_2}. \tag{4.5}$$

We have $\Delta T_1 \propto (I_{01} + I_{02})$ and $\Delta T_2 \propto I_{03}$. Similar to MoS_2, the temperature rise (K/mW) of c-Si is also from two parts: ΔT_3 by thermal energy absorption in MoS_2 and ΔT_4 by the direct laser energy absorption in c-Si. It could be represented by RSC as

$$\chi_{\mathrm{CW,\,Si}} = (\Delta T_3 + \Delta T_4) \times \chi_{\mathrm{T,\,Si}}. \tag{4.6}$$

We also have $\Delta T_3 \propto (I_{01} + I_{02})$ and $\Delta T_4 \propto I_{03}$.

For the zero-transport state ps laser Raman, it is simpler. Only laser absorption happens (the fast thermalization process), and there is no heat conduction. So we could express the temperature rise (K/mW) of MoS_2 and c-Si by RSC as

$$\chi_{\mathrm{ps,\,MoS_2}} = \Delta T_5 \times \chi_{\mathrm{T,\,MoS_2}}, \tag{4.7}$$

$$\chi_{\mathrm{ps,\,Si}} = \Delta T_6 \times \chi_{\mathrm{T,\,Si}}, \tag{4.8}$$

where $\Delta T_5 \propto (I_{01} + I_{02})$ and $\Delta T_6 \propto I_{03}$.

From the 3D simulation, for the steady-state CW laser heating, we could get ΔT_1 and ΔT_3 by setting zero absorption in c-Si, ΔT_2 and ΔT_4 by setting zero absorption in MoS_2. From zero-transport state ps laser heating, we could directly get ΔT_5 and ΔT_6 by only considering the laser absorption.

From Eqs. 4.5 and 4.7, we express the normalized RSC of MoS_2 measured in the experiment as

$$\Theta_{\mathrm{MoS_2}} = \frac{\chi_{\mathrm{CW,\,MoS_2}}}{\chi_{\mathrm{ps,\,MoS_2}}} = \frac{\Delta T_1}{\Delta T_5} + \frac{\Delta T_2}{\Delta T_5}. \tag{4.9}$$

From Eqs. 4.6 and 4.8, we express the normalized RSC of c-Si as

$$\Theta_{\mathrm{Si}} = \frac{\chi_{\mathrm{CW,\,Si}}}{\chi_{\mathrm{ps,\,Si}}} = \frac{\Delta T_3}{\Delta T_6} + \frac{\Delta T_4}{\Delta T_6}. \tag{4.10}$$

The temperature rises ΔT_1, ΔT_2, ΔT_3, ΔT_5, and ΔT_6 are only related to the laser absorption in two materials. Additionally, we have $(\Delta T_2/\Delta T_5) \propto [I_{03}/(I_{01}+I_{02})]$ and $(\Delta T_3/\Delta T_6) \propto [(I_{01}+I_{02})/I_{03}]$. To eliminate the laser absorption effect, we multiply these two temperature rise ratios from Eqs. 4.9 and 4.10 as

$$\Theta_{MoS_2} = \frac{\Delta T_1}{\Delta T_5} + \frac{(\Delta T_2 / \Delta T_5) \times (\Delta T_3 / \Delta T_6)}{\Theta_{Si} - \Delta T_4 / \Delta T_6}. \tag{4.11}$$

In Eq. 4.11, term $\Delta T_2/\Delta T_5$ is not affected by laser absorption rate because both ΔT_1 and ΔT_5 are proportional to (I_{01}+I_{02}). Similarly, term $\Delta T_4/\Delta T_6$ also has nothing to do with laser absorption rate because both ΔT_4 and ΔT_6 are proportional to I_{03}. So the normalized RSC value is now only a function of two parameters: $\Theta(R, D)$, the effect from laser absorption evaluation is successfully ruled out. Take the 6.6 nm thick MoS_2 for example, from the 3D numerical simulation and Raman experiment, we could calculate Θ_1 and Θ_2 for MoS_2 in the (D, R) space. Especially, in the (D, R) space for the zero-transport state, ΔT_5 and ΔT_6 remain constant without changing other parameters. Note in our Raman experiment, as mentioned above, the measured RSC of both MoS_2 and c-Si are Raman-intensity weighted average of the sample. At a location of the sample, the local Raman intensity is proportional to the local laser intensity and the scattered Raman signal multi-reflected in the sample. For the zero-transport state, the measured temperature rise is also time averaged over the pulse width. All these have been considered in our modeling to evaluate the temperature rise of both MoS_2 and c-Si substrate.

Figure 4.6(a) and (b) show the calculated normalized RSC mapping for MoS_2. The experimentally obtained normalized RSC (the isolines) could be satisfied by many different

(D, R) pairs. We could determine the exact D and R values by combining the results from these two cases as shown in Fig. 4.6(c), the cross point of the blue (Θ_1) and dark red (Θ_2) dashed curves: D is 0.637 cm^2/s and R is 1.75×10^{-7} K·m^2/W. As discussed in Section 3.3.2, we use the normalized probability distribution function (Ψ) (0.6065) to present the results uncertainty as shown in the false color map of Fig. 4.6(c). Finally, the deduced R is $1.75^{+0.08}_{-0.08}\times10^{-7}$ K·m^2/W and D is $0.637^{+0.193}_{-0.154}$ cm^2/s. In addition, the final results and the uncertainty for the other six samples are summarized in Table 4.2 and also plotted in Fig. 4.7(a) and (b).

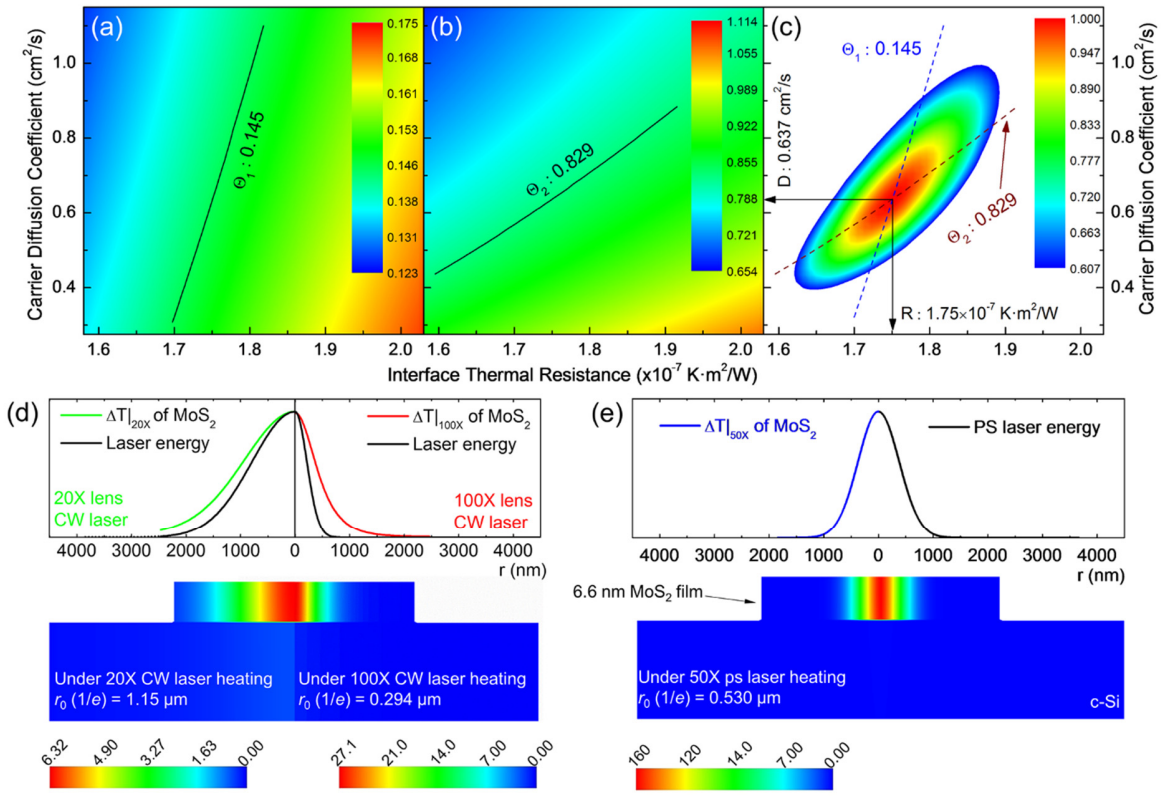

Figure 4.6 3D modeling results for the 6.6 nm thick MoS_2 sample.

To visualize hot carrier diffusion effect on the thermal distribution, similar to Section 3.3.2, we calculate the temperature rise distribution for the 6.6 nm thick MoS_2 sample under

CW laser heating with 20× (left part) and 100× (right part) objectives by the determined D and R and show the results in Fig. 4.6 (d). Compared with the laser energy distribution (dark curve), the temperature distribution of MoS_2 is out of the laser spot a lot, especially for the small heating size (100× objective). As discussed above, the diffusion length L_D (252 nm for 6.6 nm thick MoS_2) is only 1/5 of r_0 under 20× objective (1.15 μm) and almost same to that under 100× objective (294 nm). This makes the hot carrier diffusion effect on heat transport more prominent under 100× objective. For the zero-transport state ps laser heating, as shown in Fig. 4.6(e), the temperature rise of MoS_2 has almost the identical distribution to the ps laser energy distribution. The temperature rise of c-Si is so small due to its large volume and long laser absorption depth (~820 nm). This confirms that the R and D have negligible effect on the temperature rise of the samples.

Table 4.2 The summary of the hot carrier diffusivity from the 3D numerical modeling and data fitting, and the corresponding electron mobility and hot carrier diffusion length. Also, the calculated the interface thermal resistance.

Sample Thickness	D (cm^2/s)	μ ($cm^2/V{\cdot}s$)	L_D (μm)	R (10^{-7} $K{\cdot}m^2/W$)
6.6 nm	$0.637^{+0.193}_{-0.154}$	$25.5^{+7.71}_{-6.18}$	$0.252^{+0.139}_{-0.124}$	$1.75^{+0.08}_{-0.08}$
7.8 nm	$0.768^{+0.227}_{-0.210}$	$30.7^{+11.1}_{-8.41}$	$0.277^{+0.166}_{-0.145}$	$1.87^{+0.10}_{-0.09}$
9.6 nm	$0.753^{+0.201}_{-0.166}$	$30.1^{+8.04}_{-6.62}$	$0.274^{+0.142}_{-0.129}$	$1.51^{+0.06}_{-0.06}$
12.0 nm	$0.945^{+0.262}_{-0.209}$	$37.8^{+10.5}_{-8.37}$	$0.307^{+0.162}_{-0.145}$	$1.64^{+0.08}_{-0.07}$
13.2 nm	$1.07^{+0.31}_{-0.25}$	$42.7^{+12.6}_{-10.0}$	$0.327^{+0.177}_{-0.158}$	$1.29^{+0.06}_{-0.06}$
15.6 nm	$0.825^{+0.208}_{-0.176}$	$33.0^{+8.34}_{-7.02}$	$0.287^{+0.144}_{-0.132}$	$1.30^{+0.05}_{-0.04}$
17.4 nm	$1.25^{+0.31}_{-0.26}$	$50.0^{+12.5}_{-10.3}$	$0.354^{+0.177}_{-0.161}$	$1.22^{+0.06}_{-0.06}$

As discussed in Section 3.3.2, we can approximately treat the determined D in this work as unipolar carrier diffusivity of both electrons and holes. After conversion by Einstein

relation, for the 6.6 nm thick MoS_2 nanosheets sample, the measured D corresponds to a mobility of μ=25.5 cm^2/Vs. Moreover, 17.4 nm thick MoS_2 has μ=50.0 cm^2/Vs. Our measured μ is very close to the literatures value of 30-60 cm^2/Vs for few-layered MoS_2 on SiO_2,[53] ~70 cm^2/Vs for few-layered MoS_2 on Al_2O_3.[116] One of the biggest difference between the optical and electric methods to study the carrier movement is that we do not cover the sample (MoS_2 nanosheets) with a dielectric layer such as HfO_2.[12] Nevertheless, our optically measured mobility is still comparable to that measured using the contact methods. As described above, during the diffusion process, the electron-hole pair moves together so that the pair is electrically neutral and will not be influenced by the Coulomb scattering.[103] Hence, our results are much smaller than the theoretical optical-phonon-scattering-limited mobility (~400 cm^2/Vs).[129] Such high mobility could only be approached by adopting high-κ dielectric materials (*e.g.*, HfO_2, Al_2O_3) to build top-gated devices.[12,130] The dielectric layer is believed to affect (boost) the mobility because of the suppression of Coulomb scattering by the dielectric.[118,119] Besides, it has been shown that some of the reported mobility values may have been greatly overestimated in this top-gated geometry.[131]

4.3.3 Effect of MoS_2 Thickness on *R* and *D*

In order to elucidate how R and D values change with MoS_2 thickness, we plot them as a function of MoS_2 thickness as shown in Fig. 4.7(a)(b). The detailed results are also summarized in Table 4.2. As we can see, D has a relatively higher uncertainty than R. Both uncertainties come from the RSC fitting procedure and do not include systematic errors from the uncertainty of P, r_0 and NA. In Fig. 4.7 (b), the carrier diffusivity D is higher for thicker MoS_2 samples. D value almost doubles from 6.6 nm to 17.4 nm MoS_2 sample. A similar trend for this thickness-dependent D value is also found by Li *et al*. [132] This strong dependence may

be attributed to weaker in-plane electron-phonon interaction for thicker samples.[122] Besides, the additional MoS_2 layers could serve as a dielectric capping layer that enhances screening of long-range disorder.[53,122,132] And as the thickness increases, it has also been found that the effect of the charge impurities can be mitigated to some extent which leads to a mobility enhancement.[133]

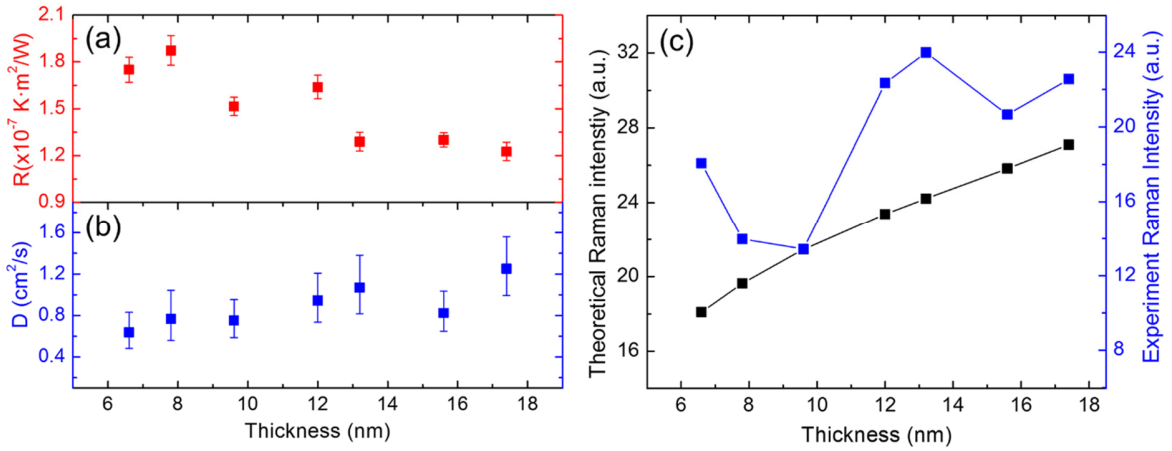

Figure 4.7 Interface thermal resistance and hot carrier diffusivity of seven MoS_2 samples supported on c-Si as a function of thickness. Theoretical Raman intensity *F* for the seven samples.

The interface thermal resistance we obtain here is in the order of 1.5×10^{-7} K·m^2/W. They are larger than what we found in previous work, such as the 8.4 nm MoS_2 on c-Si with *R* is 7.66×10^{-8} K·m^2/W.[68] We attribute this mainly to the unknown errors in laser absorption evaluation and Raman temperature coefficient calibration in our previous work while the ET-Raman completely eliminates the errors from laser absorption evaluation and temperature coefficient calibration. We feel the laser absorption is one of the factors giving the largest uncertainty. First of all, in our previous work and work reported in literatures by other researchers, the laser beam absorption was evaluated based on the refractive index of MoS_2 as 4.4. However, this property features very large deviations from sample to sample, and a broad

range of 3.05~5.20 has been reported in literatures.[15,85] Second, a small spacing between the 2D material and the substrate can induce strong optical interference and change the absorption behavior substantially. Unfortunately, quantitative knowledge of this spacing is still not available, and this significantly downgrades the measurement accuracy. Third, when calculating laser beam absorption, the laser is assumed normal to the 2D material in past work. In fact, the laser beam is focused with a finite numerical aperture. This could bring in great errors in laser absorption calculation. The smaller R of thicker samples reveals their better interface contact with the substrate, leading to accordingly improved interfacial energy coupling as found in our previous work.[68]

4.3.4 The Effect of Optical Properties

To further elaborate that the optical properties [the complex refractive index (n–ik_L)] of the sample have no effect on the results from ET-Raman technique, we vary the n and k_L values to calculate the laser absorption rate based on TMM as shown in Table 4.3. In the above 3D numerical simulation, the preset complex refractive index for 6.6 nm MoS_2 is 4.4–1.1i.[15] Based on different combinations of n and k_L values of MoS_2, we calculate the temperature rise ΔT_1 to ΔT_6 and deduce $\Theta(MoS_2)$ for both 20× and 100× objectives (two sub-states). $\Theta(MoS_2)$ has a variance of less than one thousandth while changing n or k_L value as shown in Table 4.3. For example, we reduce n by half and keep k_L value (2.2–1.1i), the calculated $\Theta(MoS_2)$ only increases by 0.11‰. So the change could be neglected. Because the R and D values are determined from $\Theta(MoS_2)$ under 20× and 100× objectives, so it is conclusive that the ET-Raman technique could eliminate the errors brought in by optical absorption evaluation.

As discussed above, the optical properties of the samples are difficult to accurately determine and vary a lot from sample to sample. Additionally, based on the determined optical

properties, the laser absorption rate is estimated assuming a vertical incident laser beam. However, the focused laser beam converges along the propagation direction and this is very complicated to be taken into account when evaluating the laser absorption level. For monolayer MoS_2, the absorbance level experimentally determined varies from 4% to 9%.[14,134] Among the error sources for Raman-based thermal probing technique, the relative error in the laser absorption was by far the dominant contributor. Moreover, the accuracy of the measurement is strongly limited by the uncertainty of the optical absorption evaluation. To this end, some measured the laser absorption level by themselves to consider the absorption variation among samples[75] or discussed the results by referring different absorbance levels obtained from others.[44] All of these treatments still have to consider the effects and errors from optical absorption evaluation so that our results provide the most accurate understanding to date.

Table 4.3 The study results for the effect of the optical properties of MoS_2 on final normalized RSC values.

Objective lens	Complex index	ΔT_1 (K)	ΔT_2 (K)	ΔT_3 (K)	ΔT_4 (K)	ΔT_5 (K)	ΔT_6 (K)	$\Theta(MoS_2)$
20×	4.4-1.1*i*	1.95	0.168	0.124	0.162	17.24	0.629	0.097
	2.2-1.1*i*	2.30	0.203	0.146	0.197	20.30	0.762	+0.11‰
	5.5-1.1*i*	1.80	0.143	0.114	0.139	15.87	0.538	+0.05‰
	4.4-0.55*i*	2.08	0.193	0.132	0.187	18.43	0.723	-0.21‰
	4.4-2.2*i*	1.70	0.129	0.108	0.125	15.05	0.484	-0.02‰
100×	4.4-1.1*i*	11.80	0.335	0.242	0.358	17.24	0.629	0.550
	2.2-1.1*i*	13.89	0.406	0.285	0.433	20.31	0.762	+0.21‰
	5.5-1.1*i*	10.86	0.287	0.223	0.306	15.87	0.538	+0.50‰
	4.4-0.55*i*	12.61	0.385	0.259	0.411	18.43	0.723	-0.13‰
	4.4-2.2*i*	10.29	0.258	0.211	0.275	15.05	0.484	-0.10‰

4.3.5 Thickness Effect on Interface Energy Transport: Interpretation from Interface Structure

As we briefed above, the MoS_2-substate interface could have a small spacing, and this spacing will significantly change the laser absorption in MoS_2. This effect has not been considered in the past for laser absorption evaluation. Our ET-Raman technique completely rules out this effect. To have a deeper understanding of this effect, and shed light on above interfacial thermal resistance results, we perform the Raman intensity enhancement study to reveal the interface structure. As has been investigated, the local interfacial energy coupling will decrease significantly if there is even a tiny spacing (*e.g.* 0.1 nm) at the interface.[32,68] At the same time, the spacing will induce Raman intensity variation. Therefore, in this section we study the Raman intensity of the MoS_2 sample against its thickness, in anticipation to uncover the local interface spacing information.

As we briefed above, the MoS_2-substate interface could have a small spacing, and this spacing will significantly change the laser absorption in MoS_2. This effect has not been considered in the past for laser absorption evaluation. Our ET-Raman technique completely rules out this effect. To have a deeper understanding of this effect, and shed light on above interfacial thermal resistance results, we perform the Raman intensity enhancement study to reveal the interface structure. As has been investigated, the local interfacial energy coupling will decrease significantly if there is even a tiny spacing (*e.g.* 0.1 nm) at the interface.[32,68] At the same time, the spacing will induce Raman intensity variation. So in this section we study the Raman intensity of the MoS_2 sample against its thickness, in anticipation to uncover the local interface spacing information.

Figure 4.7(c) shows the comparison of the experiment Raman peak intensity of MoS_2 E^1_{2g} mode and the theoretical Raman intensity *F* for our seven MoS_2 samples (the calculation method is described in Section 2.3.3). In the comparison, we assume that there is no spacing for 9.6 nm thick MoS_2 sample since it has the lowest theoretical Raman intensity among the seven samples. The deviation of the calculation results from our experiment results confirms the spacing existence for other six MoS_2 samples, especially for the 6.6 nm and 13.2 nm thick ones. This spacing can significantly increase the interface thermal resistance and local laser energy absorption. For the first four samples (6.6 ~ 12.0 nm thick), the 9.6 nm thick sample has the lowest *R* value due to its perfect interface contact (assumed no spacing).

Additionally, the thermal expansion coefficient (TEC) of MoS_2 nanosheets (~10^{-5} K^{-1})[135,136] is larger than that of c-Si (3.9×10^{-6} K^{-1})[137]. Also during the experiment, MoS_2 will have a higher temperature rise than c-Si. So when the sample is under laser heating, these two factors (spacing existence and TEC mismatch) combine to lead to interfacial thermal expansion mismatch between MoS_2 nanosheets and c-Si. This could result in increased local interface spacing, less efficient heat transfer, and a higher interfacial thermal resistance. For the last four samples (12.0 ~17.4 nm thick), the *R* value has a declining trend. We attribute this to the fact that thicker MoS_2 samples may have smaller TEC value just like PET (polyethylene terephthalate) film.[138] The TEC mismatch between MoS_2 nanosheets and c-Si substrate therefore decreases. As a result, the local interface spacing increase during experiment will become smaller than the thinner samples, leading to a better interface energy coupling. On the other hand, as we studied before,[68] thicker samples have better mechanical stiffness which could help form a better contact with c-Si substrate during sample preparation. This could also account for the reduced *R* for thicker samples in this work.

Additionally, for some Raman-based thermal probing techniques used in literatures,[44] the TEC mismatch could also introduce large errors in the Raman temperature coefficient calibration. During the laser heating, the temperature rises of two materials are different. Especially, the temperature rise of c-Si is very small due to its large thermal conductivity. As a result, the two materials will experience different mechanical stresses. However, during the calibration experiment, they are kept at the same temperature level. Therefore, the thermal expansion mismatch between the two materials are different in calibration and experiment. As a result, the Raman wavenumber changes caused by the stress in MoS_2 during the calibration are very complicated to be examined. Fortunately, as mentioned above, we do not need the Raman temperature calibration results for ET-Raman technique. Therefore, this kind of errors could be completely ruled out.

4.3.6 Applicability of ET-Raman Technique

This ET-Raman technique could also be applicable for other sample structures, such as suspended 2D material. For this structure, the absorbed laser energy could only dissipate along the in-plane direction. Additionally, the sample thermal relaxation time will be longer and there could be a heat accumulation effect by laser pulses. Therefore, the sample could be easily destroyed during the first several laser pulses. However, by controlling the laser to have a longer cooling time between pulses (low repetition rate), we could still apply ET-Raman to characterize suspended 2D materials. By using two different laser heating sizes in steady state laser heating, and one state in pulsed laser (nanosecond or picosecond laser) heating, both in-plane thermal conductivity and hot carrier diffusivity could be determined.

We can also use ET-Raman to study other 2D materials, such as other TMDs, black phosphorus, and graphene. However, the following points should be paid attention to. First,

for materials with an indirect bandgap, like few-layered MoS_2, the radiative recombination of carriers is strongly restricted so that the energy carried by the hot carriers will be transferred to local phonons. For these materials, we could just apply ET-Raman demonstrated in this work to determine their *D* and *R* values. Second, for materials with a direct bandgap, such as single-layer MoS_2, the radiative transitions dominate the recombination process. A coefficient may be applied to the last term of Eq. 3.2 to describe how much energy could transfer to local phonons. Third, for the materials without bandgap, like graphene, no hot electrons are generated during laser excitation. Electrons will carry the photon energy and transfer the energy to local lattice by electron-phonon scattering. So heat conduction equations for both electron and phonon will be needed to describe the diffusion process. Last, under extreme *e.g.*, the material has a very long or very short hot carrier diffusion length compared with the laser heating spot size, the hot carrier diffusivity *D* will become difficult to measure.

CHAPTER 5. INTERFACE THERMAL ENERGY TRANSPORT AND HOT CARRIER DIFFUSION OF FL MOS2 ON GLASS SUBSTRATE

Currently reported optical-phonon-scattering-limited carrier mobility of MoS_2 is up to 417 $cm^2/V{\cdot}s$ with two-side dielectric screening: one normal-κ side and one high-κ side. Here, using the ET-Raman technique, we discover the very fast hot carrier diffusion in μm-scale (lateral) unconstrained MoS_2 (1.8-18 nm thick) on glass substrate that only provides one-side normal-κ dielectric screening. The measured D spans from 0.76 to 9.7 cm^2/s. A nonmonotonic thickness-dependent D trend is discovered and it peaks at 3.0 nm thickness. This is explained by the competition between two physics: with increased sample thickness, the increase of sufficient screening of the substrate results in a higher mobility, but thicker samples are subject to more surface contamination, loose substrate contact and weaker substrate dielectric screening. The corresponding carrier mobility varies from 31.0 to 388.5 $cm^2/V{\cdot}s$. This mobility is surprisingly high considering the normal-κ and single side dielectric screening by the glass substrate. It is a direct result of the less-damaged structure of MoS_2 that is superior over MoS_2 samples measured in literatures that are subject to various post-processing to facilitate measurement. The very high hot carrier mobility reduces the local carrier concentration and will give a boost of Raman signal, which is further confirmed by our Raman signal study and comparison with the theoretical one.

This chapter begins with brief characterization of MoS_2 samples supported on glass substrate in Section 5.1. Then, in Section 5.2, we will focus on the physical model for this case and data processing details. The discussion about determination of R and D and structure and physics analysis is given in Section 5.3.

5.1 FL MoS_2 on Glass Substrate preparation and Characterization

To date, silicon wafer is very popular for standard integrated circuit processing and ideal substrates for creating transistors due to its extreme uniformity, chemical, and mechanical strength.[139] So tremendous work has been focused on the study of semiconductor materials supported on silicon substrate. However, in other applications like display pixel backplane and peripheral logic devices,[140,141] glass or plastic substrates are more suggested. For MoS_2 supported on glass substrate, a few related studies have been reported but only limited to simple FET structure.[142-144] From another aspect, the mechanical properties of MoS_2 nanosheets can be strongly affected by the substrate property and morphology. Unlike the polished c-Si substrate we used in our previous work,[145] MoS_2 prepared through mechanical exfoliation onto the glass substrate does not follow its nanoscale rough surface but instead is supported by the high points on the substrate. This surface roughness affects the energy coupling of MoS_2 nanosheets and the substrate, therefore may cause a local variance in the sample's electrical and mechanical properties.[146,147] Tang *et al*. indicated that the loose contact at the interface could significantly increase the interface thermal resistance.[148] Also, a large temperature rise in glass substrate is expected in experiment due to its relatively low thermal conductivity.[149] However, its temperature profile could not be obtained by Raman spectroscopy because there is no prominent Raman spectrum in most glass substrates. Additionally, compared with c-Si substrate, the better dielectric effect from the glass substrate (SiO_2) could dramatically increase the carrier diffusivity of its supported MoS_2 nanosheets.[53,106,132] All of these additional considerations when using glass instead of Si as substrate make it very challenging and complicated to study MoS_2 nanosheets supported on glass substrate.

Still by micromechanical exfoliation method, six few-layered MoS_2 samples were prepared. The samples are mounted on the glass substrate (Fisher brand pre-cleaned microscope slide) instead of the c-Si substrate. An optical microscope, atomic force microscope (AFM) and Raman spectroscopy are used to identify and locate the MoS_2 nanosheets. The MoS_2 nanosheets have the lateral size ranging from 7 to 16 µm. Compared to the c-Si substrate, MoS_2 nanosheets on glass substrate have better optical contrast,[150] so we could easily identify larger ultrathin sheets.

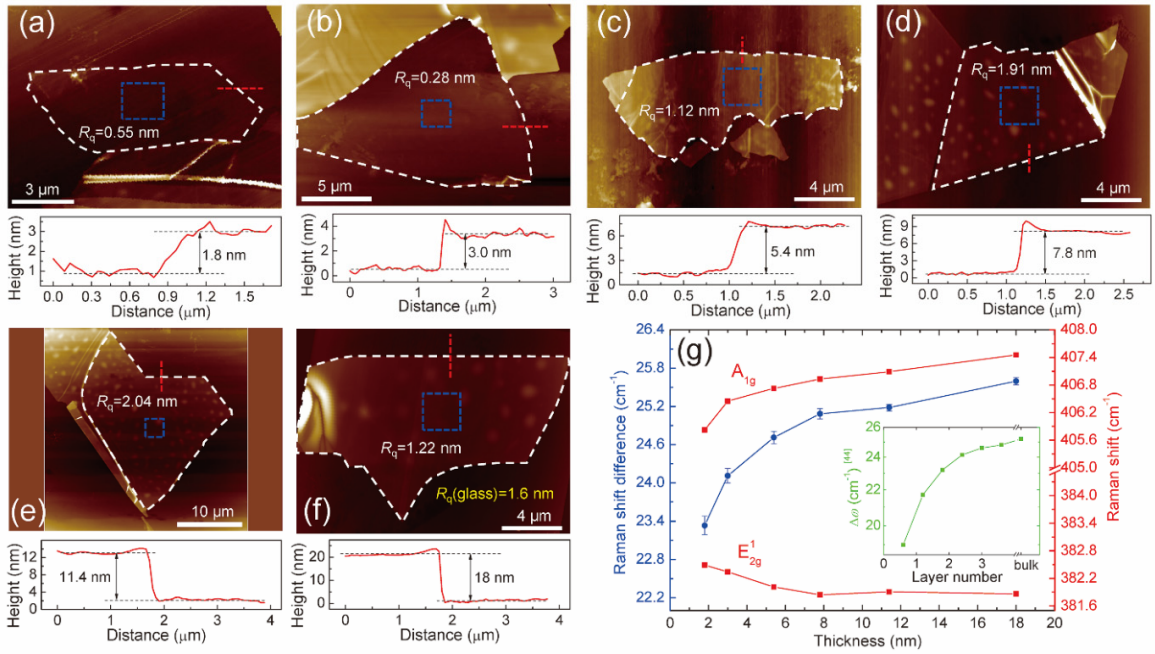

Figure 5.1 Six MoS_2/glass samples AFM results and Raman shift position study results.

Figure 5.1 (a)-(g) show AFM images of the six MoS_2 samples on glass substrate. In each image, we use the dashed white circle to mark the sample area; the red dashed line to indicate the height profiles measurement area and the result is shown beneath the AFM image. The samples have a thickness of 1.8 nm, 3.0 nm, 5.4 nm, 7.8 nm, 11.4 nm, and 18 nm, respectively. Take the 1.8 nm thick MoS_2 for example, it has a surface roughness (R_q) of 0.55

nm. Also, the substrate (glass) has a R_q (glass) around 1.6 nm which is pretty large compared with the c-Si substrate we used in previous works (R_q is only 0.09 nm). This is because that the glass substrate is not polished. The higher roughness could also suggest the wrinkles or ripples in the samples. The white dots could be the gel film residues introduced from the MoS_2 sample preparation process because of the high points of the glass substrate. During the sample transfer process (from gel film to glass substrate), the MoS_2 film could only have good contact with the high points of glass, and this attraction is stronger than that between MoS_2 film and the gel film. However, the suspended area (no high point support) of MoS_2 film has much weaker attraction with the glass. Therefore, the residues from gel film could be easily left on the MoS_2 film surface when the gel film detaches. For the thick samples, the interlayer van der Waals interaction within the MoS_2 film is very strong compared to the attraction between MoS_2 and gel film. However, for the ultrathin samples (1.8 nm has only three atomic layers), the final MoS_2 film sample on glass experiences one last exfoliation when the gel film detaches it. Around half of MoS_2 film is taken away by the gel film instead of being fully released to the glass substrate. So the thin sample surface is free of residue from the gel film.

Besides, compared with the hydrophobic silicon, the glass is hydrophilic and large numbers of water molecules may be introduced to the interface. For the thick samples, the white dots are more evident and dense. We speculate that the water molecules could permeate through the thinner MoS_2 nanosheets more easily and evaporate into the environment. The surficial water could also affect the samples' thermal and electrical properties. Fig. 5.1(g) shows the thickness dependence of Raman shift of two Raman modes of MoS_2 which agrees well with our previous results and validates our AFM measurement results.

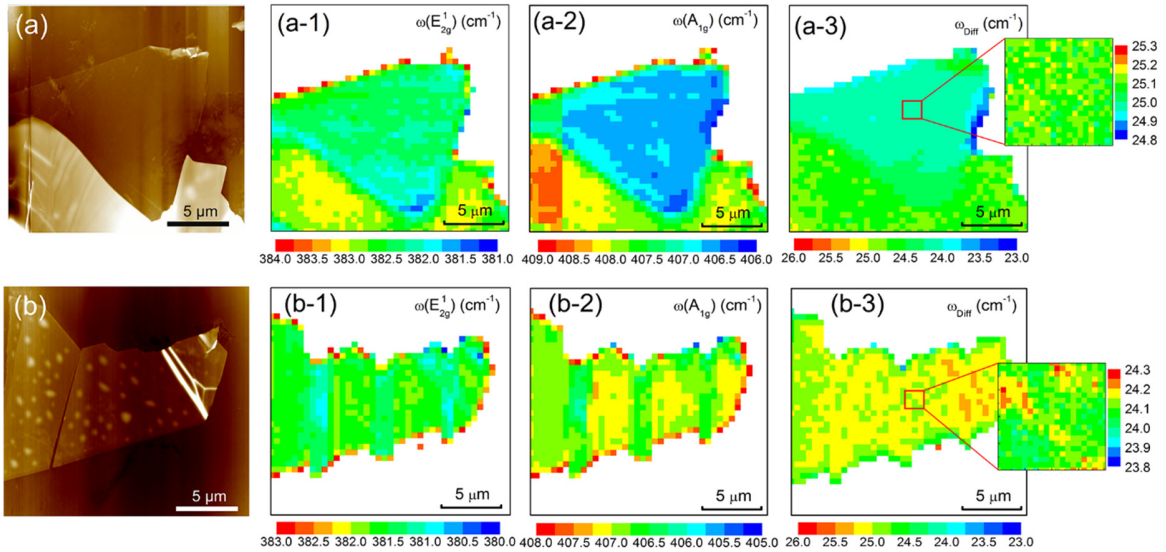

Figure 5.2 Raman shift mapping false color images of 3.0 nm and 7.8 nm thick MoS_2 samples.

To have a better idea of the uniformity of sample surface structure, we also do the Raman shift mapping by using CW laser line for the 3.0 nm and 7.8 nm thick MoS_2 samples. Here we take the 3.0 nm thick MoS_2 sample for instance to discuss the Raman mapping results. Fig. 5.2(a) shows its AFM image with a width of 20 μm. The Raman spectra are recorded for each point with a step size of 500 nm and then they are analyzed by an MATLAB-based automatic fitting program to determine the Raman shift information. Fig. 5.2(a-1) and (a-2) show the false color images created from the Raman shift of E^1_{2g} and A_{1g} modes as a function of position. Fig. 5.2(a-3) shows the Raman shift difference of these two modes. Because we did the Raman experiments for *D* and *R* determination on a small area of the sample, to gather more information of that area, we zoom in the mapping area as marked with red square in Fig. 5.2 (a-3). In the enlarged view, the mapping step size for this area is 100 nm. The relatively small variance of Raman shift difference mapping confirms the uniform sample thickness. In the mapping result of the samples, the boundary does not have a smooth transition. We attribute

this to the possible real structure variance. Besides, as just discovered in our group, the asymmetry of Raman scattering by structure variation could also account for this result.[151]

5.2 Physical Model and Data Processing

In ET-Raman, similar to the work in last chapter, we construct different energy transport states in both space and time domains, and examine the sample's thermal response. We perform two sub-states for steady-state heating with different laser heating sizes by different objective lenses (100× and 20×) to differentiate the effect of D and R. The laser spot has a radius of 1.50 μm and 0.366 μm (1/e profile) for 20× and 100× objectives, respectively. By collecting and analyzing Raman signal under different laser power (P), we could get the RSC: $\chi_{CW}=\partial\omega/\partial P$. Two RSC values could be obtained for each sample by varying the objective objectives, χ_{CW1} for 20× objective, χ_{CW2} for 100× objective.

Then we generate two zero-transport states using the ps laser and obtain RSC under both 50× and 100× objectives as χ_{ps1} and χ_{ps2}, respectively. Within each pulse (13 ps), the thermal diffusion length for both MoS_2 nanosheets and glass substrate is around 38 nm and 6.6 nm, respectively. ($L_t = 2\sqrt{\alpha_k t_0}$). They are all much smaller than the laser spot size (r_0 is 0.246 μm for 100× objective, and 0.431 μm for 50× objective). Hence, the heat conduction in the laser heating region has a very weak effect on the temperature rise. The relaxation time of the MoS_2 nanosheets supported on glass substrate (R~10^{-6} K·m^2/W) can be estimated as $\delta z \cdot \rho c_p R$=37.8 ns which is even longer than the ps laser cooling time (20.8 ns). So the temperature of the sample could not be fully cooled down to its original. Instead, it will be heated again when next pulse comes until the sample reaches thermal equilibrium with the environment. Hence, there is a steady-state heat accumulation effect as shown in Figure 5.3. As a result, the temperature rise (χ_{ps}) is from a combined effect of a single pulse and the steady-

state accumulation of the heat. Especially, the heating size effect in the steady-state accumulation is negligible. So, the temperature rise induced by the accumulation is almost identical under same laser power level (*e.g.*, 1 mW) when the thermal equilibrium reaches. However, the temperature rise from a single pulse is mostly coming from the volumetric heat capacity of the sample (ρc_p) and will be different for different heating sizes. By comparing the zero-conduction state under different heating size (100× and 50× objectives), we could eliminate the steady-state accumulation effect. As a result, we could use these zero-transport states (ps laser heating) to distinguish the roles of ρc_p and (R, D) with a negligible contribution of D and R to the temperature rise.

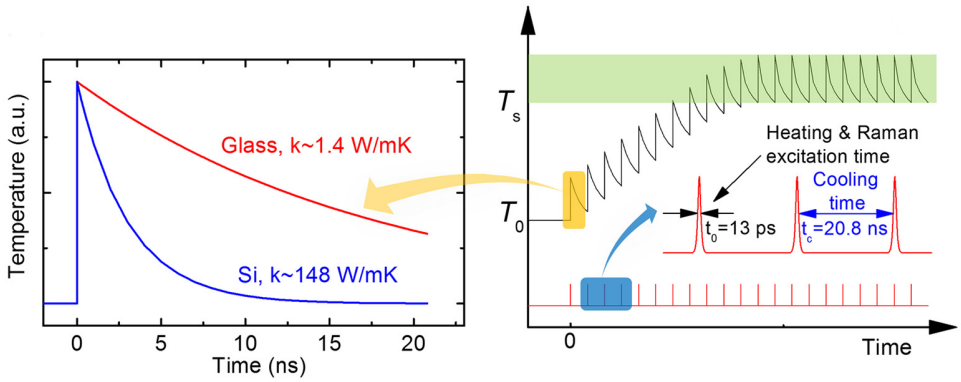

Figure 5.3 Thermal relaxation time difference between Si and glass, and heat accumulation effect in glass under ps laser heating.

For the MoS_2 nanosheets on glass substrate, after the steady-state and zero-transport heating experiments, we define the dimensionless normalized RSC as $\Theta_1 = \chi_{CW1}/(\chi_{ps2}-\chi_{ps1})$ and $\Theta_2 = \chi_{CW2}/(\chi_{ps2}-\chi_{ps1})$. Moreover, this normalized RSC completely rules out the effects of laser absorption, Raman temperature coefficients, and the pulse accumulation effect. Θ_1 and Θ_2 are only a function of the 2D material and substrate materials' ρc_p, R, and D. Through a 3D heat conduction model to include all these properties, we could finally determine D and R of the

2D material. Consequently, by ET-Raman, the uncertainties from the evaluations of absorbed laser power level and absolute temperature rise could be eliminated.

5.3 Results and Discussion

5.3.1 Experiment Results

For both steady-state and zero-transport state Raman experiments, eight room-temperature Raman spectra are collected at different laser power by the control computer to find the laser power coefficient for each sample. The CW laser energy is varied from 0.38 mW to 2.13 mW (0.090 to 0.506 MW/cm^2) under the 100× objective, and from 1.34 to 7.59 mW (0.019 to 0.107 MW/cm^2) under the 20× objective. The ps laser energy is from 0.195 to 1.106 mW (pulse power density is from 0.053 to 0.303 GW/cm^2) under 50× objective and from 0.126 to 0.611 mW (pulse power density is from 0.106 to 0.514 GW/cm^2) under 100× objective. Note that this laser power is the level just before the laser enters the MoS_2 sample surface. Especially, for the ps laser Raman, the photon absorption saturation has to be avoided and make the sample stay within the linear temperature dependence range for Raman properties.[126,127] For the 1.8 nm thick MoS_2 under 100× objective with ps laser, as shown in Fig. 5.4(f), the saturable absorption begins around 0.602 GW/cm^2, albeit smaller than the saturation intensity from the literature. So the saturation intensity for different samples may vary a little bit and very careful selection of the laser power range will be necessary.

Next, we take the 1.8 nm thick sample to illustrate the results in this work. Fig. 5.4 (a) shows five representative room temperature Raman spectra and their corresponding Lorentzian fits of MoS_2 under 100× objective by CW laser. Results under 50× objective by ps laser are shown in Fig. 5.4 (b). In Fig. 5.4 (a), with increased laser power, both two modes of MoS_2 shift to left (red shift) linearly and the shifts are visible as $\Delta\omega|(0.38\text{ mW} \sim 2.13\text{ mW})$ by CW laser

and $\Delta\omega|(0.19\ \text{mW} \sim 1.11\ \text{mW})$ by ps laser for MoS_2. These Raman shift changes show that the temperature of the sample heating area becomes higher under a higher laser power. Note that the Raman linewidth of MoS_2 from CW laser is smaller than that from ps laser, as shown in Fig. 5.4(a) and (b). This is because the observed signal of Raman is not solely dependent on the spectral resolution of the spectrometer, but it is also dependent on the linewidth of the laser. The CW laser comes with a spectral linewidth less than 0.01 pm. However the picosecond laser has a linewidth around 9 pm. However, this will not affect the absolute Raman peak position. Additionally, we use the linear fitting results from Raman shift position against laser power to determine the final results. So the absolute difference in Raman spectra from two laser sources will be ruled out.

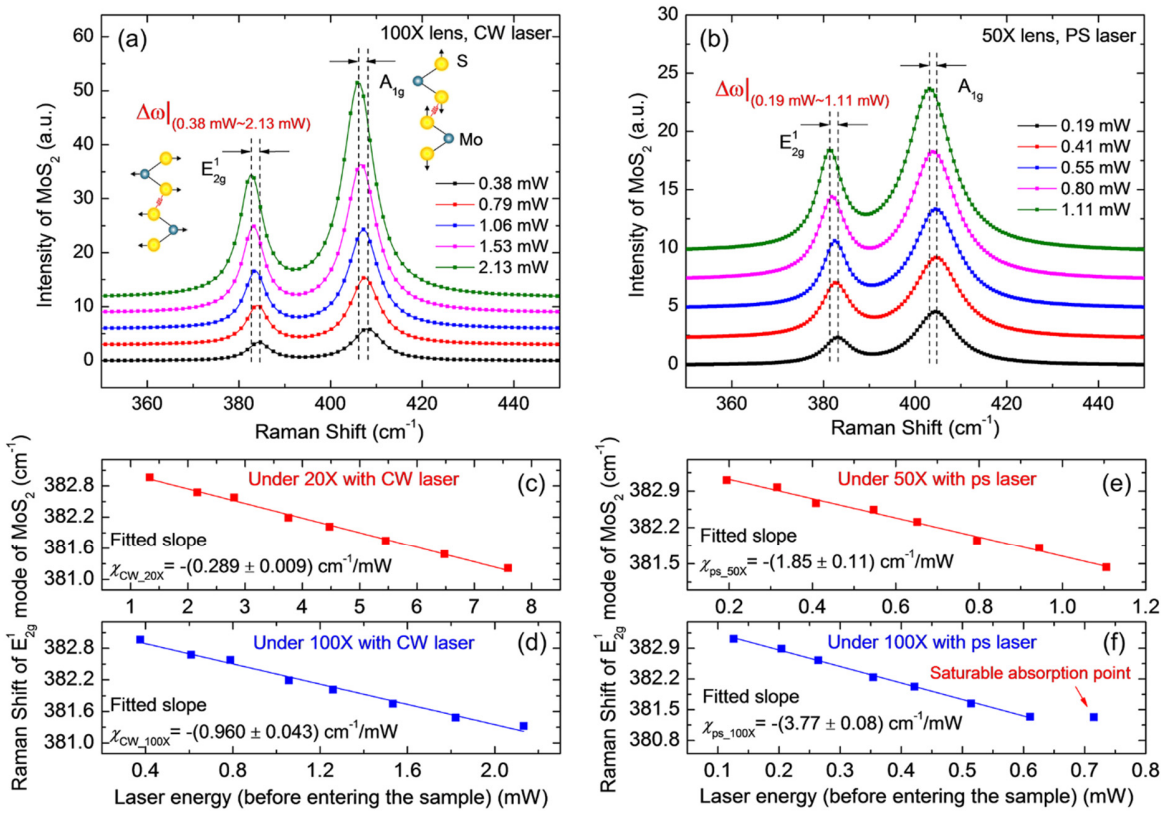

Figure 5.4 The ET-Raman experiments results of 1.8 nm thick MoS_2 nanosheets.

By using CW laser, as shown in Fig. 5.4(c) and (d), the linear fitting results RSC of MoS_2 E^1_{2g} mode under 20× objective (χ_{CW1}) is –(0.289±0.009) cm^{-1}/mW, and under 100× objective (χ_{CW2}) is –(0.960±0.043) cm^{-1}/mW. They are also much higher than the corresponding RSC (CW) value of MoS_2 (6.6 nm thick) on c-Si substrate: –0.026 cm^{-1}/mW (20× objective) and –0.150 cm^{-1}/mW (100× objective).[145] For glass substrate, the heat dissipation is less efficient due to its small thermal conductivity. So a larger temperature rise is expected for MoS_2 supported on glass substrate.

Table 5.1 Summary of Raman experiment results and thickness dependent bandgap of six MoS_2 samples.

Sample thickness	**1.8 nm**	**3.0 nm**	**5.4 nm**	**7.8 nm**	**11.4 nm**	**18.0 nm**
Band gap	1.64 eV	1.54 eV	1.42 eV	1.35 eV	1.31 eV	1.30 eV
χ_{CW1} **(cm^{-1}/mW)**	-(0.289 ±0.009)	-(0.344 ±0.014)	-(0.289 ±0.009)	-(0.370 ±0.017)	-(0.369 ±0.017)	-(0.240 ±0.010)
χ_{CW2} **(cm^{-1}/mW)**	-(0.960 ±0.043)	-(0.940 ±0.041)	-(0.973 ±0.040)	-(0.936 ±0.044)	-(0.784 ±0.032)	-(0.620 ±0.023)
χ_{ps1} **(cm^{-1}/mW)**	-(1.85 ±0.11)	-(1.43 ±0.03)	-(1.24 ±0.02)	-(1.10 ±0.04)	-(0.71 ±0.02)	-(0.42 ±0.01)
χ_{ps2} **(cm^{-1}/mW)**	-(3.77 ±0.08)	-(3.09 ±0.06)	-(2.72 ±0.08)	-(2.04 ±0.06)	-(1.48 ±0.02)	-(1.05 ±0.02)
Θ_1	0.150 ±0.010	0.207 ±0.010	0.251 ±0.014	0.394 ±0.025	0.375 ±0.017	0.382 ±0.021
Θ_2	0.499 ±0.038	0.566 ±0.030	0.658 ±0.034	1.00 ±0.06	1.03 ±0.05	0.988 ±0.053

By using ps laser under 50× and 100× objectives, as shown in Fig. 5.4(e) and (f), the RSC values of MoS_2 E^1_{2g} mode are –(1.85±0.11) cm^{-1}/mW and –(3.77±0.08) cm^{-1}/mW, respectively. The power coefficient under 100× objective (χ_{ps2}) is larger than that under 50× objective (χ_{ps1}). This difference comes from the temperature rise from the single pulse. Just

like in CW laser heating, ps laser under 100× objective has a higher power density. Similarly, for 50× objective, it is also much higher than the corresponding RSC (ps) value of MoS_2 (6.6 nm thick) on c-Si substrate –0.057 cm^{-1}/mW.[145] The RSC values for all six samples are summarized in Table 5.1.

5.3.2 Determination of *D* and *R*

We apply the 3D numerical modeling based on the finite volume method to calculate the temperature rise to determine the *D* and *R* values. Take the 1.8 nm thick MoS_2 for example, from the 3D numerical simulation and Raman experiment, we could calculate the normalized RSC (Θ_1 and Θ_2) for MoS_2 in the (*D*, *R*) space. As mentioned in Section 4.3.2, the MoS_2 nanosheets have the thickness dependent bandgap.[15] As summarized in Table 5.1, we extract the E_g values to determine *R* and *D* values. This consideration is especially important and necessary for relatively thin samples: 1.8 nm MoS_2 has E_g as 1.64 eV, and it dramatically decreases down to 1.42 eV for 5.4 nm. Fig. 5.5 (a) and (b) show the calculated normalized RSC mapping for MoS_2. Many different (*D*, *R*) pairs could satisfy the experimental normalized RSC (the isolines). By combining the results from these two cases as shown in Fig. 5.5 (c), we determine the exact *D* and *R* values from the cross point of the blue (Θ_1) and dark red (Θ_2) dashed curves. Finally, the deduced *R* is $1.28^{+0.16}_{-0.16} \times 10^{-6}$ $K \cdot m^2/W$ and *D* is $4.17^{+1.33}_{-0.97}$ cm^2/s. The final results with the uncertainty for all six samples are summarized in Table 5.1 and also plotted in Fig. 5.5 (a) and (b).

Then, we obtain the temperature profile from the 3D modeling (by the determined *D* and *R*) for the 1.8 nm thick MoS_2 sample and its substrate, under 20× (left part) and 100× (right part) objectives with CW laser heating. As shown in Fig. 5.5 (d), this visualizes the hot carrier diffusion effect on the thermal energy distribution. Especially, the temperature rise in glass

results from the thermal energy transferred from upper MoS_2. The low thermal conductivity of glass restricts the heat dissipation. Compared with the laser energy distribution (dark curve), the temperature distribution of MoS_2 is out of the laser spot a lot, especially for the small heating size (100× objective). For the zero-transport state ps laser heating modeling, we only consider the temperature rise from the single pulse. As shown in Fig. 5.5 (e), the temperature rise of MoS_2 almost has the same distribution to the ps laser energy distribution. This confirms that the R and D have a negligible effect on the temperature rise of the samples. The temperature rise of glass substrate is close to zero due to negligible heat transport from MoS_2 during very short ps laser pulse duration.

Table 5.2 Summary of the interface thermal resistance (R) and hot carrier diffusivity (D) from the 3D numerical modeling and data fitting, the corresponding electron mobility (μ) and hot carrier diffusion length (L_D).

Sample Thickness	D (cm^2/s)	μ ($cm^2/V{\cdot}s$)	L_D (nm)	R (10^{-6} $K{\cdot}m^2/W$)
1.8 nm	$4.17^{+1.33}_{-0.97}$	$166.8^{+53.3}_{-39.1}$	$645.8^{+365.1}_{-312.6}$	$1.28^{+0.16}_{-0.16}$
3.0 nm	$9.71^{+1.89}_{-1.57}$	$388.5^{+75.5}_{-62.8}$	$985.5^{+434.4}_{-396.2}$	$1.94^{+0.18}_{-0.17}$
5.4 nm	$5.17^{+1.90}_{-0.70}$	$206.8^{+75.9}_{-28.0}$	$719.0^{+435.5}_{-264.7}$	$1.16^{+0.15}_{-0.15}$
7.8 nm	$2.33^{+1.09}_{-0.79}$	$93.3^{+43.4}_{-31.4}$	$482.9^{+329.4}_{-212.9}$	$2.07^{+0.31}_{-0.29}$
11.4 nm	$0.76^{+0.45}_{-0.32}$	$30.2^{+18.1}_{-13.0}$	$274.9^{+212.9}_{-180.2}$	$7.09^{+0.14}_{-0.13}$
18.0 nm	$0.78^{+0.38}_{-0.25}$	$31.0^{+15.2}_{-10.0}$	$278.5^{+194.8}_{-158.2}$	$0.41^{+0.14}_{-0.13}$

In this work, the measured D corresponds to a mobility range from 31.0 $cm^2/V{\cdot}s$ (18.0 nm thick) to 388.5 $cm^2/V{\cdot}s$ (3.0 nm thick). Our measurement upper bound is larger than most of the reported work. We attribute this to the fact that our MoS_2 samples are unprocessed and unconstrained. Early electrical measurements have deduced motilities in the range of 100-260 $cm^2/V{\cdot}s$ for bulk MoS_2 crystals.[103]

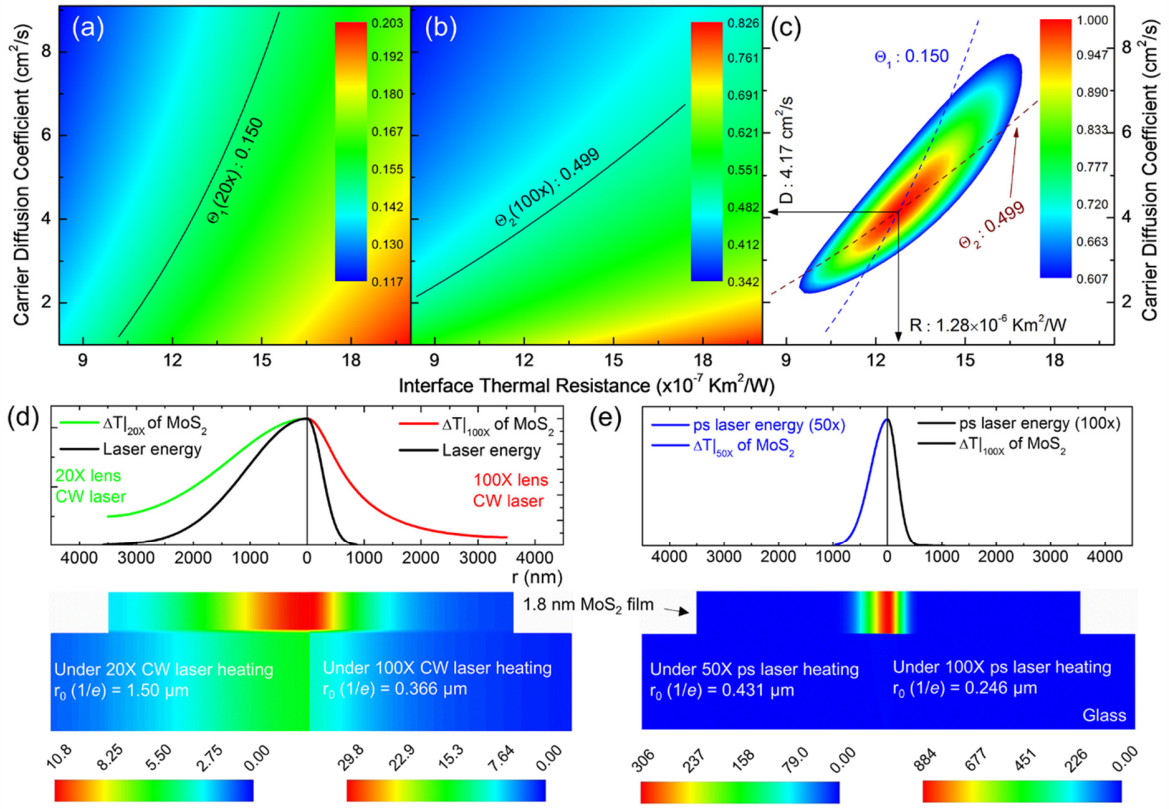

Figure 5.5 3D numerical modeling results for the 1.8 nm thick MoS_2 sample.

Moreover, the theoretical optical-phonon-scattering-limited mobility was reported up to 400 $cm^2/V \cdot s$ approached by adopting high-κ dielectric materials (*e.g.*, HfO_2, Al_2O_3) to build top-gated devices.[12,129,130,152] Furthermore, compared with the c-Si substrate (*p*-doped) as shown in last chapter, the insulator glass substrate used in this work could create better dielectric environment to enhance the dielectric screening of Coulomb potentials which could lead to enhanced carrier mobility especially for relatively thin MoS_2 samples.[53,132] Besides, compared to the air (dielectric constant is 1), MoS_2 has a much larger dielectric constant (~4).[153] As a result, for thicker MoS_2 samples, the upper part itself could also serve as the high dielectric environment (dielectric capping effect).[53]

5.3.3 MoS_2 Thickness Effect on *R* and *D*

In anticipation to find out the effect of MoS_2 thickness on *R* and *D*, we plot them as a function of MoS_2 thickness as shown in Fig. 5.6. For comparison, the *D* and *R* results from MoS_2 supported on c-Si substrate from last chapter are also plotted in these two figures. Table 5.1 also lists the entire results. For the hot carrier diffusivity *D*, as shown in Fig. 5.6(a), the 3.0 nm MoS_2 sample has the largest *D* value. Similar trends for this thickness-dependent carrier mobility are also reported before.[122,132] The inset of Fig. 5.6(a) shows the carrier mobility results from Lin *et al.*'s work.[122] They attribute this to the effect from metal source/drain contacts, and only the top MoS_2 layer could be connected to the contacts.[154] With decreased sample thickness, the absence of sufficient screening of the substrate results in a lower mobility. However, when the thickness is becoming smaller, the finite interlayer conductivity (in a resistor network model) could result in an effective higher total mobility.[154] The competition of these two physics accounts for a maximum mobility value at a certain layer thickness.[133] For our optically generated hot carrier transport, the resistor network model does not apply here. Instead, we have following explanations for this nonmonotonic relationship between sample thickness and hot carrier diffusivity. For thin samples (1.8 nm and 3.0 nm thick), with the increase of film thickness, the effect of the charge impurities will be reduced and the screening of substrate increases, both leading to carrier transport boost.[133] During the sample transfer process, contamination of the sample cannot be avoided. Such contamination includes charged impurities and defects such as absorbed or trapped oxygen and water, residue from Gel film or Scotch tape, or trapped ions and substrate defects.[155] All these could significantly contribute to disorders and degrade the hot carrier transport. For thicker samples,

as shown in the sample AFM characterization results from Section 5.1, the white dots in the AFM images could be the high points or the Gel film residues, especially for the thick samples (>7.8 nm thick). The loose contact caused by the high points of the substrate could weaken the substrate dielectric screening and restrict the carrier transport. This also accounts for the fact that, as shown in Fig. 5.6(a), the *D* for thicker MoS_2 samples are almost at the same level for both glass and c-Si substrates. However, the measured *D* in this work is relatively lower. As discussed in sample preparation in Section 5.1, the hydrophilic glass dielectric surface could introduce more water molecules to thicker MoS_2 nanosheets samples. These water molecules-induced electronic traps could also affect the charge transfer, leading to a decreased carrier diffusivity.[156] Besides, for the maximum *D* value (3.0 nm thick MoS_2), additional discussion could also be found in next section.

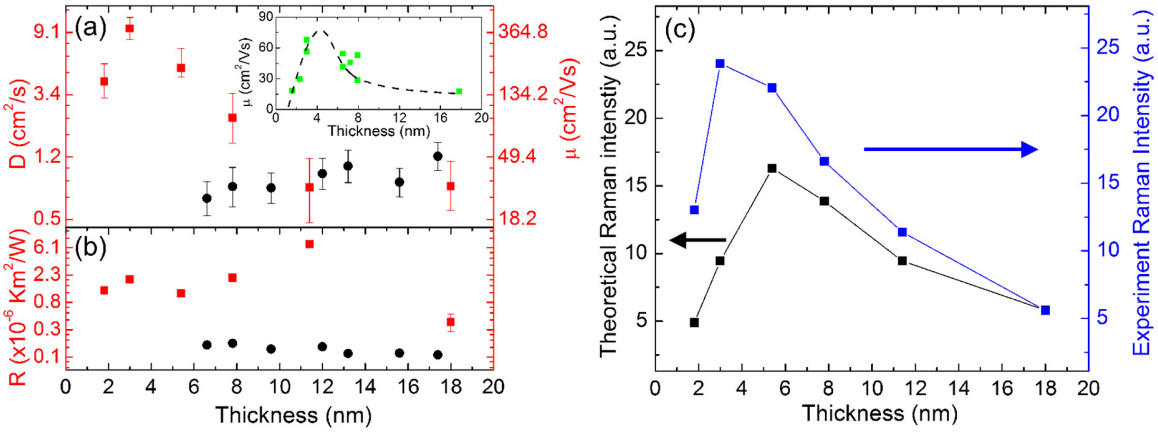

Figure 5.6 Hot carrier diffusivity, interface thermal resistance versus sample thickness of six MoS_2 samples on glass substrate (the red plots). The theoretical Raman intensity study results.

For the interface thermal resistance as shown in Fig. 5.6 (b), we obtain here is in the order of 2×10^{-6} K·m^2/W. They are much larger than what we found in previous work for c-Si supported MoS_2 nanosheets [dark dots in Fig. 5.6 (b)], such as the 6.6 nm MoS_2 has *R* as

1.75×10^{-7} K·m^2/W. On the one hand, the ET-Raman eliminates the errors from laser absorption evaluation and temperature coefficient calibration. Therefore, we do not need to consider those two factors. On another hand, as we mentioned in the introduction section, the glass substrate we used in this work is not polished as the c-Si substrate. So the MoS_2 nanosheets prepared from mechanical exfoliation onto glass substrate are actually supported by the high points from the substrate. This imperfect and loose interface contact could dramatically weaken the interface energy coupling.[32] Besides, as shown in Fig. 5.6 (b) and Fig. 5.1 (e), 11.4 nm thick MoS_2 sample has both the largest *R* value and largest lateral size. It is possible that the stress in the exfoliated MoS_2 sample is difficult to be released, especially for the sample with large lateral size. This kind of stress can also reduce the interface energy coupling. In this work, the dielectric substrate promotes great screening and simplifies the transfer of hot carriers. There are some concerns for the applicability of ET-Raman to study the hot carrier mobility of 2D MoS_2 supported on metal surface. With the metal as substrate, the Fermi level pinning (FLP) will occur at the interface which will make the Fermi level pinned closer to the conduction band in MoS_2. This Fermi level shift may form the covalent bonds between MoS_2 and the contact metal. As a result, most of the photo-generated charge carriers will diffuse into the metal substrate. Besides, many other complicated physical phenomena have to be taken into consideration while using metal substrate, such as the enhanced surface recombination, low substrate Coulomb screening, *etc*. In this case, ET-Raman will have great difficulty to study its effect by heating size variation.

5.3.4 Theoretical Raman Intensity Study

The theoretical Raman intensity of different samples could be evaluated by considering multiple reflections of both the incident laser beam and the Raman signal within the supported

MoS_2 nanosheets. The comparison of the theoretical Raman intensity F and the experiment Raman intensity is shown in Fig. 5.6 (c). As has been studied in our previous work, the Raman signal of the sample will be significantly enhanced if there is even a tiny spacing at the interface (MoS_2 supported on c-Si substrate). In the experiment, the 3 nm thick sample has the largest Raman intensity per unit laser power excitation. Moreover, we have tried to increase the interface spacing level (from 0 to hundreds of nanometers) and found that the theoretical Raman intensity was not very sensitive to the spacing (increased only less than 10%) for our samples. This shows that the spacing has very limited contribution to this Raman intensity enhancement.

Additionally, as shown in Fig. 5.6 (a) and (c), the theoretical Raman intensity has the same change trend to our D value versus sample thickness. This could be explained below. For MoS_2, it is experimentally considered to be an n-type semiconductor due to its sulfur vacancies.[157,158] This means that the donor (electron) concentration is larger but it may vary from sample-to-sample. This difference gives MoS_2 slightly different Fermi energy levels and the Fermi energy increases (shifts to conduction band) with increased electron concentration. Besides, because the electron-phonon scattering rate and Fermi energy have a positive correlation, the Raman intensity is inversely proportional to Fermi energy.[159,160] In the Raman laser heating process, the 3.0 nm thick sample has the largest carrier diffusivity that can result in lower carrier concentration level at its excitation region due to the fast carrier diffusion. This will lead to a relatively lower Fermi energy level. So its local Raman intensity is enhanced and much larger than its theoretical intensity.

For the experimentally obtained Raman intensity, we use a 50× objective lens (NA=0.5) to collect the Raman signal for all six samples under the same laser energy level (2.5

mW before entering the sample) and same integration time (4 s). Moreover, we assume the normal incidence because of the backscattering geometry, the propagation direction of the incident and scattered light is perpendicular to the plane of the MoS_2. In addition, the laser beam is Gaussian and the focused laser beam hits the sample surface at the beam waist which provides the normal incidence of the laser beam in the sample.[91,159] For our MoS_2 samples, the thickness is too small to consider the portion of the beam entering the sample at an oblique angle.

CHAPTER 6. FIVE-STATE PICOSECOND ET-RAMAN FOR MEASURING IN-PLANE THERMAL CONDUCTIVITY OF FEW-LAYERED MOS2 UNDER CONJUGATION WITH HOT CARRIER AND INTERFACE PHONE TRANSPORT

During the ET-Raman study for interface thermal resistance of FL MoS_2 and its substrate, the in-plane thermal conductivity value was refered from other's work. This could not suit our case and may introduce uncertainty for our interface energy transport study. In this work, we introduce a technique to determine k of FL MoS_2 by designing different Raman laser heating states at both space and time domain: Five-State ET-Raman. This is simple and reliable and is more generally applicable than many existing methods. It can be used effectively to determine the k and also interface thermal resistance (R) and hot carrier diffusivity (D) simultaneously with high accuracy and confidence because it can successfully eliminate the errors brought by evaluations of laser energy absorption and Raman temperature calibration. Using the technique, we determined the k, D, and R of eight FL MoS_2 samples with a thickness ranging from 2.4 to 37.8 nm supported on a glass substrate. And a nonmonotonic thickness-dependent k trend is discovered and agrees well with others' work. It decreases from 60.3 W/m·K for 2.4 nm thick to 31.0 W/m·K for 9.2 nm thick, and increases to 76.2 W/m·K for 37.8 nm thick MoS_2.

In this chapter, I will first demonstrate the physical model of Five-State Picosecond ET-Raman technique in section 6.1. Then the experiment details including the sample preparation, experiment setup, and Raman experiment results in section 6.2. In section 6.3, I will show how we can simultaneously determine three important physical parameters in the 2D interface systems: D, R, and k. Additionally, especially for the thickness-dependent k, I will give some physical discussion for our findings.

6.1 Physical Principles of Five-State Picosecond ET-Raman Technique

In the Five-States Picosecond ET-Raman technique, we construct total five distinct energy transport states in both space and time domains, and probe the materials' thermal response to determine the in-plane thermal conductivity of MoS_2 with consideration of the effect of interface thermal transport and hot carrier diffusion. Fig. 6.1 shows the physical principles of this technique. Similar to the ET-Raman technique, a laser with 532 nm irradiates the 2D MoS_2 sample for both laser heating and Raman probe. In a big picture, the absorbed laser energy will be transported from two effects: in-plane hot carrier diffusion and two directions (both in-plane and out-of-plane down to the substrate) phonon transport. For in-plane direction, both hot carrier diffusion (hot carrier diffusivity) and phonon transport (thermal conductivity) contribute to the thermal energy transport. From the hot carrier diffusion process, thermal energy from this thermalization process will dissipate out to the lower temperature area. The heat transfer rate (q) could be considered as the circular fin situation as $q = 2\pi k r_0 t \Delta T m \frac{K_1(mr_0)I_1(mr_1) - I_1(mr_0)K_1(mr_1)}{K_0(mr_0)I_1(mr_1) + I_0(mr_0)K_1(mr_1)}$, where k, t, and r_1 is the in-plane thermal conductivity, the thickness, and lateral size (radius) of 2D material, r_0 is the radius of laser heating spot, $m=(k \cdot t \cdot R)^{-1}$ and R is the interface thermal resistance between 2D material and its substrate. We can describe the heat transfer rate by hot carriers as $q = (\partial N / \partial r) 2\pi r_0 D t E_g$, where $\Delta N(r,t)$ (cm^{-3}) is hot carrier concentration, D (cm^2/s) is hot carrier diffusivity, E_g is the bandgap of 2D material. As we can see, the thermal energy transport by phonon and hot carrier follow different rules as a function of laser heat spot size so that we could differentiate the effect of D, k, R by designing steady state heating with different laser heating sizes. By this

technique to measure the *k* of MoS_2, not only can we will consider the effect from *D* and *R* on thermal energy transport, but we also could determine the *D* and *R* values.

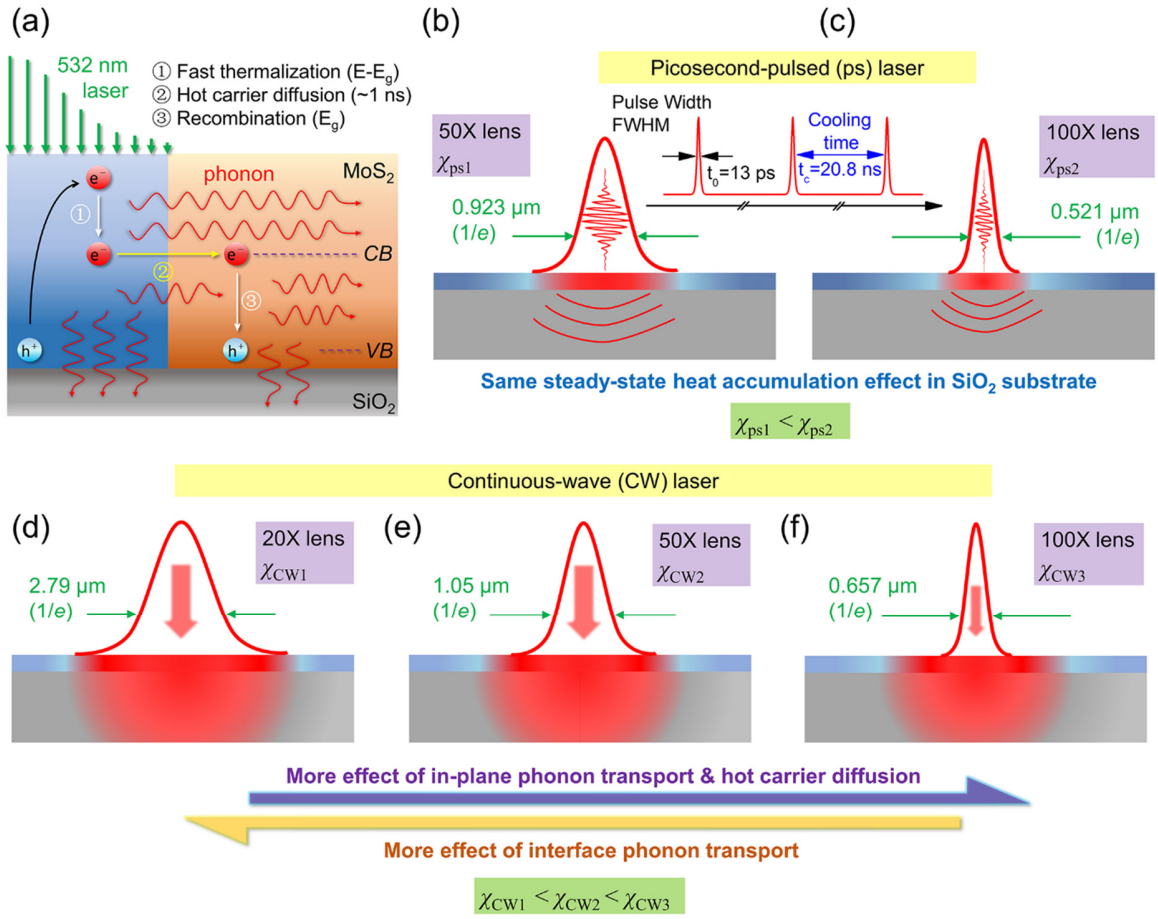

Figure 6.1 The physical principle of Five-State Picosecond ET-Raman.

Specifically, in our technique, we have three sub-states in steady-state heating and two sub-states in picosecond heating. In the steady-state heating, three sub-states come with different laser heating sizes. As shown in Fig. 6.1 (d) - (f), we use a CW laser source to generate steady-state heating to study the temperature profile with strong (*R*, *k*, *D*) effect from Raman signal. Moreover, by using different objectives (20×, 50×, and 100×) to have the size variation, we could differentiate the effect of *R, D*, and *k*. In Fig. 6.1 (a), the laser heating spot under a

20× (NA=0.4) objective has a diameter around 2.79 μm (1/*e* peak value). Since the MoS_2 nanosheets will absorb the laser energy, they will conduct the absorbed energy directly to substrate via *R* and to the in-plane direction then to the substrate via the interface (effects of *R, D*, and *k*). At the same time of laser heating, the same laser beam also excites Raman signal by which we could get the temperature profile of the sample. The determined RSC: $\chi_{CW1}=\partial\omega/\partial P$ will be affected by *R*, *D*, and *k*, laser absorption coefficient, and temperature coefficient of Raman shift. Then, as shown in Fig. 6.1 (e) and (f), we reduce the laser heating dimension to much smaller levels by a 50× (NA=0.5) objective (1.05 μm) and a 100× (NA=0.8) objective (0.657 μm). Then we also obtain RSC from corresponding experiments as χ_{CW2} and χ_{CW3}. RSC increases with smaller heating size ($\chi_{CW1} < \chi_{CW2} < \chi_{CW3}$) due to its larger energy density. Besides, when the heating spot size decreases, the *D* and *k* of the 2D material will have more influence on the measured temperature, and *R* will have less effect. Ideally, when the laser heating spot size is even larger than 2D material, the measured temperature rise will be dominated by the interface property (*R*). Therefore, these three steady states construction could differentiate the effect of *k*, *D,* and *R* in the measured RSC by Raman spectroscopy.

Another two sub-states in picosecond laser heating are opposite to the steady-state: it has zero-transport. As shown in Fig. 6.1 (b) and (c), we apply the ps laser under 50× (NA=0.5, 0.92 μm) and 100× (NA=0.8, 0.52 μm) objectives. Similarly, we obtain RSC under both 50× and 100× objectives as χ_{ps1} and χ_{ps2}, respectively. We could use these zero-transport states (ps laser heating) to distinguish the roles of ρc_p and (*R*, *k*, *D*) with a negligible contribution of *R, k,* and *D* to the temperature rise.

Based on the determined RSC values from the steady-state and zero-transport heating experiments, we define the dimensionless normalized RSC as $\Theta_1= \chi_{CW1}/(\chi_{ps2}-\chi_{ps1})$, $\Theta_2=$

$\chi_{CW2}/(\chi_{ps2}-\chi_{ps1})$, and $\Theta_3=\chi_{CW3}/(\chi_{ps2}-\chi_{ps1})$. Moreover, this normalized RSC completely rules out the effects of laser absorption, Raman temperature coefficients, and the pulse accumulation effect. Θ is only a function of the 2D material and substrate materials' ρc_p, R, k, and D. Through a 3D heat conduction model to include all these properties, we could finally determine 2D material's R, k, and D simultaneously.

6.2 Five-State Picosecond ET-Raman Experiment Details

6.2.1 Sample preparation and characterization

We prepare eight few-layered supported MoS_2 samples by micromechanical cleavage technique. The lateral size of layered MoS_2 nanosheets has an equivalent radius ranging from 7.5 to 13 μm.

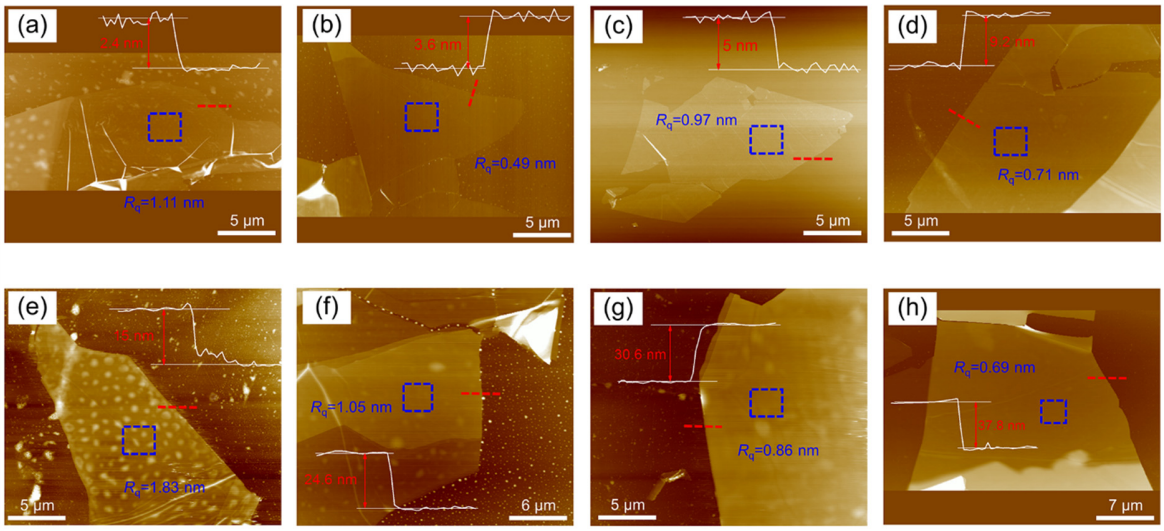

Figure 6.2 AFM measurement results of eight FL MoS_2 sample on glass substrate.

As illustrated in Figure 6.2, the samples have a thickness of around 2.4, 3.6, 5.0, 9.2, 15.0, 24.6, 30.6 and 37.8 nm, respectively. The blue dashed square shows the area where the laser is focused during different Raman experiments. We also evaluate the sample surface

roughness. For example, the 2.4 nm thick sample has a root-mean-square (RMS) roughness (R_q) of 1.11 nm. R_q varies for different samples. Larger R_q indicates possible wrinkles or ripples. For reference, the substrate (glass) surface has a R_q (glass) around 1.6 nm.

6.2.2 Five-State ET-Raman experiment setup

As shown in Fig. 6.3, similarly, the Raman experiments are performed by using a confocal Raman system that consists of a Raman spectrometer. The 532 nm CW laser or ps laser is introduced to the Raman system. Three different objective lenses are used for steady-state heating, and two different objective lenses are used for ps laser heating.

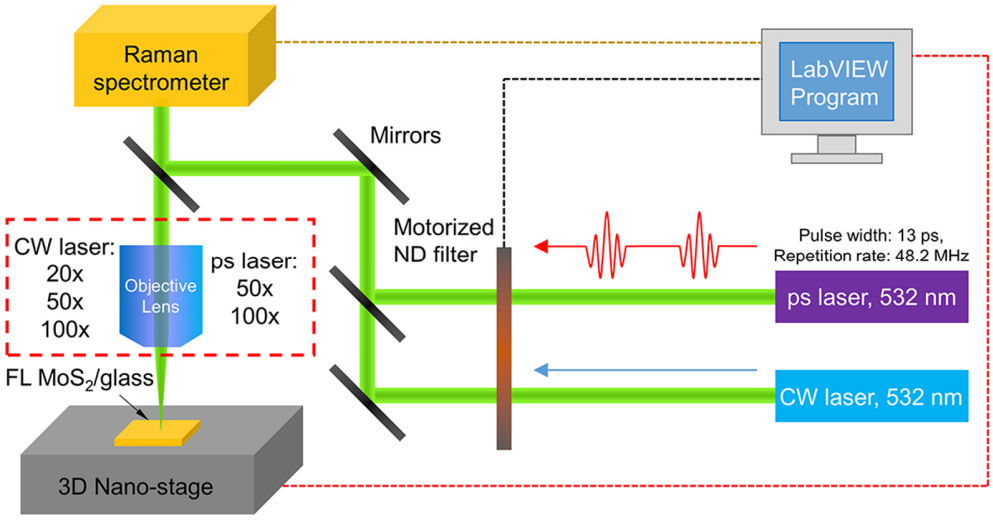

Figure 6.3 Schematic of Five-State Picosecond ET-Raman experiment setup.

6.2.3 Thermal response of MoS_2 under CW and picosecond-pulsed laser heating

In the Raman experiments, as shown in Fig. 6.4(a)-(e), the laser heating size is determined by the spatial energy distribution for each heating state. Take 20× objective with CW laser for example, as shown in Fig. 6.4 (a), the false color map data is from the image captured by the CCD camera. The corresponding laser spot size (at e^{-1}) is determined as 1.40 μm. Taking the 2.4 nm thick MoS_2 sample for example, a typical Raman spectrum of MoS_2

under different heating states is shown in the first sub-figure [e.g., Fig. 6.4 (a-1)]. The RSC value for five different heating states are obtained by the linear fitting.

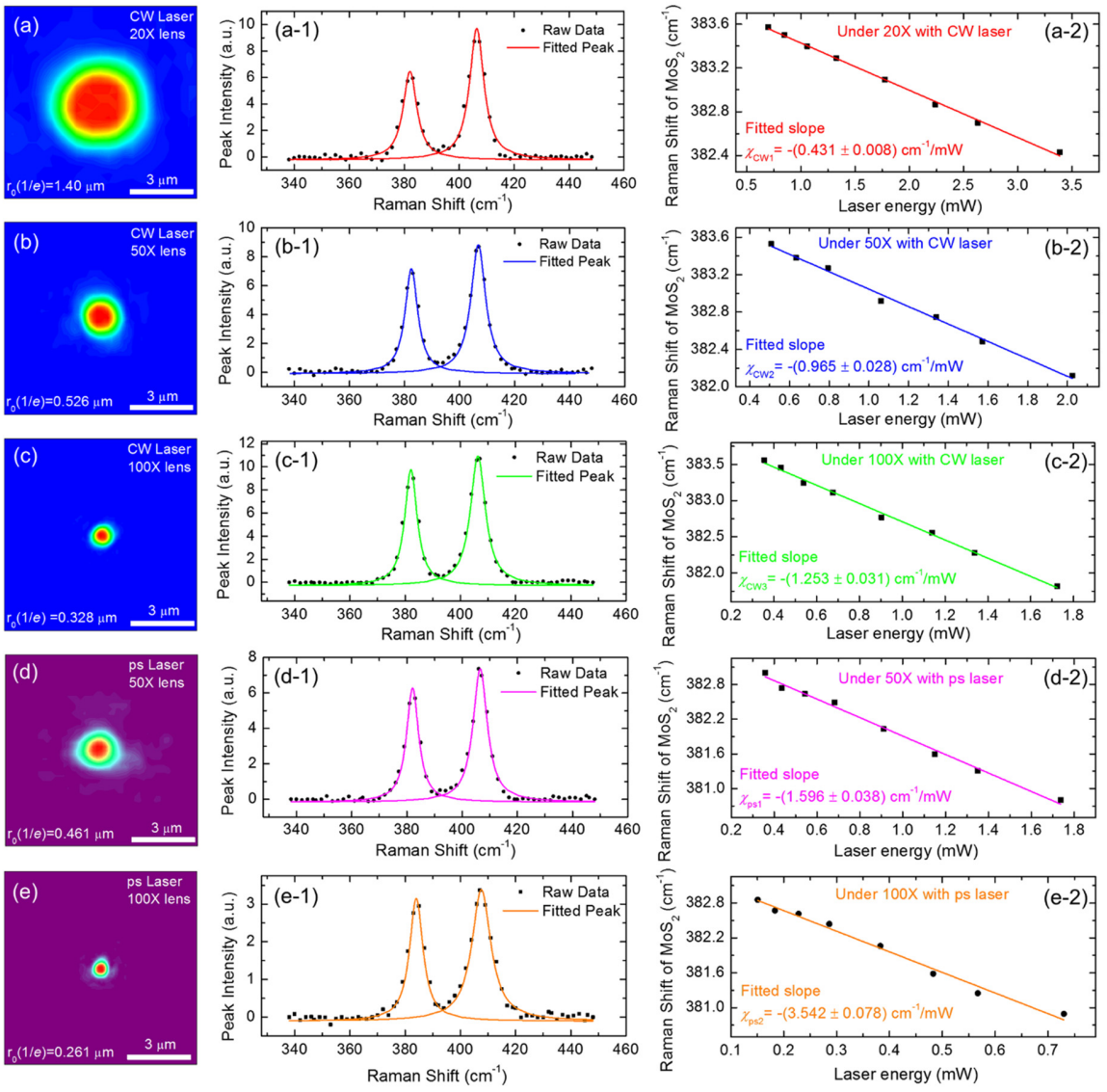

Figure 6.4 Spatial focused laser energy distribution false-color map of five heating states. The typical Raman spectrum and the linear fitting result (RSC) of 2.4 nm thick MoS_2 nanosheets at different heating states. The solid curve and line are the fitted results.

By CW laser, as shown in Fig. 6.4 (a-2), (b-2) and (c-2), the linear fitting results RSC of MoS_2 E^1_{2g} mode under 20× objective is –(0.431±0.008) cm^{-1}/mW, under 50× objective is –

(0.965±0.028) cm^{-1}/mW, and under 100× objective is –(1.253±0.031) cm^{-1}/mW. By ps laser under 50× and 100× objectives, as shown in Fig. 6.4 (d-2) and (e-2), the RSC values of MoS_2 E^1_{2g} mode are –(1.596±0.038) cm^{-1}/mW and –(3.542±0.078) cm^{-1}/mW, respectively. Based on the RSC values from five heating states, we obtain the normalized RSC as Θ_{exp_1} = Θ_{exp_2} = 0.496±0.019, and Θ_{exp_3} = 0.644±0.026.

6.3 Simultaneous determination of *k*, *D,* and *R*

Then, as demonstrated in Chapter 4, we conduct the 3D numerical modeling calculate the temperature rise to determine the in-plane thermal conductivity (*k*), hot carrier diffusivity (*D*) and the interface thermal resistance (*R*). Take the 2.4 nm thick MoS_2 for example, from the 3D numerical simulation and Raman experiment, we could calculate Θ_1, Θ_2 and Θ_3 for MoS_2 in the (*k*, *D*, *R*) space. Then, we use the normalized probability distribution function (Ω) to recalculate the (*k*, *D*, *R*) space data to determine the (*k*, *D*, *R*). $\Omega_i = \exp\left[-(\Theta_i - \Theta_{exp\_i})^2 / (2\sigma_i^2)\right]$ (i = 1, 2, and 3) with Θ_i and Θ_{exp_i} are normalized RSC value from 3D modeling and experiment, respectively. σ_i is the experimental uncertainty. In the (*k*, *D*, *R*) space, we define a composite probability distribution function as $\Omega(k, D, R) = \Omega_1 \cdot \Omega_2 \cdot \Omega_3$. The position in the (*k*, *D*, *R*) space of $\Omega(k, D, R) = 1.0$ represents the corresponding (*k*, *D*, *R*) results for this sample. For the 2.4 nm thick sample, as shown in Figure 6.5 (a), the $\Omega(k, D, R) \geq 0.65$ in the (*k*, *D*, *R*) space gives a (*k*, *D*, *R*) range. In this space range, we are more than 65% confident that the final (*k*, *D*, *R*) result is inside. When we increase the confidence level from 0.65 to 0.80 to 0.95, and to 1.0, as shown in Fig. 6.5 (b)-(d), the (*k*, *D*, *R*) space range gets smaller and smaller. As a result, in Fig. 6.5(d), there will be only one point (k_0, D_0, R_0) in the space that could give us Ω(60.3 W/m·K, 7.92 cm^2/s, 1.82×10^{-6} K·m^2/W)=1.0.

So we could have the simultaneous determination of k, D, and R as $k_0 = 60.3$W/m·K, $D_0 = 7.92$ cm^2/s, and $R_0 = 1.82\times10^{-6}$ K·m^2/W.

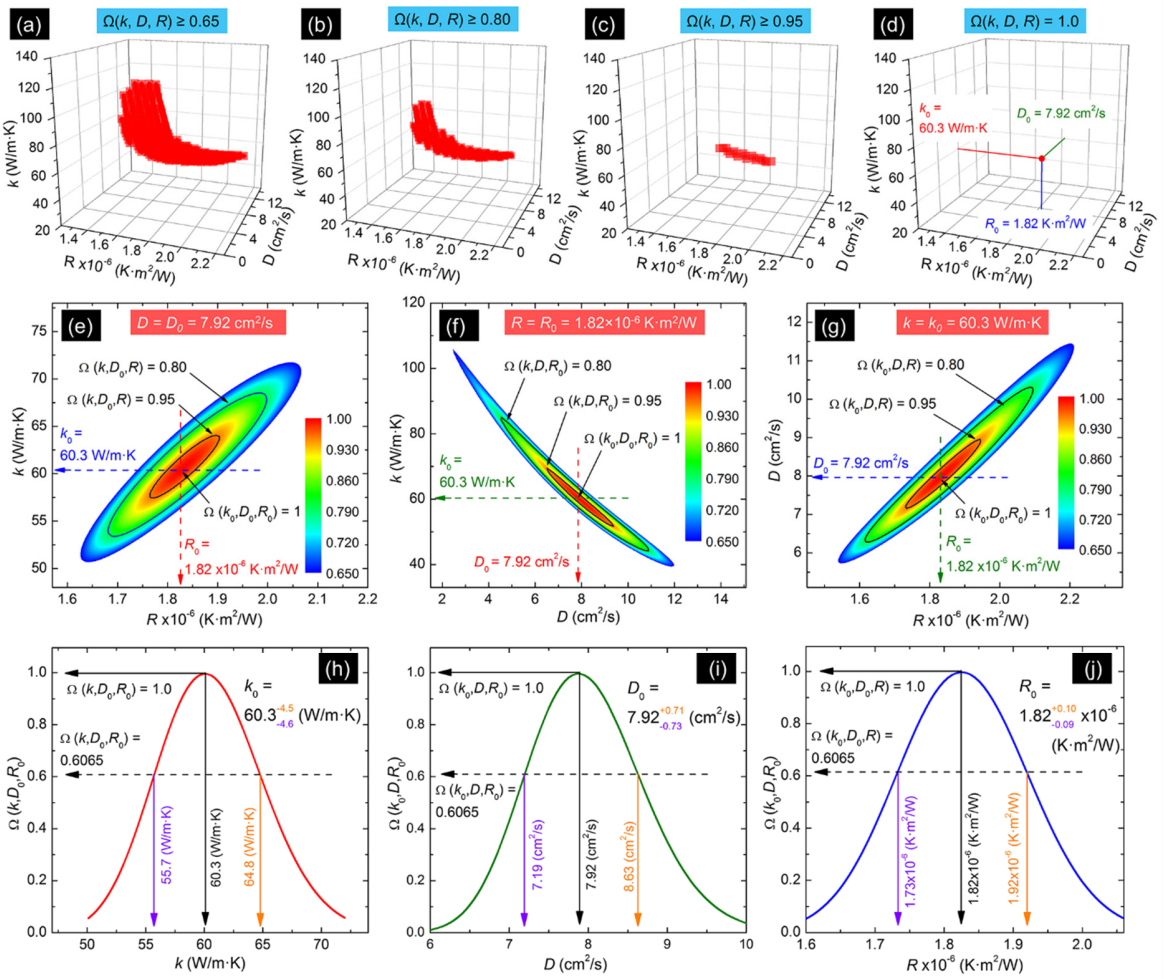

Figure 6.5 Simultaneous determination of k, D, R of 2.4 nm thick MoS_2 sample.

Fig. 6.5 (e)-(g) show the cross-section views of Fig. 6.5 (a) which are the color contours of the different confidence levels. All those three cross-section planes go through the point of $\Omega(k, D, R) = 1$ in the (k, D, R) space. Fig. 6.5 (e) represents the 2D $\Omega(k, D, R)$ contour in (k, R) space with $D = D_0 = 7.92$ cm^2/s. Two dash lines through point $\Omega(k, D_0, R) = 1.0$ also give the k and R determination. Also, by extracting the data from dash lines, as shown in Fig. 6.5(h)-

(j), we could have a 1D plot of $\Omega(k, D, R)$ against k, D, and R, respectively. The red 1D plot in Fig. 6.5(h) corresponds to the red dash lines in Fig. 6.5(e) and (f). Another two 1D plots in Fig. 6.5(i) and (j) correspond to the green and blue dash lines in Fig. 6.5(e)-(g), respectively. To show the final results with uncertainty, we use the value of $\Omega(k, D, R) = 0.6065$ corresponding to the σ confidence to find the final results range. From Fig. 6.5 (h)-(j), we have the deduced k_0 as $60.3^{+4.5}_{-4.6}$ W/m·K, D_0 as $7.92^{+0.71}_{-0.73}$ cm^2/s, and R_0 as $1.82^{+0.10}_{-0.09} \times 10^{-6}$ K·m^2/W. Also, Also, the final results and the uncertainty for all eight samples are summarized in Table 6.1 and also plotted in Fig. 6.6 (a)-(c). Note that all uncertainties come from the RSC fitting procedure and we do not include systematic errors from the uncertainty of P, r_0 and NA.

Table 6.1 The summary of the thermal conductivity (k), hot carrier diffusivity (D), and the calculated the interface thermal resistance (R) of eight MoS_2 samples.

Sample Thickness	Layer Number	k (W/m·K)	D (cm^2/s)	R (10^{-6} K·m^2/W)
2.4 nm	4	$60.3^{+4.4}_{-4.7}$	$7.92^{+0.74}_{-0.82}$	$1.82^{+0.10}_{-0.09}$
3.6 nm	6	$46.0^{+4.3}_{-4.2}$	$10.3^{+1.13}_{-1.05}$	$0.602^{+0.047}_{-0.046}$
5.0 nm	8	$35.1^{+3.3}_{-3.2}$	$10.2^{+1.22}_{-1.23}$	$0.798^{+0.061}_{-0.060}$
9.2 nm	15	$31.0^{+2.8}_{-2.7}$	$8.49^{+1.11}_{-1.02}$	$0.402^{+0.042}_{-0.041}$
15.0 nm	25	$51.0^{+2.1}_{-2.1}$	$10.2^{+1.04}_{-0.96}$	$0.480^{+0.049}_{-0.049}$
24.6 nm	41	$52.4^{+2.3}_{-2.1}$	$7.63^{+1.12}_{-1.06}$	$1.07^{+0.12}_{-0.12}$
30.6 nm	51	$62.9^{+2.2}_{-2.2}$	$6.45^{+0.93}_{-0.91}$	$0.938^{+0.120}_{-0.120}$
37.8 nm	63	$76.2^{+2.5}_{-2.5}$	$6.22^{+0.96}_{-0.88}$	$0.482^{+0.103}_{-0.099}$

6.4 Results and Discussion

6.4.1 Thickness-Dependent In-plane Thermal Conductivity of FL MoS_2

In Fig. 6.6 (a), we show the in-plane thermal conductivity of eight 2D FL MoS_2 samples at room temperature as a function of the thickness (number of layers). We also insert the recent

measurement results for comparison.[64,65,71-75] The different values from different works of thermal conductivity could be attributed to the difference from samples quality and measurement methods.

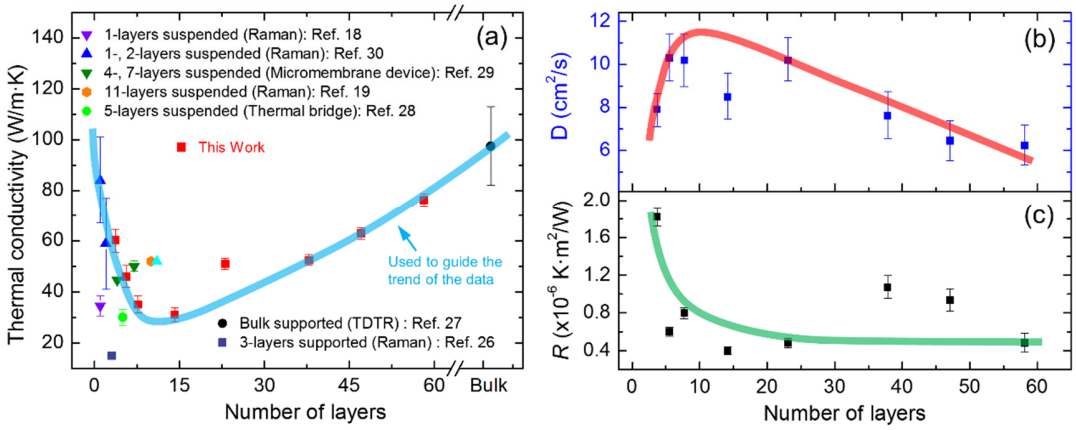

Figure 6.6 Summary of the room temperature in-plane thermal conductivity of MoS_2 as a function of layer number for this work (dark squares) and other experimentally obtained results. Hot carrier diffusivity (D) and interface thermal resistance (R) of eight MoS_2 samples. The blue, red, and green curves are used to visually guide the trend of the data.

However, the nonmonotonic thickness-dependent k trend guided by a light blue curve with the nadir at around 6.6 nm thick (10 layers) found in this work agrees well with others' results. This dependence could be rationalized as follows. On the one hand, as shown in Fig. 6.2, we could find some white dots in the AFM images which are potentially the Gel film residues, especially for 15 nm thick sample. This possible presence of Gel film residue and/or native oxide could cause surface disorders resulting in diffuse phonon-surface (boundary) scattering, this effect will be less pronounced for thicker samples which will lead to higher in-plane thermal conductivity. This trend of thermal conductivity with thickness has been also demonstrated and explained in regular films and other 2D materials.[161] However, this fails to explain our data in Fig. 6(a). On the other hand, for the thin MoS_2 samples (< 10 layers) as

studied by first-principles calculations by Gu *et al*.,[162] the thermal conductivity reduction from single layer to few-layer is accounted by the change of phonon dispersion and the enhanced phonon scattering strength for thicker samples. The changes in the phonon dispersion with increasing layer numbers will result in lower group velocity which could greatly decrease the thermal conductivity. Specially, similar to graphene from single layer to few-layer, the mirror symmetry is missing which changes the anharmonic force constant leading to stronger phonon scattering and thermal conductivity reduction.[163]

6.4.2 Effect of MoS_2 Thickness On *R* and *D*

Figure 6.6 (b)(c) show how *R* and *D* values change with MoS_2 thickness.The detailed results are also summarized in Table 6.1. Especially, *D* has a relatively higher uncertainty than both *k* and *R*. As explained in last three chapters, the hot carrier diffusivity is studied by its effect on thermal energy distribution. Ideally, if we could generate extreme heating states, the uncertainty of *D* could be strongly reduced. Fig. 6.6 (b) presents the nonmonotonic thickness dependent carrier diffusivity *D*. Similar trend has been found as shown in last chapter, we attributed this to the reduced charge impurities for thin samples and loose contact with the substrate or possible wet substrate surface for thicker samples.

The interface thermal resistance *R* for eight samples are in the order of 1.0×10^{-6} $K\cdot m^2/W$ and decrease with increasing layer number. We have studied the thickness dependent interface thermal energy transport, the thicker sample with better stuffiness could help to form better contact with the substrate.[68] Also, the glass substrate used in this work is not polished so that the FL MoS_2 sample may be possibly supported by the high points from the substrate. This is the reason why the *R* is larger than that with the polished silicon substrate.

CHAPTER 7. CONCLUSION AND FUTURE WORK

7.1 Conclusion

7.1.1 Conclusion on Interfacial Thermal Conductance between few to tens of layered MoS_2 and c-Si (effect of MoS_2 thickness)

In this work, we measured the interfacial thermal conductance (G) between few to tens of layered MoS_2 and c-Si substrate. For each sample, to get its G, sample preparation, thickness measurement and experiments of interface thermal conductance and temperature calibration were performed. It was found G increased with increasing layers of MoS_2 from approximately 0.974 $MWm^{-2}K^{-1}$ for 7 layers to 68.6 $MWm^{-2}K^{-1}$ for around 75 layers at room temperature. This close-to-two order of magnitude change in G reflected the interface spacing change versus the MoS_2 thickness. To better identify the morphology of MoS_2/c-Si interface, the interference enhancement of Raman signal of MoS_2 nanosheets was studied to confirm the spacing variation. The experimental Raman intensity was significantly higher than that of tight MoS_2-Si contact, uncovering the strong interface optical interference and the local spacing. To further understand the experimental results, we have conducted MD simulations to calculate the interface thermal conductance between MoS_2 and c-Si. It showed that thicker samples have a higher G, similar to the experimental observation. This could be explained by the improved mechanical stiffness of thicker samples and the resulting better interface contact. For the all the three samples under study (7, 8, and 13 layered), their G shows a decreasing trend against the local temperature. This was explained by the reduced phonon specific heat against decreased temperature. The calculated G agreed well with the upper bound G observed in our experiment, indicating when MoS_2 is thick (tens of nm), the local interface is close to the ideal scenario determined by local van der Waals bonding.

7.1.2 Conclusion on Hot Carrier Diffusivity and Interface Thermal Resistance of sub-10 nm MoS_2

We have developed a novel technology for the determination of both hot carrier diffusivity (D) and the interface thermal resistance (R) of sub-10 nm virgin mechanically exfoliated MoS_2 nanosheets on the c-Si substrate. The hot carrier effect on heat conduction by photon excitation, diffusion, and recombination could significantly extend the heating area size, especially when the laser focal spot size is comparable to the hot carrier diffusion length. The laser focal spot size was varied from 0.294 μm to 1.14 μm to change its effect in heat conduction, and the resulting temperature rise was measured by Raman spectroscopy. For our four sub-10 nm MoS_2 samples (3.6, 5.4, 8.4 and 9.0 nm), their hot carrier diffusivity was measured as $1.18^{+0.30}_{-0.23}$, $1.07^{+0.37}_{-0.26}$, $1.20^{+0.34}_{-0.27}$, and $1.62^{+0.30}_{-0.23}$ cm^2/s under the 1 ns hot carrier lifetime. Little thickness effect on hot carrier diffusion was observed. In fact, the technology can firmly determine the hot carrier diffusion length without knowledge of the lifetime. The four samples' hot carrier diffusion length was determined as $0.344^{+0.041}_{-0.036}$ (3.6 nm), $0.327^{+0.052}_{-0.043}$ (5.4 nm), $0.346^{+0.046}_{-0.042}$ (8.4 nm), and $0.402^{+0.036}_{-0.030}$ μm (9.0 nm). The hot carrier diffusivity study is conducted without applying an electric field or electrical contacts so the results could reflect the intrinsic properties of virgin 2D materials. We believe this non-contact and non-invasive technique could also be used for carrier transport and interface energy coupling study of other 2D materials. There have been only a few reports regarding the hot carrier transport study for MoS_2 nanosheets or the methods to exclude the potential influence on the transport measurement caused by the electrode. Also the results point out that for photon-excitation based energy transport study in 2D materials, the hot carrier diffusion could play a big role in

affecting the results, especially when the excitation size is comparable to the hot carrier diffusion length.

7.1.3 Conclusion on ET-Raman for Probing Interface Energy Transport and Hot Carrier Diffusion in few-layered MoS_2

As exemplified by studying the hot carrier diffusivity (D) and the interface thermal resistance (R) of mechanically exfoliated MoS_2 nanosheets on the c-Si substrate, we demonstrate a novel technique: ET-Raman without evaluation of light absorption or absolute temperature rise of MoS_2. The hot carrier effect on heat conduction could significantly extend the heating area, especially when the laser heating size is comparable to the hot carrier diffusion length. The laser focal spot size was varied from 0.294 μm to 1.14 μm to change hot carrier effect in heat conduction, and the resulting temperature rise effect was measured by power differential of Raman shift. Instead of only using continuous laser, a picosecond pulsed laser was also applied to heat and excite the Raman signal. By studying MoS_2 and the substrate's thermal response under different laser heating states, D and R were determined without knowing the laser absorption or the temperature coefficients of MoS_2. This development successfully eliminates the weak points of currently widely used Raman-based thermal characterization techniques. For our seven MoS_2 samples, under the 1 ns hot carrier lifetime, their hot carrier diffusivity was measured in the order of 1.0 cm^2/s which corresponds to a diffusion length in the order of 300 nm. D was observed to increase with the MoS_2 thickness. This strong dependence may be attributed to weaker in-plane electron-phonon interaction for thicker samples, their enhanced screening of long-range disorder, and improved charge impurities mitigation. No electric field or electrical contacts applied on the sample during this technique assures that the results could reflect the intrinsic properties of 2D materials. R is

determined as 1.22~1.87×10^{-7} K·m^2/W, decreasing with the MoS_2 thickness. This could be caused by the reduced interface spacing increase under laser heating for thicker samples, and the increased stiffness of thicker samples. The local interface spacing is uncovered by comparing the theoretical Raman intensity and experimental data, and is correlated with the observed *R* variation. To our best knowledge, ET-Raman could also be used for carrier transport and interface energy coupling study of other 2D materials in the most applicable forms with high accuracy and confidence. Such an impactful state-resolved technique opens up a new way for efficient and accurate 2D materials thermal and electrical properties characterization.

7.1.4 Conclusion on ET-Raman Application for FL MoS_2 on Glass Substrate

Taking advantage of ET-Raman technique without laser absorption and absolute temperature evaluation, we successfully determined the interface thermal resistance (*R*) and hot carrier diffusivity (*D*) of six mechanically exfoliated MoS_2 nanosheets supported on glass substrate. The sample thickness spanned over one order: 1.8~18 nm. This special structure provides one-side normal-*k* dielectric screening and very little material damage that would occur by top dielectric material coating in traditional mobility measurement. Compared with highly polished c-Si substrate, the glass substrate induced a quite high interface thermal resistance: 0.41~7.09 ×10^{-6} K·m^2/W, about one order of magnitude higher than that of MoS_2/c-Si interface. The determined *D* value spans from 0.76 to 9.7 cm^2/s, corresponding to a mobility range of 30.2~388.5 cm^2/V·s. A nonmonotonic thickness dependent *D* trend was discovered and was attributed to the possibly reduced charge impurities for thin samples and loose contact with the substrate or possible wet substrate surface for thicker samples. The very high hot carrier mobility will reduce the hot carrier concentration in the laser heating region in Raman

experiment, leading to a reduced electron-phonon scattering and boosted Raman intensity. This has been confirmed by our Raman intensity study and comparison against theoretical predictions.

7.1.5 Conclusion on Development of Five-State Picosecond ET-Raman Technique

In this work, we developed a novel Five-State Picosecond ET-Raman to measure the in-plane thermal conductivity (k) of nm-thick 2D materials. It does not need laser absorption and absolute temperature rise evaluation. By considering the effects of hot carrier diffusion and interface thermal energy transport, this technique was successfully applied to study eight 2D FL MoS_2 samples (2.4 nm to 37.8 nm thick) supported on glass substrate. Aside from the in-plane thermal conductivity, we can quantitatively determine the hot carrier diffusivity and interface thermal resistance simultaneously. We discovered a nonmonotonic thickness-dependent k trend. We attributed this to the possible surface phonon scattering, the change of phonon dispersion and enhanced phonon scattering strength. The measured k value spans from 31.0 to 76.2 W/m·K and is in good agreement with others'. This non-contact measurement uncovers the intrinsic properties of FL MoS_2. This technique could also be used for efficient and accurate thermal conductivity, carrier transport and interface energy coupling study of other 2D materials in the most applicable form with remarkable confidence. It will have a long-term impact on Raman-based thermal and electrical properties characterization of 2D materials.

7.2 Future Work

Based on the advantages of ET-Raman technique, it is good to focus on different transition metal dichalcogenides (TMDs), MX_2 (M=Mo, W, etc; X=S, Se, or Te). They are all semiconductor in nature and possess huge potential to be made into ultra-small and low power transistors that are more efficient than state-of-the-art silicon-based transistors.[164] Besides

sharing the similarities of a bandgap in the visible-near IR range, high carrier mobility, and on/off ratio with silicon, TMDs can be deposited onto flexible substrates and survive the stress and strain compliance of flexible supports.[165,166] Therefore, future work for continuation of research project has the following topics.

1. Investigate the effect of layered physical structure (lateral size, thickness, and defect) on the interface thermal transport and hot carrier diffusion. For real electronics applications, 2D materials with different thickness and lateral size could strongly affect the devices functionality. Besides, TMDs may contain many different structural defects in their crystal lattices which significantly influence their physico-chemical properties. Having structural defects can be either detrimental or beneficial, depending on the targeted application. For future work, for TMDs, we will focus on MX_2 (M=Mo, W; X=S, Se, or Te). By using the micromechanical cleavage technique, for each material, we will prepare 2D TMDs nanosheets samples for different thickness. The sample lateral size could be adjusted by focus ion beam in anticipation of exploring the size effect. Samples with the same thickness and lateral size would be first examined to identify the defects then study the defect effect.

2. Study the effect of substrate on both interface energy coupling and hot carrier diffusion. Different substrates could have different energy-coupling level with its upper 2D nanosheets to have different interface thermal conductance. Besides, different substrates could provide different dielectric environment which could strongly affect the hot carrier diffusivity of 2D TMDs. All these effects will be studied in the future work with quantitative understanding.

3. Explore the effect of temperature (70 K~850 K) on interface energy coupling and hot carrier diffusion. The operation temperature of electronics could vary a lot which may

significantly influence the device performance. 2D TMDs and its substrate could have different thermal expansion rate. With temperature change, the 2D material wrinkles could be flattened or become worse. These could strongly affect the interface energy coupling. Besides, the carrier diffusion will decrease when the temperature increases due to the increase of the carrier collision and braking. This temperature-related study will target these critical physics and provide in-depth and systematic understanding.

REFERENCES

1 Novoselov, K. S. *et al.* Electric field effect in atomically thin carbon films. *Science* **306**, 666-669 (2004).

2 Berger, C. *et al.* Ultrathin epitaxial graphite: 2D electron gas properties and a route toward graphene-based nanoelectronics. *The Journal of Physical Chemistry B* **108**, 19912-19916 (2004).

3 Bolotin, K. I. *et al.* Ultrahigh electron mobility in suspended graphene. *Solid State Commun.* **146**, 351-355 (2008).

4 Han, M. Y., Özyilmaz, B., Zhang, Y. & Kim, P. Energy band-gap engineering of graphene nanoribbons. *Phys. Rev. Lett.* **98**, 206805 (2007).

5 Wang, Q. H., Kalantar-Zadeh, K., Kis, A., Coleman, J. N. & Strano, M. S. Electronics and optoelectronics of two-dimensional transition metal dichalcogenides. *Nat. Nanotechnol.* **7**, 699-712 (2012).

6 Gaur, A. P. *et al.* Optical and vibrational studies of partially edge-terminated vertically aligned nanocrystalline MoS_2 thin films. *J. Phys. Chem. C* **117**, 26262-26268 (2013).

7 Huang, X. *et al.* Graphene-based materials: synthesis, characterization, properties, and applications. *Small* **7**, 1876-1902 (2011).

8 Wu, W. *et al.* Piezoelectricity of single-atomic-layer MoS_2 for energy conversion and piezotronics. *Nature* **514**, 470-474 (2014).

9 Novoselov, K. *et al.* Two-dimensional atomic crystals. *Proceedings of the National Academy of Sciences of the United States of America* **102**, 10451-10453 (2005).

10 Liu, K.-K. *et al.* Growth of large-area and highly crystalline MoS_2 thin layers on insulating substrates. *Nano Lett.* **12**, 1538-1544 (2012).

11 Coleman, J. N. *et al.* Two-dimensional nanosheets produced by liquid exfoliation of layered materials. *Science* **331**, 568-571 (2011).

12 Radisavljevic, B., Radenovic, A., Brivio, J., Giacometti, i. V. & Kis, A. Single-layer MoS_2 transistors. *Nat. Nanotechnol.* **6**, 147-150 (2011).

13 Radisavljevic, B., Whitwick, M. B. & Kis, A. Integrated circuits and logic operations based on single-layer MoS_2. *ACS nano* **5**, 9934-9938 (2011).

14 Mak, K. F., Lee, C., Hone, J., Shan, J. & Heinz, T. F. Atomically thin MoS_2: a new direct-gap semiconductor. *Phys. Rev. Lett.* **105**, 136805 (2010).

15 Yim, C. *et al.* Investigation of the optical properties of MoS_2 thin films using spectroscopic ellipsometry. *Appl. Phys. Lett.* **104**, 103114 (2014).

16 Lopez-Sanchez, O., Lembke, D., Kayci, M., Radenovic, A. & Kis, A. Ultrasensitive photodetectors based on monolayer MoS_2. *Nat. Nanotechnol.* **8**, 497-501 (2013).

17 Polman, A. & Atwater, H. A. Photonic design principles for ultrahigh-efficiency photovoltaics. *Nat. Mater.* **11**, 174-177 (2012).

18 Freitag, M. *et al.* Energy dissipation in graphene field-effect transistors. *Nano Lett.* **9**, 1883-1888 (2009).

19 Schulz, M. in *Power Conversion and Intelligent Motion Conference.*

20 Blazdell, P. Basics of Thermal Management Materials for Microelectronics–theory and practise.

21 Kapitza, P. The study of heat transfer in helium II. *J. Phys.(USSR)* **4**, 181-210 (1941).

22 Robertson, J. Interfaces and defects of high-K oxides on silicon. *Solid-State Electron.* **49**, 283-293 (2005).

23 Ziegler, A. *et al.* Interface structure and atomic bonding characteristics in silicon nitride ceramics. *Science* **306**, 1768-1770 (2004).

24 Hopkins, P. E. Thermal transport across solid interfaces with nanoscale imperfections: effects of roughness, disorder, dislocations, and bonding on thermal boundary conductance. *ISRN Mech. Eng.* **2013** (2013).

25 Stevens, R. J., Zhigilei, L. V. & Norris, P. M. Effects of temperature and disorder on thermal boundary conductance at solid–solid interfaces: Nonequilibrium molecular dynamics simulations. *Int. J. Heat Mass Transfer* **50**, 3977-3989 (2007).

26 Hopkins, P. E., Phinney, L. M., Serrano, J. R. & Beechem, T. E. in *2010 14th International Heat Transfer Conference.* 313-319 (American Society of Mechanical Engineers).

27 Casalegno, V. *et al.* Measurement of thermal properties of a ceramic/metal joint by laser flash method. *J. Nucl. Mater.* **407**, 83-87 (2010).

28 Pernot, G. *et al.* Precise control of thermal conductivity at the nanoscale through individual phonon-scattering barriers. *Nat. Mater.* **9**, 491-495 (2010).

29 Gundrum, B. C., Cahill, D. G. & Averback, R. S. Thermal conductance of metal-metal interfaces. *Phys. Rev. B* **72**, 245426 (2005).

30 Cahill, D. G., Goodson, K. & Majumdar, A. Thermometry and thermal transport in micro/nanoscale solid-state devices and structures. *J. Heat Transfer* **124**, 223-241 (2002).

31 Yue, Y., Zhang, J. & Wang, X. Micro/Nanoscale Spatial Resolution Temperature Probing for the Interfacial Thermal Characterization of Epitaxial Graphene on 4H-SiC. *Small* **7**, 3324-3333 (2011).

32 Tang, X., Xu, S., Zhang, J. & Wang, X. Five orders of magnitude reduction in energy coupling across corrugated graphene/substrate interfaces. *ACS Appl. Mater. Interfaces* **6**, 2809-2818 (2014).

33 Diao, J., Srivastava, D. & Menon, M. Molecular dynamics simulations of carbon nanotube/silicon interfacial thermal conductance. *The Journal of chemical physics* **128**, 164708 (2008).

34 Hu, M., Keblinski, P. & Schelling, P. K. Kapitza conductance of silicon–amorphous polyethylene interfaces by molecular dynamics simulations. *Phys. Rev. B* **79**, 104305 (2009).

35 Zhong, H. & Lukes, J. R. Interfacial thermal resistance between carbon nanotubes: molecular dynamics simulations and analytical thermal modeling. *Phys. Rev. B* **74**, 125403 (2006).

36 Zhang, J., Wang, Y. & Wang, X. Rough contact is not always bad for interfacial energy coupling. *Nanoscale* **5**, 11598-11603 (2013).

37 Prasher, R. Acoustic mismatch model for thermal contact resistance of van der Waals contacts. *Appl. Phys. Lett.* **94**, 1905 (2009).

38 Little, W. The transport of heat between dissimilar solids at low temperatures. *Can. J. Phys.* **37**, 334-349 (1959).

39 Reddy, P., Castelino, K. & Majumdar, A. Diffuse mismatch model of thermal boundary conductance using exact phonon dispersion. *Appl. Phys. Lett.* **87**, 211908 (2005).

40 Persson, B. & Ueba, H. Heat transfer between weakly coupled systems: Graphene on a-SiO_2. *EPL (Europhysics Letters)* **91**, 56001 (2010).

41 Cai, W. *et al.* Thermal transport in suspended and supported monolayer graphene grown by chemical vapor deposition. *Nano Lett.* **10**, 1645-1651 (2010).

42 Mak, K. F., Lui, C. H. & Heinz, T. F. Measurement of the thermal conductance of the graphene/SiO_2 interface. *Appl. Phys. Lett.* **97**, 221904 (2010).

43 Chen, Z., Jang, W., Bao, W., Lau, C. & Dames, C. Thermal contact resistance between graphene and silicon dioxide. *Appl. Phys. Lett.* **95**, 161910 (2009).

44 Taube, A., Judek, J., Łapińska, A. & Zdrojek, M. Temperature-dependent thermal properties of supported MoS_2 monolayers. *ACS Appl. Mater. Interfaces* **7**, 5061-5065 (2015).

45 Leblebici, Y. & Kang, S.-M. S. *Hot-carrier reliability of MOS VLSI circuits*. Vol. 227 (Springer Science & Business Media, 2012).

46 Lang, Z. *et al.* Phonon-limited electron mobility in single-layer MoS_2. *Chinese Physics Letters* **31**, 027301 (2014).

47 Kim, S. *et al.* High-mobility and low-power thin-film transistors based on multilayer MoS_2 crystals. *Nat. Commun.* **3**, 1011 (2012).

48 Lin, H., Xu, S., Zhang, Y.-Q. & Wang, X. Electron Transport and Bulk-like Behavior of Wiedemann–Franz Law for Sub-7 nm Thin Iridium Films on Silkworm Silk. *ACS Appl. Mater. Interfaces* **6**, 11341-11347 (2014).

49 Song, J. C., Rudner, M. S., Marcus, C. M. & Levitov, L. S. Hot carrier transport and photocurrent response in graphene. *Nano Lett.* **11**, 4688-4692 (2011).

50 Bonaccorso, F., Sun, Z., Hasan, T. & Ferrari, A. Graphene photonics and optoelectronics. *Nature photonics* **4**, 611-622 (2010).

51 Ruzicka, B. A. *et al.* Hot carrier diffusion in graphene. *Phys. Rev. B* **82**, 195414 (2010).

52 Strait, J. H., Nene, P. & Rana, F. High intrinsic mobility and ultrafast carrier dynamics in multilayer metal-dichalcogenide MoS_2. *Phys. Rev. B* **90**, 245402 (2014).

53 Bao, W., Cai, X., Kim, D., Sridhara, K. & Fuhrer, M. S. High mobility ambipolar MoS_2 field-effect transistors: Substrate and dielectric effects. *Appl. Phys. Lett.* **102**, 042104 (2013).

54 Nazir, G., Khan, M. F., Iermolenko, V. M. & Eom, J. Two-and four-probe field-effect and Hall mobilities in transition metal dichalcogenide field-effect transistors. *RSC Advances* **6**, 60787-60793 (2016).

55 Semenov, A. D., Gol'tsman, G. N. & Sobolewski, R. Hot-electron effect in superconductors and its applications for radiation sensors. *Superconductor Science and Technology* **15**, R1 (2002).

56 Shen, X., Wang, H. & Yu, T. How do the electron beam writing and metal deposition affect the properties of graphene during device fabrication? *Nanoscale* **5**, 3352-3358 (2013).

57 Bao, W. *et al.* Lithography-free fabrication of high quality substrate-supported and freestanding graphene devices. *Nano Res.* **3**, 98-102 (2010).

58 Kang, S., Movva, H. C. P., Sanne, A., Rai, A. & Banerjee, S. K. Influence of electron-beam lithography exposure current level on the transport characteristics of graphene field effect transistors. *J. Appl. Phys.* **119**, 124502 (2016).

59 Kumar, N., He, J., He, D., Wang, Y. & Zhao, H. Charge carrier dynamics in bulk MoS_2 crystal studied by transient absorption microscopy. *J. Appl. Phys.* **113**, 133702 (2013).

60 Wang, R. *et al.* Ultrafast and spatially resolved studies of charge carriers in atomically thin molybdenum disulfide. *Phys. Rev. B* **86**, 045406 (2012).

61 Buscema, M. *et al.* Large and tunable photothermoelectric effect in single-layer MoS2. *Nano Lett.* **13**, 358-363 (2013).

62 Bae, J. J. *et al.* Thickness-dependent in-plane thermal conductivity of suspended MoS_2 grown by chemical vapor deposition. *Nanoscale* **9**, 2541-2547 (2017).

63 Ding, Z., Jiang, J.-W., Pei, Q.-X. & Zhang, Y.-W. In-plane and cross-plane thermal conductivities of molybdenum disulfide. *Nanotechnol.* **26**, 065703 (2015).

64 Yan, R. *et al.* Thermal conductivity of monolayer molybdenum disulfide obtained from temperature-dependent Raman spectroscopy. *ACS nano* **8**, 986-993 (2014).

65 Sahoo, S., Gaur, A. P., Ahmadi, M., Guinel, M. J.-F. & Katiyar, R. S. Temperature-dependent Raman studies and thermal conductivity of few-layer MoS_2. *J. Phys. Chem. C* **117**, 9042-9047 (2013).

66 Lee, S.-M. & Cahill, D. G. Influence of interface thermal conductance on the apparent thermal conductivity of thin films. *Microscale Thermophys. Eng.* **1**, 47-52 (1997).

67 Zhu, J. *et al.* Ultrafast thermoreflectance techniques for measuring thermal conductivity and interface thermal conductance of thin films. *J. Appl. Phys.* **108**, 094315 (2010).

68 Yuan, P., Li, C., Xu, S., Liu, J. & Wang, X. Interfacial thermal conductance between few to tens of layered-MoS_2 and c-Si: Effect of MoS_2 thickness. *Acta Mater.* **122**, 152-165 (2017).

69 Wang, T. *et al.* Interfacial Thermal Conductance between Mechanically Exfoliated Black Phosphorus and SiOx: Effect of Thickness and Temperature. *Adv. Mater. Interfaces* **4**, 1700233 (2017).

70 Gu, X. & Yang, R. Phonon transport in single-layer transition metal dichalcogenides: A first-principles study. *Appl. Phys. Lett.* **105**, 131903 (2014).

71 Sreeprasad, T., Nguyen, P., Kim, N. & Berry, V. Controlled, defect-guided, metal-nanoparticle incorporation onto MoS_2 via chemical and microwave routes: electrical, thermal, and structural properties. *Nano Lett.* **13**, 4434-4441 (2013).

72 Liu, J., Choi, G.-M. & Cahill, D. G. Measurement of the anisotropic thermal conductivity of molybdenum disulfide by the time-resolved magneto-optic Kerr effect. *J. Appl. Phys.* **116**, 233107 (2014).

73 Aiyiti, A. *et al.* Thermal conductivity of suspended few-layer MoS_2. *Nanoscale* **10**, 2727-2734 (2018).

74 Jo, I., Pettes, M. T., Ou, E., Wu, W. & Shi, L. Basal-plane thermal conductivity of few-layer molybdenum disulfide. *Appl. Phys. Lett.* **104**, 201902 (2014).

75 Zhang, X. *et al.* Measurement of lateral and interfacial thermal conductivity of single- and bilayer MoS_2 and $MoSe_2$ using refined optothermal raman technique. *ACS Appl. Mater. Interfaces* **7**, 25923-25929 (2015).

76 Beechem, T., Yates, L. & Graham, S. Invited Review Article: Error and uncertainty in Raman thermal conductivity measurements. *Rev. Sci. Instrum.* **86**, 041101 (2015).

77 Yuan, P., Liu, J., Wang, R. & Wang, X. Hot Carrier Diffusion Coefficient of Sub-10 nm Virgin MoS_2: Uncovered by Non-contact Optical Probing. *Nanoscale* **9**, 6808-6820 (2017).

78 Wang, X. *Experimental Micro/nanoscale Thermal Transport*. (John Wiley & Sons, 2012).

79 Sadeghi, M. M., Pettes, M. T. & Shi, L. Thermal transport in graphene. *Solid State Commun.* **152**, 1321-1330 (2012).

80 Yu, D., Li, S., Qi, W. & Wang, M. Temperature-dependent Raman spectra and thermal conductivity of multi-walled MoS2 nanotubes. *Appl. Phys. Lett.* **111**, 123102 (2017).

81 Li, H., Wu, J., Yin, Z. & Zhang, H. Preparation and applications of mechanically exfoliated single-layer and multilayer MoS_2 and WSe_2 nanosheets. *Acc. Chem. Res.* **47**, 1067-1075 (2014).

82 Meitl, M. A. *et al.* Transfer printing by kinetic control of adhesion to an elastomeric stamp. *Nat. Mater.* **5**, 33-38 (2006).

83 Nemes-Incze, P., Osváth, Z., Kamarás, K. & Biró, L. Anomalies in thickness measurements of graphene and few layer graphite crystals by tapping mode atomic force microscopy. *Carbon* **46**, 1435-1442 (2008).

84 Perez, E. X. *Design, Fabrication and Characterization of Porous Silicon Multilayer Optical Devices* Doctoral thesis, Universitat Rovira i Virgili, (2007).

85 Zhang, H. *et al.* Measuring the Refractive Index of Highly Crystalline Monolayer MoS_2 with High Confidence. *Sci. Rep.* **5**, 8440 (2015).

86 Lee, C. *et al.* Anomalous lattice vibrations of single-and few-layer MoS_2. *ACS Nano* **4**, 2695-2700 (2010).

87 Su, L., Zhang, Y., Yu, Y. & Cao, L. Dependence of coupling of quasi 2-D MoS_2 with substrates on substrate types, probed by temperature dependent Raman scattering. *Nanoscale* **6**, 4920-4927 (2014).

88 Beechem, T., Graham, S., Kearney, S. P., Phinney, L. M. & Serrano, J. R. Invited Article: Simultaneous mapping of temperature and stress in microdevices using micro-Raman spectroscopy. *Rev. Sci. Instrum.* **78**, 061301 (2007).

89 Su, L., Zhang, Y., Yu, Y. & Cao, L. Dependence of coupling of quasi 2-D MoS 2 with substrates on substrate types, probed by temperature dependent Raman scattering. *Nanoscale* **6**, 4920-4927 (2014).

90 Wang, Y., Ni, Z., Shen, Z., Wang, H. & Wu, Y. Interference enhancement of Raman signal of graphene. *Appl. Phys. Lett.* **92**, 043121 (2008).

91 Yoon, D. *et al.* Interference effect on Raman spectrum of graphene on SiO_2/Si. *Phys. Rev. B* **80**, 125422 (2009).

92 Varshney, V. *et al.* MD simulations of molybdenum disulphide (MoS_2): Force-field parameterization and thermal transport behavior. *Computational Materials Science* **48**, 101-108 (2010).

93 Plimpton, S. Fast parallel algorithms for short-range molecular dynamics. *Journal of computational physics* **117**, 1-19 (1995).

94 Ong, Z.-Y. & Pop, E. Molecular dynamics simulation of thermal boundary conductance between carbon nanotubes and SiO_2. *Phys. Rev. B* **81**, 155408 (2010).

95 Xiao, J. *et al.* Alignment controlled growth of single-walled carbon nanotubes on quartz substrates. *Nano Lett.* **9**, 4311-4319 (2009).

96 Chang, S.-W., Nair, A. K. & Buehler, M. J. Geometry and temperature effects of the interfacial thermal conductance in copper–and nickel–graphene nanocomposites. *J. Phys.: Condens. Matter* **24**, 245301 (2012).

97 Rappé, A. K., Casewit, C. J., Colwell, K., Goddard Iii, W. & Skiff, W. UFF, a full periodic table force field for molecular mechanics and molecular dynamics simulations. *J. Am. Chem. Soc.* **114**, 10024-10035 (1992).

98 Liu, J., Xu, Z., Cheng, Z., Xu, S. & Wang, X. Thermal Conductivity of Ultrahigh Molecular Weight Polyethylene Crystal: Defect Effect Uncovered by 0 K Limit Phonon Diffusion. *ACS Appl. Mater. Interfaces* **7**, 27279-27288 (2015).

99 Shi, H. *et al.* Exciton dynamics in suspended monolayer and few-layer MoS_2 2D crystals. *ACS Nano* **7**, 1072-1080 (2013).

100 Nestoros, M., Forget, B. C., Christofides, C. & Seas, A. Photothermal reflection versus temperature: Quantitative analysis. *Phys. Rev. B* **51**, 14115 (1995).

101 Christofides, C., Othonos, A. & Loizidou, E. Influence of temperature and modulation frequency on the thermal activation coupling term in laser photothermal theory. *J. Appl. Phys.* **92**, 1280-1285 (2002).

102 Christofides, C. *et al.* Two-layer model for photomodulated thermoreflectance of semiconductor wafers. *J. Appl. Phys.* **80**, 1713-1725 (1996).

103 Fivaz, R. & Mooser, E. Mobility of charge carriers in semiconducting layer structures. *Phys. Rev.* **163**, 743 (1967).

104 Shur, M. S. *Handbook series on semiconductor parameters*. Vol. 1 (World Scientific, 1996).

105 Suh, J. *et al.* Doping against the native propensity of MoS_2: degenerate hole doping by cation substitution. *Nano Lett.* **14**, 6976-6982 (2014).

106 Linnros, J. Carrier lifetime measurements using free carrier absorption transients. I. Principle and injection dependence. *J. Appl. Phys.* **84**, 275-283 (1998).

107 Pérez, E. X. *Design, fabrication and characterization of porous silicon multilayer optical devices*. (Universitat Rovira i Virgili, 2008).

108 Lanzillo, N. A. *et al.* Temperature-dependent phonon shifts in monolayer MoS_2. *Appl. Phys. Lett.* **103**, 093102 (2013).

109 Neuberger, M. in *Handbook of Electronic Materials* 5-5 (Springer, 1971).

110 Wang, H., Zhang, C. & Rana, F. Ultrafast dynamics of defect-assisted electron–hole recombination in monolayer MoS_2. *Nano Lett.* **15**, 339-345 (2014).

111 Regner, K. T. *et al.* Broadband phonon mean free path contributions to thermal conductivity measured using frequency domain thermoreflectance. *Nat. Commun.* **4**, 1640 (2013).

112 Hu, Y., Zeng, L., Minnich, A. J., Dresselhaus, M. S. & Chen, G. Spectral mapping of thermal conductivity through nanoscale ballistic transport. *Nat. Nanotechnol.* **10**, 701-706 (2015).

113 Cai, Y., Lan, J., Zhang, G. & Zhang, Y.-W. Lattice vibrational modes and phonon thermal conductivity of monolayer MoS_2. *Phys. Rev. B* **89**, 035438 (2014).

114 Neamen, D. A. *Semiconductor physics and devices*. pp 154 (McGraw-Hill Higher Education, 2003).

115 Liu, L., Kumar, S. B., Ouyang, Y. & Guo, J. Performance limits of monolayer transition metal dichalcogenide transistors. *IEEE Trans. Electron Devices* **58**, 3042-3047 (2011).

116 Choi, W. *et al.* High detectivity multilayer MoS_2 phototransistors with spectral response from ultraviolet to infrared. *Adv. Mater.* **24**, 5832-5836 (2012).

117 Judek, J. *et al.* High accuracy determination of the thermal properties of supported 2D materials. *Sci. Rep.* **5**, 12422 (2015).

118 Ono, M., Ishihara, T. & Nishiyama, A. Influence of dielectric constant distribution in gate dielectrics on the degradation of electron mobility by remote Coulomb scattering in inversion layers. *IEEE Trans. Electron Devices* **51**, 736-740 (2004).

119 Yang, J. *et al.* in *2006 8th International Conference on Solid-State and Integrated Circuit Technology Proceedings.* 1315-1317 (IEEE).

120 Wang, L. *et al.* Slow cooling and efficient extraction of C-exciton hot carriers in MoS_2 monolayer. *Nat. Commun.* **8**, 13906 (2017).

121 Yu, Y. *et al.* Exciton-dominated dielectric function of atomically thin MoS_2 films. *Sci. Rep.* **5** (2015).

122 Lin, M.-W. *et al.* Thickness-dependent charge transport in few-layer MoS_2 field-effect transistors. *Nanotechnol.* **27**, 165203 (2016).

123 Li, S.-L. *et al.* Thickness scaling effect on interfacial barrier and electrical contact to two-dimensional MoS_2 layers. *ACS nano* **8**, 12836-12842 (2014).

124 Lembke, D., Allain, A. & Kis, A. Thickness-dependent mobility in two-dimensional MoS_2 transistors. *Nanoscale* **7**, 6255-6260 (2015).

125 Yang, R., Wang, Z. & Feng, P. X.-L. Electrical breakdown of multilayer MoS_2 field-effect transistors with thickness-dependent mobility. *Nanoscale* **6**, 12383-12390 (2014).

126 Zhou, K. G. *et al.* Size-Dependent Nonlinear Optical Properties of Atomically Thin Transition Metal Dichalcogenide Nanosheets. *Small* **11**, 694-701 (2015).

127 Wang, K. *et al.* Broadband ultrafast nonlinear absorption and nonlinear refraction of layered molybdenum dichalcogenide semiconductors. *Nanoscale* **6**, 10530-10535 (2014).

128 Keller, U. Recent developments in compact ultrafast lasers. *Nature* **424**, 831-838 (2003).

129 Kaasbjerg, K., Thygesen, K. S. & Jacobsen, K. W. Phonon-limited mobility in *n*-type single-layer MoS_2 from first principles. *Phys. Rev. B* **85**, 115317 (2012).

130 Liu, H. & Peide, D. Y. MoS_2 Dual-Gate MOSFET With Atomic-Layer-Deposited Al_2O_3 as Top-Gate Dielectric. *IEEE Electron Device Lett.* **33** (2012).

131 Fuhrer, M. S. & Hone, J. Measurement of mobility in dual-gated MoS_2 transistors. *Nat. Nanotechnol.* **8**, 146-147 (2013).

132 Li, S.-L. *et al.* Thickness-dependent interfacial coulomb scattering in atomically thin field-effect transistors. *Nano Lett.* **13**, 3546-3552 (2013).

133 Das, S., Chen, H.-Y., Penumatcha, A. V. & Appenzeller, J. High performance multilayer MoS_2 transistors with scandium contacts. *Nano Lett.* **13**, 100-105 (2012).

134 Bernardi, M., Palummo, M. & Grossman, J. C. Extraordinary sunlight absorption and one nanometer thick photovoltaics using two-dimensional monolayer materials. *Nano Lett.* **13**, 3664-3670 (2013).

135 El-Mahalawy, S. & Evans, B. The thermal expansion of 2H-MoS_2, 2H-$MoSe_2$ and 2H-WSe_2 between 20 and 800° C. *J. Appl. Crystallogr.* **9**, 403-406 (1976).

136 Gan, C. K. & Liu, Y. Y. F. Direct calculation of the linear thermal expansion coefficients of MoS_2 via symmetry-preserving deformations. *Phys. Rev. B* **94**, 134303 (2016).

137 Touloukian, Y. S., Powell, R., Ho, C. & Nicolaou, M. Thermophysical Properties of Matter-The TPRC Data Series. Volume 10. Thermal Diffusivity. (DTIC Document, 1974).

138 Lin, J.-Y. *et al.* in *Imaging Methods for Novel Materials and Challenging Applications, Volume 3* 353-358 (Springer, 2013).

139 Trott, G. R. & Shorey, A. in *Microsystems, Packaging, Assembly and Circuits Technology Conference (IMPACT), 2011 6th International.* 359-362 (IEEE).

140 Sarma, K. *et al.* in *Proc. of SPIE Vol.* 181.

141 McAlpine, M. C. *et al.* High-performance nanowire electronics and photonics on glass and plastic substrates. *Nano Lett.* **3**, 1531-1535 (2003).

142 Pu, J. *et al.* Highly flexible MoS_2 thin-film transistors with ion gel dielectrics. *Nano Lett.* **12**, 4013-4017 (2012).

143 Yoon, J. *et al.* Highly flexible and transparent multilayer MoS_2 transistors with graphene electrodes. *Small* **9**, 3295-3300 (2013).

144 Lee, G.-H. *et al.* Flexible and transparent MoS_2 field-effect transistors on hexagonal boron nitride-graphene heterostructures. *ACS Nano* **7**, 7931-7936 (2013).

145 Yuan, P., Wang, R., Tan, H., Wang, T. & Wang, X. Energy Transport State Resolved Raman for Probing Interface Energy Transport and Hot Carrier Diffusion in Few-Layered MoS_2. *ACS Photonics* **4**, 3115-3129 (2017).

146 Lui, C. H., Liu, L., Mak, K. F., Flynn, G. W. & Heinz, T. F. Ultraflat graphene. *Nature* **462**, 339-341 (2009).

147 Quereda, J., Castellanos-Gomez, A., Agraït, N. & Rubio-Bollinger, G. Single-layer MoS_2 roughness and sliding friction quenching by interaction with atomically flat substrates. *Appl. Phys. Lett.* **105**, 053111 (2014).

148 Tang, X., Xu, S. & Wang, X. Corrugated epitaxial graphene/SiC interfaces: photon excitation and probing. *Nanoscale* **6**, 8822-8830 (2014).

149 Schmidt, A. J., Chen, X. & Chen, G. Pulse accumulation, radial heat conduction, and anisotropic thermal conductivity in pump-probe transient thermoreflectance. *Rev. Sci. Instrum.* **79**, 114902 (2008).

150 Rubio-Bollinger, G. *et al.* Enhanced visibility of MoS_2, $MoSe_2$, WSe_2 and black-phosphorus: making optical identification of 2D semiconductors easier. *Electronics* **4**, 847-856 (2015).

151 Wang, R. *et al.* Asymmetry of Raman scattering by structure variation in space. *Opt. Express* **25**, 18378-18392 (2017).

152 Wang, H. *et al.* in *Electron Devices Meeting (IEDM), 2012 IEEE International.* 4.6. 1-4.6. 4 (IEEE).

153 Santos, E. J. & Kaxiras, E. Electrically driven tuning of the dielectric constant in MoS2 layers. *ACS Nano* **7**, 10741-10746 (2013).

154 Sui, Y. & Appenzeller, J. Screening and interlayer coupling in multilayer graphene field-effect transistors. *Nano Lett.* **9**, 2973-2977 (2009).

155 Chen, J.-H., Cullen, W., Jang, C., Fuhrer, M. & Williams, E. Defect scattering in graphene. *Phys. Rev. Lett.* **102**, 236805 (2009).

156 Fridleifsson, I. B. Geothermal energy for the benefit of the people. *Renewable Sustainable Energy Rev.* **5**, 299-312 (2001).

157 Tongay, S. *et al.* Defects activated photoluminescence in two-dimensional semiconductors: interplay between bound, charged, and free excitons. *Sci. Rep.* **3**, 2657 (2013).

158 Qiu, H. *et al.* Hopping transport through defect-induced localized states in molybdenum disulfide. *Nat. Commun.* **4**, 2642 (2013).

159 Venezuela, P., Lazzeri, M. & Mauri, F. Theory of double-resonant Raman spectra in graphene: Intensity and line shape of defect-induced and two-phonon bands. *Phys. Rev. B* **84**, 035433 (2011).

160 Xu, H., Xie, L., Zhang, H. & Zhang, J. Effect of graphene Fermi level on the Raman scattering intensity of molecules on graphene. *ACS Nano* **5**, 5338-5344 (2011).

161 Pettes, M. T., Maassen, J., Jo, I., Lundstrom, M. S. & Shi, L. Effects of surface band bending and scattering on thermoelectric transport in suspended bismuth telluride nanoplates. *Nano Lett.* **13**, 5316-5322 (2013).

162 Gu, X., Li, B. & Yang, R. Layer thickness-dependent phonon properties and thermal conductivity of MoS_2. *J. Appl. Phys.* **119**, 085106 (2016).

163 Lindsay, L., Broido, D. & Mingo, N. Flexural phonons and thermal transport in graphene. *Phys. Rev. B* **82**, 115427 (2010).

164 Xin-Ran, W., Yi, S. & Rong, Z. Field-effect transistors based on two-dimensional materials for logic applications. *Chinese Physics B* **22**, 098505 (2013).

165 Cheng, R. *et al.* Few-layer molybdenum disulfide transistors and circuits for high-speed flexible electronics. *Nat. Commun.* **5** (2014).

166 Akinwande, D., Petrone, N. & Hone, J. Two-dimensional flexible nanoelectronics. *Nat. Commun.* **5**, 5678 (2014).